ՀՀ ԳԱԱ Վ. ՀԱՄԲԱՐՁՈՒՄՅԱՆԻ անվ. ԲՅՈՒՐԱԿԱՆԻ ԱՍՏՂԱԴԻՏԱՐԱՆ

Նաիրա Մուշեղի Ազատյան

«Երիտասարդ ենթակարմիր աստղակույտերի որոնում և ուսումնասիրություն»

Ատենախոսություն

Ա.03.02 – «Աստղաֆիզիկա, ռադիոաստղագիտություն» մասնագիտությամբ
ֆիզիկամաթեմատիկական գիտությունների թեկնածուի գիտական աստիճանի համար

Գիտական ղեկավար՝
ֆ.մ.գ.թ. Ելենա Համլետի Նիկողոսյան

Բյուրական-2022

NAS RA BYURAKAN ASTROPHYSICAL OBSERVATORY after V.A. AMBARTSUMIAN

Naira M. Azatyan

“Search and study of young infrared stellar clusters”

DOCTORAL THESIS

For the degree of Doctor of philosophy in

the specialization 01.03.02 – Astrophysics and Radioastronomy

Supervisor:

Dr. Elena H. Nikoghosyan

Byurakan-2022

CONTENT

CHAPTER 1

1. INTRODUCTION

The star formation process continues at all stages of the evolution of our and other galaxies, including the present one [7], and is one of the most important processes which provides the visible output of the galaxies. The evolutionary process of stars enriches the surrounding environment by heavy elements through a continuous manner via powerful stellar winds and an instantaneous manner via supernova explosions accompanied by a strong release of energy, which, in addition to generating turbulent motions in the surrounding gas-dust matter, contributes to maintaining its highly heterogeneous structure and may, under certain circumstances, give birth to new molecular regions prone to star formation. Therefore, stellar clusters are recognized as important laboratories for astrophysical research. Most stars (70-90%) appear to form in clusters (e.g., [7]; [112]; [81]) and most of these clusters dissolve on timescales of 10s of Myrs [77] to form the field star population. The majority of the clusters are unbound immediately upon formation by the expulsion of gas (e.g., [108]; [67]; [109]), while those that survive this initial phase are often disrupted over the next few hundred Myr by processes such as dynamical interactions with other molecular clouds or Galactic tidal fields (e.g. [8]; [112]; [105]; [53]). Therefore, the young stellar clusters (not older, than ~$3x10^6$ years) have provided an important tracer of recent star formation in galaxies and of spiral structure in galactic disks with a wide range of stellar mass (from O high-mass stellar objects to brown dwarfs) within relativity small volume of space. Since stars in such groups share the common heritage of being formed more or less simultaneously from the same progenitor molecular cloud, observations of a cluster can be used to provide classical tests of stellar evolution theory. Presently, it is generally recognized that the stellar content of our Galaxy forms in clusters located within cold (T~10-30 K) and dense ($n > 10^3$ cm^{-3}) giant molecular clouds of the Galactic disk (e.g. [28]; [112]). Therefore, the main properties of the stellar population in the young clusters, such as the density distribution, the age and age spread, the star formation efficiency (SFE), and the shape of the initial mass function (IMF) might be very well closely related to the physical properties and mass distribution of the progenitor structures in the parental cloud (e.g. [135]). There is a large number of observation data, which witness that the star formation process has consecutive nature [185]. Therefore, the spatial distribution of young stellar objects (YSOs) in clusters and the quantitative ratio between YSOs with different masses and ages are essential for understanding the evolutionary history of a cluster itself. However, such studies have been seriously hampered by the fact that galactic clusters form in giant molecular clouds and during their formation and earliest stages of evolution are completely embedded in molecular gas and dust, and thus obscured from view. Given the constraints imposed by traditional techniques of optical astronomy, direct observation and study of young embedded clusters had been extremely difficult, if not impossible. However, during the last two decades, the development of infrared (IR) astronomy has dramatically improved this situation providing astronomers the ability to survey and systematically study embedded clusters within molecular clouds.

Embedded stellar clusters, which are still surrounded by molecular clouds are of particular interest to understand which properties of stellar clusters are related to their origins and which are derived from subsequent evolution [65]; [112]. For example, mass segregation, the concentration of higher mass stars in the centers of clusters, which is observed in many optically visible open clusters is also seen in some of the embedded clusters. Because the embedded clusters are too young to have undergone significant dynamical evolution, the mass segregation must be a property of the process of star formation in the natal molecular clouds. In recent years, significant progress has been made in solving problems related to the theory of star formation. For example, many investigations show, that the special distribution of stellar population in the young clusters is not uniform. Observations of young clusters usually indicate that the most massive stars (high and intermediate-mass) are as a rule located near the center of the cluster [193]; [110]; [68]. This is true for both poor [93], [194] and extended rich [205] clusters. The location of the high-mass stars near the center of the cluster could be an indication of where they formed. Individual stars accrete at highly different rates, dependent on their position in the cluster potential. Stars that spend more time near the center of the cluster accrete more than those that are in the outer regions. This happens as the gas falls preferentially into the deepest part of the potential, to be accreted by whichever star is nearest [31]. In the example of several clusters, a certain relationship was revealed between the stellar density of the cluster and the average mass of its members. Low-mass stars form in loose groups of a few objects per cubic parsec [76], while high-mass stars are usually found to form in dense clusters with densities up to 10^4 objects per cubic parsec in the case of the Trapezium cluster (see e.g. [134]; [96]). There is also a certain relationship between the properties of the stellar population of young clusters and the process of their formation. If the star-formation in clusters is triggered, the age spread of stars in the cluster should be small, while in self-initiated protocluster condensations, the individual clumps should have a larger age spread [205].

Despite all efforts, however, today there are much more questions in the theory of star formation than answers to them. Some of the relatively clarified questions include the mechanism of low-mass star formation. The formation of low-mass TTau stars is composed of different stages [123]; [119]; [182]; [189]. In the first stage, when there are no pressure gradients in the molecular cloud, the whole cloud begins to collapse in free fall forming prestellar fragmentations in many gravitationally bound cores in a molecular cloud. Prestellar fragmentations start to become opaque with a protostellar object in the center as its central density reaches about 10^{-13}g cm^{-3} [123]; [32]. At some point, a given condensation becomes gravitationally unstable and quickly collapses to form star/stars [123]; [9]. The high angular momentum core material forms an infalling envelope of gas and dust which begins to provide additional material for the central object through its built accretion disk which surrounds the central object [182]. Initially, the mass of the central protostar is very small than the mass of the surrounding envelope. The formation of the star is finished when the infall/accretion phase is terminated. In the final stage, the surrounding envelope and circumstellar disk material will be either fully accreted (or dispersal) and/or the disk material turns into a planetary system [189]. Observations have shown that the star formation process is accompanied by bipolar outflows (e.g. [19]). These outflows are believed to carry away the excess angular momentum of the infalling matter [111]. These theoretical phases have been confirmed by observations of stellar objects at different evolutionary stages: from molecular protostellar clouds to low-mass main-sequence stars [113]; [12]. Several studies show that most intermediate-mass Herbig Ae/Be stars share a number of characteristics of low-mass stars [95]. However, extending this theory to high-mass stars is not trivial. One of the many reasons is that high dust extinction makes it difficult to observe high-mass stars during critical early formation phases. They evolve quickly and important evolutionary phases are short-lived. As a result, high-mass stars reach the zero-age main sequence (ZAMS) while still accreting (e.g. [102]; [204]; [68]; etc.).

Significant amounts of interstellar gas and dust in the envelopes and disks surrounding the YSOs can absorb the energy emitted by the central star and reproduce it at longer wavelengths. Since the surrounding gas and dust in the envelope and disk disappear during the time, the IR colors and spectral energy distributions (SEDs) of the YSOs provide the most robust method for the identification of their evolutionary stage [95]; [140]; [137]; [4]. Therefore, IR observations are an essential and powerful tool for investigating young stars with all masses and evolutionary stages [122]. Figure 1 shows the empirical evolutionary sequence for the formation of a single star from a prestellar cloud core to a Class III YSO which is taken from [9]. In near-(NIR) and mid-(MIR) IR wavelengths, three classes of low-mass YSOs can be distinguished based on the slope of their SEDs [119]; [113]. Class III ("Weak" T Tauri stars) and Class II ("Classical" T Tauri stars) sources correspond to pre-main-sequence (PMS) stars surrounded by a circumstellar disk (optically thin and optically thick at <10 μm wavelengths, respectively), but lacking a dense circumstellar envelope [10]. The younger Class I objects detected at 2 μm are surrounded by both a disk and a low-mass (often only residual) circumstellar envelope [10]; [130]; [192]. Besides these evolutionary phases of YSOs, (sub)millimeter dust continuum mapping of molecular cloud cores with large ground-based radio telescopes has revealed even younger, compact protostellar condensations designated as Class 0 which remains invisible at ≤25 μm [12]. The youngest, i.e. the prestellar stage of star formation has been detected by (sub)millimeter line and continuum observations. At this phase, a gravitationally bound core has formed in a molecular cloud and the central hydrostatic protostellar object does not exist yet within the core (i.e., $M_{star} = 0$). Therefore, the search and classification of YSOs are based on the existence of their main properties, namely, the existence of circumstellar envelope and disk which causes one of the main observational properties of YSOs – IR excess.

Investigations have shown that more than one mechanism may be at work forming clusters in the natal molecular cloud and all embedded clusters are associated with IRAS sources [161]. The obtained data only strengthened the confidence that stars are born in deeply embedded regions, which contain a significant amount of intimately mixed relatively cold gas and dust [167. This component of the star formation regions is called the interstellar medium (ISM). The matter in ISM, which exists in the form of gas (atoms, molecules, ions, and electrons) and dust (tiny solid particles), manifests itself primarily through obscuration, reddening, and polarization of starlight, through the formation of absorption lines in stellar spectra, and through various emission mechanisms (both over a continuum and at specific wavelengths). This material accounts for ~10–15% of the total mass of the Galactic disk. It tends to concentrate near the Galactic plane and along the spiral arms while being very inhomogeneously distributed at small scales. It displays dramatic density and temperature contrasts, such that only the densest, coldest molecular regions can offer an environment favorable to star formation [70].

Consequently, the study of ISM in conjunction with the study of embedded in them YSOs is very important for understanding the process of formation and evolution of the stellar population.

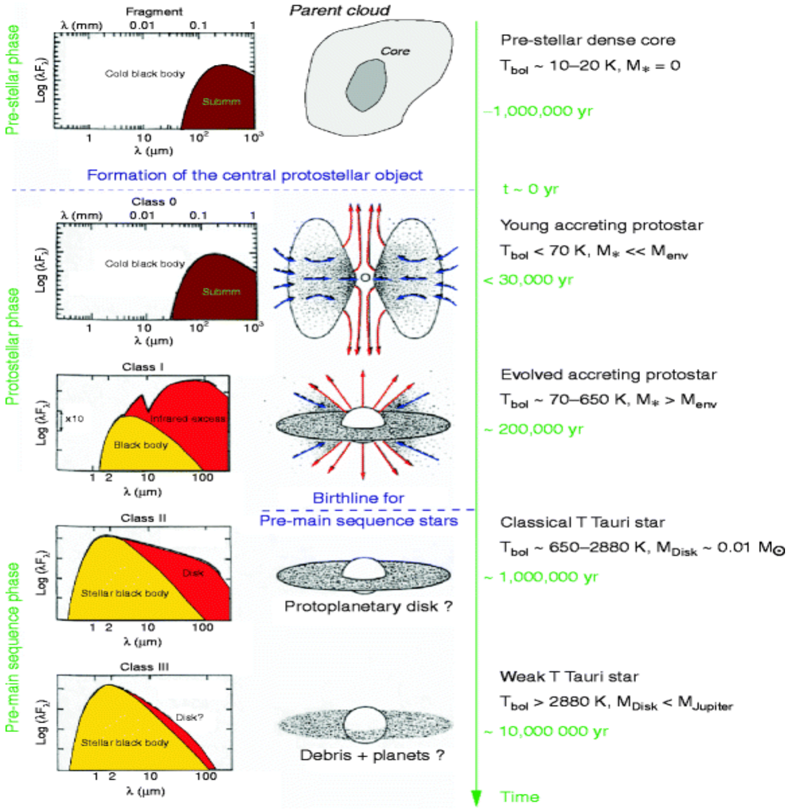

Figure 1. Empirical evolutionary sequence for the formation of a single star from a prestellar cloud core to a Class III YSO, based on the shape of the SED (left), the bolometric temperature, and the mass of circumstellar material indicated on the right [12].

As was already mentioned, the most fundamental properties of molecular clouds are temperature, density, and mass, which, apparently, heavily influence the process of star formation. At the typical low temperatures and high densities of these dusty star-forming systems, the primary constituent, hydrogen, cannot be directly observed, and the conditions in them are therefore measured through alternative tracers. Studies show that, commonly, the low temperature of molecular clouds (e.g. 10 K) is resulting in the far-IR (FIR) and submillimetre (submm) emission which is dominated by dust grains, mostly composed of silicates and oxides [56]; [114]; [50]. Therefore, dust grains play an important role in the astrophysics of the ISM. Interstellar dust determines what galaxies look like, how the ISM in a galaxy behaves. The most obvious effect of dust grains is that they cause the extinction of starlight. It is estimated that 30% or more of the energy emitted as starlight in the Universe is reradiated by dust in the IR [24]. The line-of-sight dust column density may be determined by fitting a modified black-body model to the SED of the thermal dust emission [92]. This technique, however, requires knowledge of the dust properties and changing physical conditions, including the temperature in the molecular clouds (e.g., [88], [60]; [181]; [51].

To better understand the process of star formation as a whole, it is necessary to study the nature of star formation regions in the Galaxy and the properties of subsystems in these regions. Many papers have been published on searches for and studies of new stellar clusters embedded in star-forming regions ([27]; [110]; [68]; [147], etc.). It should be noted, however, that searches for stellar clusters in the vicinity of YSOs with assumed high masses are not always successful. For example, [110] discovered only 57 clusters in the neighborhoods of 217 YSOs associated with IRAS sources; this represents only 26%. Thus, the question arises of why clusters were not observed in the other 74% and whether this was caused by a lack of observational data. It appears that the central regions of compact groups of YSOs (with diameters of 1pc and ages of 1 Myr), embedded in a dense gas-dust matter, generally include a YSO or a pair of stars with high and intermediate masses [65]; [112]; [107]. Studies of the star-forming regions may be relevant to an entire range of questions related to the evolutionary theory of individual stellar objects of different masses, as well as of clusters as a whole, in a couple of the ISM. For our research, we have chosen relatively poorly-studied regions that are located at a significant distance. The aims of this thesis are:

- The search for young stellar clusters in the vicinity of IRAS objects, which appear to be associated with high-mass YSOs;
- Identification of the clusters' members using their IR properties;
- Investigation of structural properties of young stellar clusters;
- Determination of age and age spread of clusters' members;
- Construction of the Luminocity Functions (LFs) and Mass Functions (MFs) for clusters;
- Determination of ISM parameters, namely the distribution of hydrogen column density ($N(H_2)$) and dust temperature (T_d);

- Determination of SFE and star formation rate (SFR)

This thesis is based on the papers [151], [16], [15], [156], [155], [18], [153] and [17]. The thesis is structured as follows: Chapter 2 introduces the methods based on which we searched for star-forming regions and investigate them. In Chapter 3, the results of the search of compact stellar clusters in the sample of star-forming regions, as well as the determination of their sizes and the special distribution of the stellar content in them are presented. Chapter 4 contains a detailed study of three star-forming regions which include the behavior of ISM in them and the identification of the young stellar population with their properties. The results of our investigation are concluded in Chapter 5.

CHAPTER 2

2. METHODS

2.1. Observational data

In our study, we used data covering a wide range of NIR to FIR wavelengths. The first dataset comprises archival NIR photometric data and images in the J, H, and K bands of the Galactic Plane Survey DR6 (UKIDSS GPS, [129]) with a resolution of 0.1″/px, which is one of the five surveys of the *UKIRT* Infrared Deep Sky Survey (UKIDSS). This survey is complete to approximately 18 mag in the K band and provides a percentage probability of an individual object being a star, galaxy, or noise. In the absence of UKIDSS GPS data, we used the data of the Two Micron Sky Survey (2MASS, [52]).

The MIR wavelengths are ideal for studying circumstellar disks because these wavelengths are well removed from the peak of the underlying stellar energy distribution, resulting in much greater excesses over the underlying stellar photosphere. Archival MIR observations were obtained from the *Spitzer* Space Telescope under the Galactic Legacy Infrared Midplane Survey Extraordinaire (GLIMPSE) and GLIMPSE 360 programs [47]. GLIMPSE observations were taken using the InfraRed Array Camera (IRAC; [69]) centred at 3.6, 4.5, 5.8, and 8 μm with a resolution of 0.6"/px. GLIMPSE360 is a *Spitzer* “Warm Mission” program. After the cryogen depletion in May 2009, the observatory is operating only at 3.6 and 4.5 μm channels of IRAC with a resolution of 0.6"/px. GLIMPSE and GLIMPSE360 data products are very similar. There are two types of source lists: a high-reliability point source Catalog and a more complete point source Archive. At longer wavelengths, we used data from a survey of the inner Galactic plane using the Multiband Infrared Photometer for *Spitzer* (MIPSGAL). The survey field was imaged in 24 and 70 μm passbands with resolutions of 6"/px and 18"/px, respectively [38]; however, only 24 μm data were available for the studied star-forming regions. The point source photometric data were downloaded from the NASA/IPAC Infrared Science Archive.

We also used All-sky Wide-field Infrared Survey Explorer (AllWISE, [52]) program MIR data which extends the work of the successful Wide-field Infrared Survey Explorer mission (WISE, [201]) in the 3.4, 4.6, 12, and 22 μm bandpasses. AllWISE combined data from the cryogenic and post-cryogenic survey phases to form the most comprehensive view of the MIR sky currently available. Also, we used the

Midcourse Space Experiment (MSX, [165]) full plane survey data in the 8.28, 12.13, 14.65, and 21.3 μm bands, which are accessible through VizieR.

To study gas and dust, as well as deeply embedded point sources, we used FIR observations in the 70–500 μm range, obtained with the Photodetector Array Camera and Spectrometer (PACS, [163]) and the Spectral and Photometric Imaging Receiver (SPIRE, [79]) on board the 3.5 m *Herschel* Space Observatory [162]. For our analyses, we used photometric data and images of *Herschel* PACS 70, 160 μm and SPIRE 250, 350, and 500 μm catalogs, and the *Herschel* infrared Galactic Plane Survey (Hi-GAL, [144]) at 70, 160, 250, 350, and 500 μm wavebands. The corresponding *Herschel* half-power beamwidth (HPBW) values are 5.0" at 70 μm, 11.4" at 160 μm, 17.8" at 250 μm, 25.0" at 350 μm, and 35.7" at 500 μm. The point and extended source photometry were downloaded from the NASA/IPAC Infrared Science Archive. There are objects which have measured fluxes in both *Herschel* PACS and Hi-GAL catalogs. We used Hi-GAL photometric data for those cases.

The Infrared Astronomical Satellite (IRAS, [150]) Point Source Catalog v2.1 (PSC) data was used. The IRAS mission performed an unbiased, sensitive all-sky survey at 12, 25, 60, and 100 μm. *Herschel* PACS and Hi-GAL data have better resolution than the IRAS PSC data. Therefore, we used the data from the Hi-GAL 70, 160 μm, or *Herschel* PACS 70, 160 μm catalogs instead of IRAS 60 and 100 μm data. We also used the SCUBA Legacy Catalogues [57] obtained with the Submillimetre Common User Bolometer Array (SCUBA) operating at 850 and 450 μm bandpasses accessible in VizieR service.

2.2. Dust emission

The Hi-GAL observations provide a complete and unbiased view of continuum emission in the Galactic plane in 70, 160, 250, 350, and 500 μm bands. This wavelength range covers the peak of the spectral energy distribution of cold dust emission, constraining important ISM parameters such as the hydrogen column density ($N(H_2)$) and the dust temperature (T_d).

To obtain the $N(H_2)$ and T_d, the thermal emission from cold dust lying in the *Herschel* FIR optically thin bands (160–500 μm) can be used [92], [22]. Following the discussion in the previous studies (e.g. [22]) this wavelength range is well applicable for those cases where the dust temperature is in the range of 5-50 K, while there are no clear restrictions for the column density. We excluded the 70 μm band emission, which would have a significant contribution from the warm dust component, and, therefore, modeling with a single-temperature blackbody would over-estimate the derived temperatures. Besides, in this range, the optically thin assumption would not hold.

For our task, the processed *Herschel* images were downloaded through the *Herschel* Interactive Processing Environment (HIPE, [158]). To eliminate the effect of bad pixels on the final result, we gave them the median value of eight immediate-neighbor pixels. For the estimation of N(H_2) and T_d, we used the following order of steps. First of all, the surface brightness unit for all images was converted to $\mathrm{Jy/px}$. Since the PACS image is already in $\mathrm{Jy/px}$, this step was only required for the SPIRE images (whose units are in $\mathrm{MJy/sr}$). Next, the 160–350 μm images were convolved to the resolution of the 500 μm image (lowest among all images), using the convolution kernels of [13], and regridded to a pixel scale of 14 arcsec (same as 500 μm image). These steps are carried out using the plug-in "*Photometric Convolution*" and task "*Convert Image Unit*" available in the HIPE software.

Modified single-temperature blackbody fitting was subsequently carried out on a pixel-by-pixel basis using the following formula:

$$S_\nu = B_\nu(\nu,\ T_d)\,\Omega\,(1 - e^{-\tau(\nu)}) \tag{1}$$

with

$$\tau(\nu) = \mu_{H_2}\, m_H\, k_\nu\, N(H_2) \tag{2}$$

where ν is frequency, $S_\nu(\nu)$ is observed flux density, $B_\nu(\nu,\ T_d)$ is Planck function, T_d is dust temperature, Ω is the solid angle in steradians from where the flux is obtained (in this case for all bands the solid angle subtended by a 14 arcsec×14 arcsec pixel), $\tau(\nu)$ is optical depth, μ_{H_2} is the mean molecular weight (adopted as 2.8 here), m_H is the hydrogen mass, k_ν is dust opacity, and $N(H_2)$ is hydrogen column density. For opacity, we adopt a functional form of $k_\nu = 0.1(\nu/1000\ GHz)^\beta\ cm^2 g^{-1}$, with β=2 (see [92], [11]). For each pixel, equation (1) was fitted using the four data points (160, 250, 350, and 500 μm) keeping T_d and N(H_2) as free parameters. [124] used a conservative 15% uncertainty in the flux densities of the *Herschel* bands. We adopt the same value for all bands. The uncertainties of the parameters were derived using Pearson's χ^2 statistics:

$$\chi^2 = \sum_{i=1}^{N} \frac{(D_i - F_i)^2}{F_i} \tag{3}$$

where D_i is observed flux and F_i is flux predicted by the model, N is the number of bands. Notably, the parameters obtained with the modified blackbody model do not deviate from certain errors, which are related to a number of factors, including the quality of the images used and the uncertainty of calibration of *Herschel* images. Besides, the errors are a strong function of the parameters' values. According to the previous studies, the mentioned above values of k_ν and β provide the good result for environment with T_d in the range from 5 to 60 K. To a large extent, the final result is also affected by the fact that star-forming regions show the structure of many scales, and so fitting a single column density and temperature to any point does not adequately represent the whole region [22]. In our cases, the increase of χ^2 is most likely explained by the quality of the images. Figure 2 shows an example of the *Herschel* image of Level 2.5, where there are many bad pixels. Moreover, a whole strip of bad pixels passes through the bright condensation, which whatever filtering cannot completely remove. This is most likely the reason for the increase in the χ^2 value in the regions.

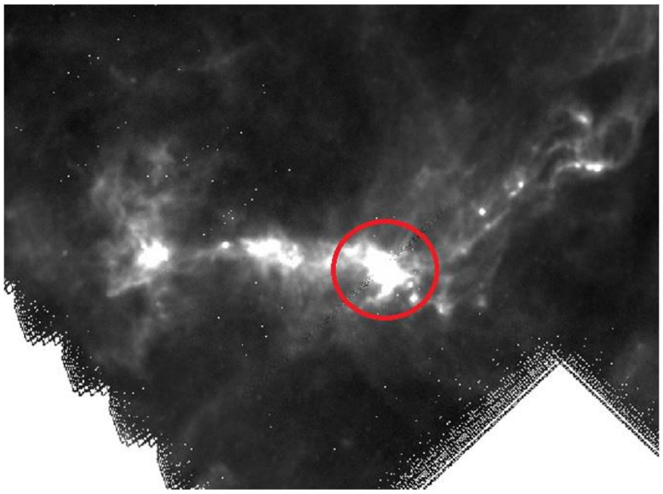

Figure 2. *Herschel* image at 250 μm (2.5 Level). The red circle marks the location of bad pixels in the vicinity of IRAS05168+3634 source.

From the derived $N(H_2)$ values, we estimate the mass of the dusty clumps using the following expression:

$$M_{clump} = \mu_{H_2} \, m_H \, Area_{pix} \sum N(H_2), \tag{4}$$

where $Area_{pix}$ is the area of a pixel in cm^2.

2.3. Selection of stellar objects

To select and study the potential stellar members of the star-forming regions, we used NIR, MIR, and FIR data (see Section 2.1). The identification of YSOs was performed with GPS UKIDSS-DR6 as the main catalogue, and then other MIR and FIR catalogues were cross-matched with it. As was mentioned in Section 2.1, the GPS UKIDSS-DR6 catalogue provides the probability of an object being a star, galaxy, or noise based on its image profile. The UKIDSS team recommends that sources classified as noise should be excluded from studies since most of them are not real sources [129]. However, "galaxies" and "probable galaxies" should be included in the full search, since many of them are unresolved pairs of stars or nebulous stars and could be potential members of the star-forming region. Therefore, we selected objects with a <30 % probability of being noise and a magnitude of $K < 18.02$ mag, taking into account the K band limit of the UKIDSS survey. In addition, we removed objects with zero errors of measured magnitudes in the J, H, and K bands. The MIR and FIR photometric catalogues were cross-matched with the GPS UKIDSS-DR6 catalogue within 3σ of combined error-matching radius (Col. 3 in Table 1). Matching radii were evaluated considering the positional accuracy of each catalogue (Col. 2 in Table 1). Sometimes, the matching radii were quite large, especially for the FIR catalogues. Additionally, multiple NIR objects can be identified by only one FIR object; in such cases, priority was given to the object with significantly higher brightness in the NIR/MIR range. If necessary, we selected the closest one by coordinates. When it was not possible to identify a single object, we did not use those FIR data to avoid possible errors. The set of steps that we used to identify the YSOs in the combined photometric catalogue is presented in the following sub-sections.

2.3.1. Colour-colour diagrams

When selecting potential members of a cluster from stars located in the direction of the molecular cloud, we assumed that most of the members of the considered active star-forming region are YSOs. One of the main observational characteristics of YSOs is an IR excess due to the presence of circumstellar discs and envelopes [112]; [86]; furthermore, the measure of the IR excess in the NIR and/or MIR ranges can be used to characterise the evolutionary stage of a YSO (Class I and Class II). Therefore, YSO candidates can be identified based on their position in colour–colour (c-c) diagrams. The choice of colours depends on the available data. Objects with IR excess were first identified using the (J–H) versus (H–K) c–c NIR diagram.

Table 1. Properties of catalogs cross-matched with the GPS UKIDSS-DR6

Catalog name	Positional accuracy (arcsec)	3σ of combined error (arcsec)	Reference
(1)	(2)	(3)	(4)
GPS UKIDSS-DR6	0.3	-	[129]
GLIMPSE	0.3	1.2	[47]
AllWISE	1	3	[201]
MIPSGAL	1	3	[38]
MSX	3.3	10	[62]
IRAS	16	48	[150]
PACS: Extended source	2.4	7.2	[131]
PACS: 70 μm	1.5	5	[163]
PACS: 160 μm	1.7	5.2	[163]
SPIRE:250,350,500 μm	1.7	5.2	[79]
Hi-GAL: 70, 160, 250, 350, 500 μm	2	6.1	[176]

Notes. (1) Name of used catalog, (2) Positional accuracy of each catalog, (3) 3σ of combined error of cross-matched catalogs, (4) Source of used data.

Figure 3 **a)** shows the (J-H) versus (H-K) c-c diagram, where the solid curves represent the loci of the intrinsic colours of dwarf and giant stars [25] converted to the CIT system [39]; the parallel solid lines drawn from the base and the tip of these loci are the interstellar reddening vectors [168]. The locus of unreddened classical T Tauri stars (CTTSs) is taken from [140]. The region where the intermediate-mass PMS stars, i.e. Herbig Ae/Be stars, are usually found is bounded by dashed lines [89]. Objects with different evolutionary stages occupy specific areas in this diagram [122]: (i) Classical Be stars, (ii) objects located to the left, and (iii) objects located to the right of reddening vectors. Classical Be stars have J-K<0.6 and H-K<0.3 colour indices, which we removed from the final list.

The deviation of YSOs from the main sequence (MS) on this diagram can have two causes: the presence of IR excess and interstellar absorption, which also leads to objects reddening. In the latter case, deviation from MS will be directed along the reddening vectors. The IR excess of objects located to the right of reddening vectors (iii) cannot be caused solely by interstellar absorption and, at least partially, their IR excess is caused by the existence of a circumstellar disc and an envelope. Therefore, objects located to the right of reddening vectors can be considered YSO candidates. Among the selected YSOs and objects located in the reddening band of MS and giants (ii), we classified those that have (J-K)>3 mag colour index as Class I evolutionary stage YSOs [122]. These are located in the upper right corner of the diagram.

Other objects in the reddening band are generally considered to be either field stars or Class III objects with small NIR excess. The latter objects can be potential members of the star-forming region, however, differentiating between field stars and Class III objects is very difficult. Thus, we added to the final list those objects from this sample that were classified as Class I and Class II evolutionary stage YSOs in at least two c–c diagrams.

Not all objects in the main sample were detected in the J, H, and K bands simultaneously. Accordingly, we used data from the GLIMPSE and GLIMPSE360 catalogues to combine NIR and MIR photometry to identify sources with IR excesses and compile a more complete excess/disc census for the regions. Since the 4.5 μm band is the most sensitive of the four IRAC bands to YSOs [83], we used K-[3.6] versus [3.6]-[4.5] and (J-K) versus [3.6]-[4.5] c-c diagrams. The [3.6]-[4.5] colour is dominated by accretion rate, with higher accretion rate sources appearing redder [4].

Figure 3 **b)** shows the K-[3.6] versus [3.6]-[4.5] c-c diagram, with diagonal lines outlining the YSO location region and a dashed line separating the Class I and II object domains. The arrow shows the extinction vector [72]. All the lines in the K-[3.6] versus [3.6]-[4.5] diagram are taken from [6]. Figure 3 **c)** shows the (J-K) versus [3.6]-[4.5] c-c diagram where the solid curves represent the loci of the intrinsic colours of dwarf and giant stars [74] converted to the CIT system [39]; the parallel solid lines drawn from the base and the tip of these loci are the interstellar reddening vectors. The equations from [37] were used to construct the reddening vectors. These c-c diagrams are widely used for the YSO separations with different evolutionary classes [140]; [83]; [6].

The MIR SEDs of Class I and Class II objects are dominated by emission from dusty circumstellar material, allowing them to be readily distinguished from pure photospheric sources such as unrelated field stars and indistinguishable diskless members. *Spitzer* is advantageous for studying such regions since its imaging instruments (IRAC at 3.6-8 μm and MIPS at 24-160 μm) are targeted to the MIR wavelengths, which are less affected by extinction from dust in comparison to NIR [82]. Since the IRAC 8 μm band overlaps with silicate features, reddened photospheres would appear increasingly blue in [5.8]-[8.0] colour [137]. Figure 3 **d)** and **e)** show c-c diagrams with different combinations of *Spitzer* wavelengths distinguishing YSOs from both Class I and Class II evolutionary stages. In the **d)** panel of Figure 3, we used *Spitzer* IRAC wavelengths. Objects located around the ([3.6]-[4.5]; [5.8]-[8.0])=(0;0) region are stars with the colours of the stellar photosphere and disk-less PMS (i.e. Class III) objects. Class II objects fall within the 0<[3.6]-[4.5]<0.8 and 0.4<[5.8]-[8.0]<1.1 range. Objects with [3.6]-[4.5]>0.8 and [5.8]-[8.0]>1.1 range likely correspond to a Class I evolutionary stage [4]; [137]; [166].

The 24 μm channel is the primary means of identifying optically thin dust discs. Since photospheric colours should be close to zero for all spectral types, the [8.0]–[24] colour is particularly sensitive to excess [149]. In the **e)** panel of Figure 3, we used *Spitzer* IRAC and MIPS wavelengths to plot a [3.6]–[5.8] versus [8.0]–[24] c-c diagram. Sources clustered around [3.6]–[5.8]~0; 0≤[8]–[24]≤1 probably represent a mixture of pure photospheres and perhaps some modest 24 μm excess. Therefore objects with [3.6]-[5.8]>1.5 and [8.0]-[24]>2.4 colours are likely to be Class I sources with envelopes. Class II objects with optically thick discs exhibit [3.6]-[5.8]>0.3 and [8.0]-[24]>2 colours values [149]; [43].

Additionally, we constructed two other MIR c-c diagrams using the list of objects with good WISE detections, i.e., those possessing photometric uncertainty <0.2 mag in WISE bands. **f)** panel of Figure 3 shows the [3.4]-[4.6] versus [4.6]-[12] c-c diagram. Similar to the previous cases, objects with different evolutionary stages fall within certain areas of this diagram [104]. Class I YSOs are the reddest objects, with [3.4]-[4.6]>1.0 and [4.6]-[12]>2.0. Class II YSOs are slightly less red objects and have [3.4]-[4.6]-σ([3.4]-[4.6])>0.25 and [4.6]-[12]-σ([4.6]-[12])>1.0, where σ(...) indicates the combined photometric error, added in quadrature. The accuracy of the previous classification of stars with photometric errors <0.2 mag can be verified using WISE band 4. **g)** panel of Figure 3 shows the [3.4]-[4.6] versus [4.6]-[22] c-c diagram. Previously classified Class I sources were re-classified as Class II if [4.6]-[22]<4.0, and the Class II stars were returned to the unclassified pool if [3.4]-[12]<-1.7×([12]-[22])+4.3 [104].

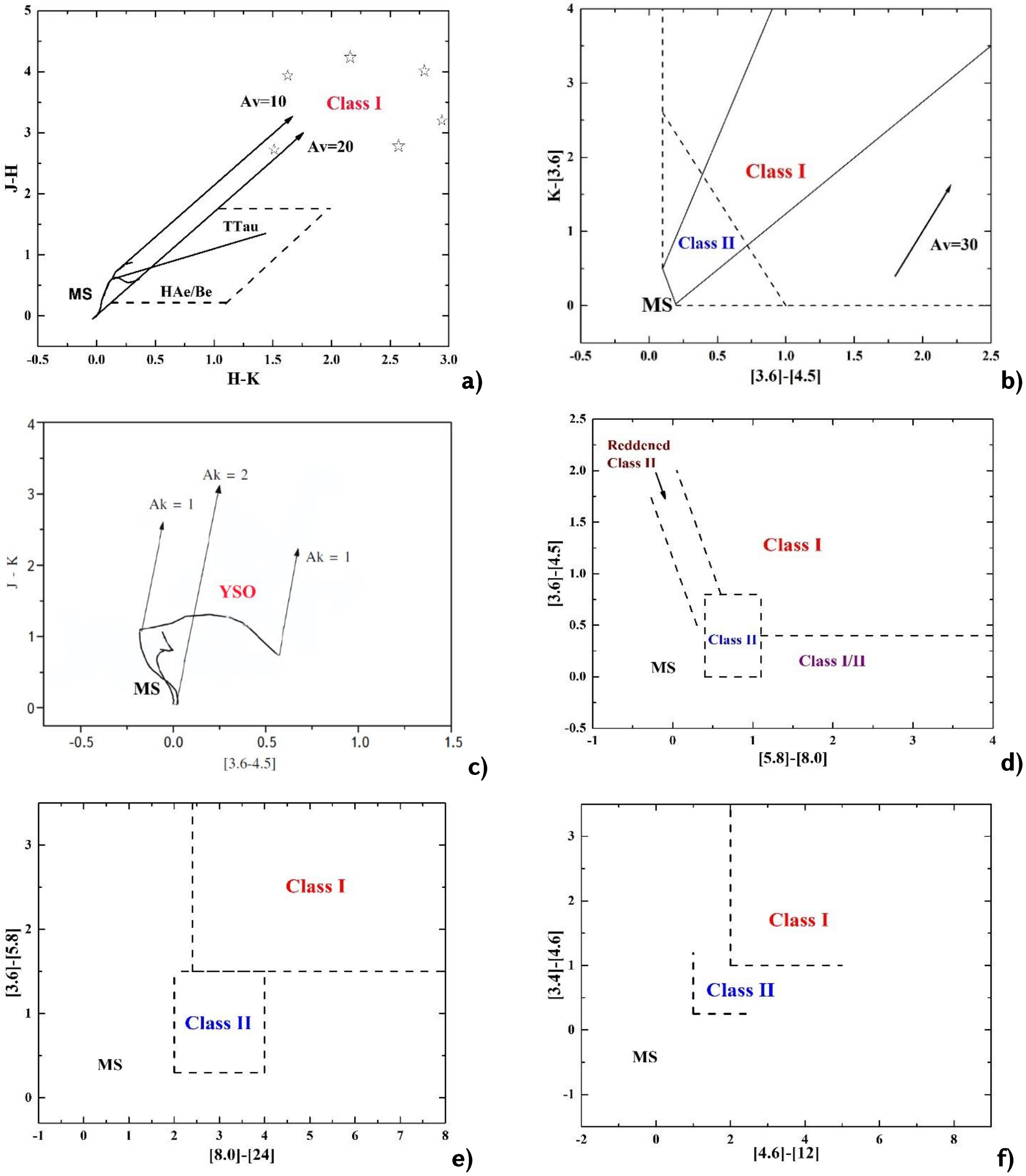
a)
J-H
H-K
Av=10
Av=20
Class I
TTau
MS
HAe/Be
b)
K-[3.6]
[3.6]-[4.5]
Class I
Class II
Av=30
MS
c)
J - K
[3.6-4.5]
Ak = 1
Ak = 2
Ak = 1
YSO
MS
d)
[3.6]-[4.5]
[5.8]-[8.0]
Reddened
Class II
Class I
Class II
MS
Class I/II
e)
[3.6]-[5.8]
[8.0]-[24]
Class I
Class II
MS
f)
[3.4]-[4.6]
[4.6]-[12]
Class I
Class II
MS

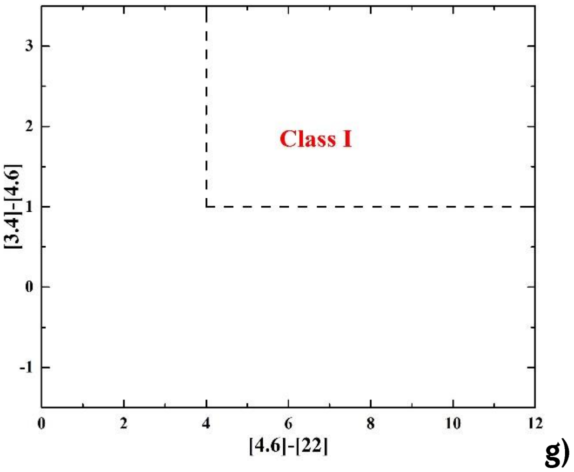

Figure 3. Colour-colour diagrams. ***a)*** (J-H) vs. (H-K) diagram. The dwarf and giant loci (solid and dashed curves, respectively) are from [25] and were converted to the CIT system [39]. The parallel lines represent the interstellar reddening vectors [168]. The locus of unreddened classical T Tauri stars is from [140], and the region bounded by dashed lines is the Herbig Ae/Be stars location [89]. ***b)*** K-[3.6] vs. [3.6]-[4.5] diagram. In this diagram Class I and II domains are separated by the dashed line. The arrow shows the extinction vector [72]. All the lines in the K-[3.6] vs. [3.6]-[4.5] diagram are from [6]. ***c)*** (J-K) vs. [3.6]-[4.5] diagram. The position of the MS and giant branch are taken from [74]. The equations from [37] were used to construct the reddening vectors. The relationships from [39] have been used to tie the various photometric systems to one another. ***d)*** [3.6]-[4.5] vs. [5.8]-[8.0] diagram. The two parallel dashed lines border the positions of reddened Class II objects. The horizontal dashed line shows the adopted division between Class I and Class I/II sources. The dashed rectangle shows the position of Class II sources. All the lines in the [3.6]-[4.5] vs. [5.8]-[8.0] diagram are from [137]. ***e)*** [3.6]-[5.8] vs. [8.0]-[24] diagram. The horizontal and vertical dashed lines separate Class I sources in this region. The dashed rectangle shows the position of Class II sources. All the lines in the [3.6]-[5.8] vs. [8.0]-[24] diagram are from [149]. ***f)*** and ***g)*** are [3.4]-[4.6] vs. [4.6]-[12] and [3.4]-[4.6] vs. [4.6]-[22] diagrams, respectively.

2.3.2. α_{IRAC} slope

Examining the IR SEDs of YSOs is one of the most robust methods for identifying the presence of a circumstellar disc. The shape of the SED can distinguish a disc origin for the observed IR excesses from other possible causes. A particularly useful measure of the shape of a SED is its slope, which is defined as $\lambda F_\lambda \propto \lambda^{\alpha_{IRAC}}$ [113]. We measured the α_{IRAC} slope values for each of the sources detected in all four IRAC bands (3-8μm). Diskless stars (i.e. stellar photospheres) are characterised by α_{IRAC}<-2.56 (Class

III), while evolved discs fall within the -2.56<α_{IRAC}<-1.8 range (Class II/III). Class II evolutionary stage objects have values in the -1.8<α_{IRAC}<0 range, while Class I evolutionary stage objects are characterized by α_{IRAC}>0 [87]; [117]. The selection of YSOs by α_{IRAC} slope is based on the same fluxes as used in the [3.6]-[4.5] versus [5.8]-[8.0] c-c diagram.

2.3.3. Extraction of field contamination

While IR excess is a powerful membership diagnostic tool for young and embedded sources, many potential contaminants exhibit IR excess. There are mainly two classes of extragalactic contaminants that can be misidentified as YSOs [188]. One is star-forming galaxies and narrow-line active galactic nuclei (AGNs), which have growing excesses at 5.8 and 8.0 μm due to hydrocarbon emission. The other is broad-line AGNs, which have IRAC colours very similar to those of YSOs. [82] developed a method based on the Bootes Shallow Survey data to substantially mitigate these contaminants. In this method, hydrocarbon emission sources, including galaxies and narrow-line AGNs, can be eliminated based on their positions in the [3.6]-[5.8] versus [4.5]-[8.0] diagram. The broad-line AGNs, which are typically fainter than YSOs in the *Spitzer* bands, are identified by their positions in the [4.5] versus [4.5]-[8.0] colour–magnitude diagram.

We firstly checked our list of YSOs according to the conclusions of [188], i.e. galaxies dominated by polycyclic aromatic hydrocarbon (PAH) emission should have MIR colours that occupy a relatively unique area of most IRAC c-c diagrams: [3.6]-[5.8]<1.5×([4.5]-[8.0]-1)/2, [3.6]-[5.8]<1.5, and [4.5]-[8.0]>1. By initially filtering out the PAH sources, we can construct a filter that more closely traces the broad-line AGN distribution and then use the [4.5] versus [4.5]-[8.0] colour-magnitude diagram to flag likely broad-line AGNs according to conditions of [82] and [166]: [4.5]-[8.0]>0.5, [4.5]>13.5+([4.5]-[8.0]-2.3)/0.4, and [4.5]>13.5. Among our selected YSOs, we also applied a condition (i.e. [4.5]>7.8 and [8.0]-[24.0]<2.5) to identify possible asymptotic giant branch (AGB) contaminants [170]. We removed from the final list all objects satisfying the above-mentioned conditions.

2.4. Determination of the YSOs parameters based on spectral energy distribution

To confirm the selected YSOs and to determine their parameters, we constructed their SEDs and fitted them with the radiative transfer models of [171]. These models assume an accretion scenario in the star formation process, where a central star is surrounded by an accretion disc, an infalling flattened envelope, and the presence of bipolar cavities. We used the command-line version of the SED fitting tool where numerous precomputed models are available. This procedure was performed using wavelengths ranging from 1.1 to 500 μm, in particular, J, H, and K (2MASS); J, H, and K (UKIDSS); 3.6, 4.5, 5.8, and 8.0 μm (*Spitzer* IRAC); 24 μm (*Spitzer* MIPS); 3.4, 4.6, 12, and 22 μm (WISE); 8.28, 12.13, 14.65, and 21.3 μm (MSX); 12 and 25 μm (IRAS); 70 and 160 μm (*Herschel* PACS), 70, 160, 250, 350, and 500 μm (Hi-GAL). We took the apparent magnitudes of those surveys where the object was detected as a point source. We considered as an upper limit the FIR fluxes that were identified as closest by coordinates to the NIR object to avoid possible errors (see Section 2.3). For the interstellar extinction, we chose an interval taking into account the results obtained by COBE/DIRBE and IRAS/ISSA maps. The distance interval corresponds to the estimations made in the previous studies. To identify the representative values of different physical parameters, the tool retrieved the best-fit model and all models that exhibited differences between χ^2 values and the best χ^2 smaller than 3N, where N is the number of the data points used [171]. This approach was chosen because the sampling of the model grid is too sparse to effectively determine the minima of the χ^2 surface and consequently obtain the confidence intervals.

CHAPTER 3

3. SELECTION OF THE REGIONS

3.1. Objects

For our search for compact clusters, we chose IRAS sources from the list of [196] which are associated with YSOs, presumably with high-masses ($M > 8\ M_\odot$). Different manifestations of activity were observed in all regions: H_2 and CO outflows, emissions in NH_3, H_2O, and CH_3OH lines, compact HII regions, etc. Overall, 20 regions from [196] list were detected in GPS UKIDSS.

In order to detect clusters in considered 20 regions, we constructed surface stellar density distribution maps around each IRAS source within a 4'x4' region using photometric data of the GPS UKIDSS-DR6 and GLIMPSE. The density was determined simply by dividing the number of stellar sources in a “b”x”b” box with a step size of “a”. Three sets of “b” and “a” values were used: 40" and 20"; 30" and 15"; and 20" and 10". In order to maximize the ability to detect a cluster, the dimensions of box and step were determined empirically for each cluster; this will increase the statistical significance of the local peaks in stellar density. A large-sized box may “smear” out the local density peaks against the common background. On the other hand, if the box is too small then the overall picture is affected by errors since the number of sources in each box is comparable to random fluctuations in the background stellar density. Ultimately, the sizes of the box and step were chosen by taking into account the size of the group itself. A cluster was considered to really exist if the surface stellar density in the vicinity of the IRAS source exceeded the average background by more than 2σ. Isodenses of the found clusters are shown in Figure 4.

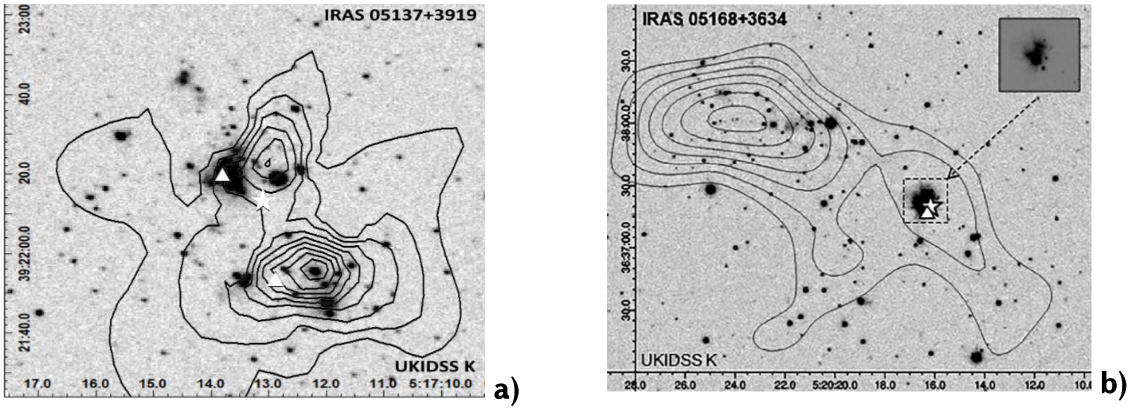

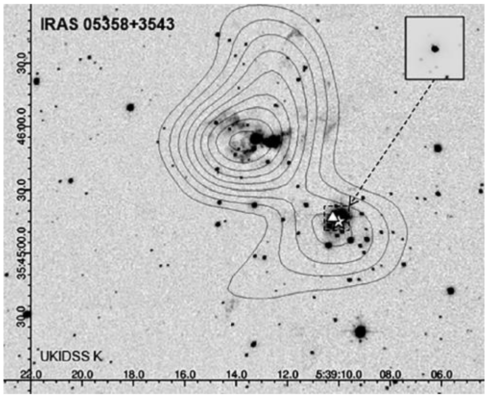
IRAS 05358+3543
UKIDSS K
22.0
20.0
18.0
16.0
14.0
12.0
5:39:10.0
08.0
06.0
30.0
46:00.0
30.0
35:45:00.0
30.0

c)

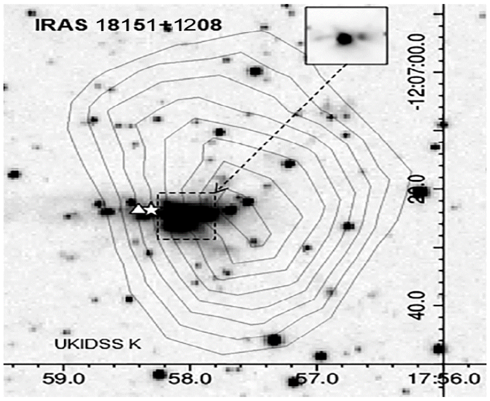
IRAS 18151-1208
UKIDSS K
59.0
58.0
57.0
17:56.0
-12:07:00.0
20.0
40.0

c)

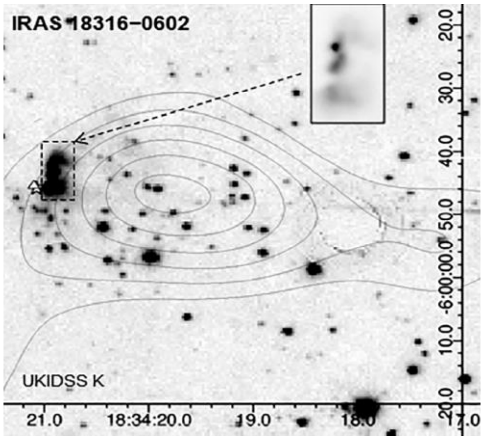
IRAS 18316−0602
UKIDSS K
21.0
18:34:20.0
19.0
18.0
17.0
20.0
30.0
40.0
50.0
-6:00:00.0
10.0
20.0

d)

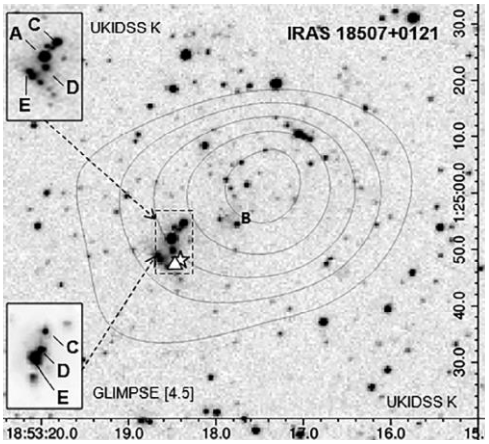
IRAS 18507+0121
UKIDSS K
A
C
D
E
B
GLIMPSE [4.5]
C
D
E
UKIDSS K
18:53:20.0
19.0
18.0
17.0
16.0
30.0
20.0
10.0
1:25:00.0
50.0
40.0
30.0

e)

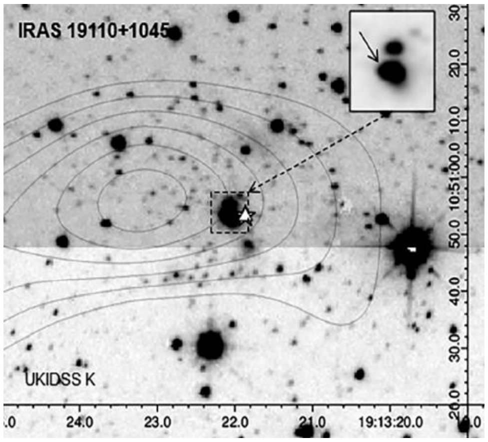
IRAS 19110+1045
UKIDSS K
24.0
23.0
22.0
21.0
19:13:20.0
30.0
20.0
10.0
10:51:00.0
50.0
40.0
30.0
20.0

f)

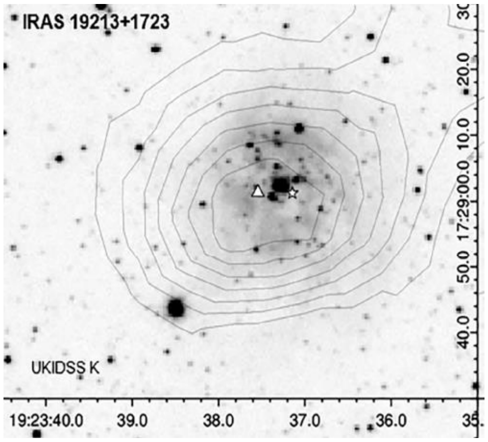
IRAS 19213+1723
UKIDSS K
19:23:40.0
39.0
38.0
37.0
36.0
20.0
10.0
17:29:00.0
50.0
40.0

g)

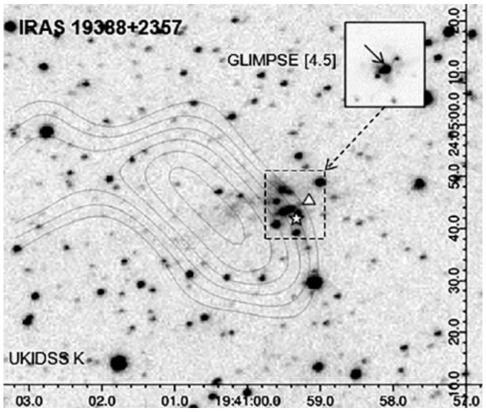
IRAS 19388+2357
GLIMPSE [4.5]
UKIDSS K
03.0
02.0
01.0
19:41:00.0
59.0
58.0
57.0
20.0
10.0
24:05:00.0
50.0
40.0
30.0
20.0
10.0

h)

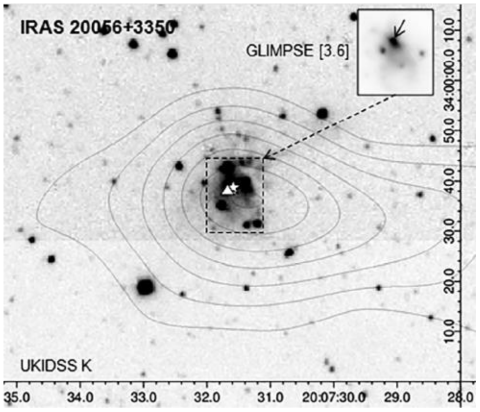
IRAS 20056+3350
GLIMPSE [3.6]
UKIDSS K
35.0
34.0
33.0
32.0
31.0
20:07:30.0
29.0
28.0
10.0
34:00:00.0
50.0
40.0
30.0
20.0
10.0

k)

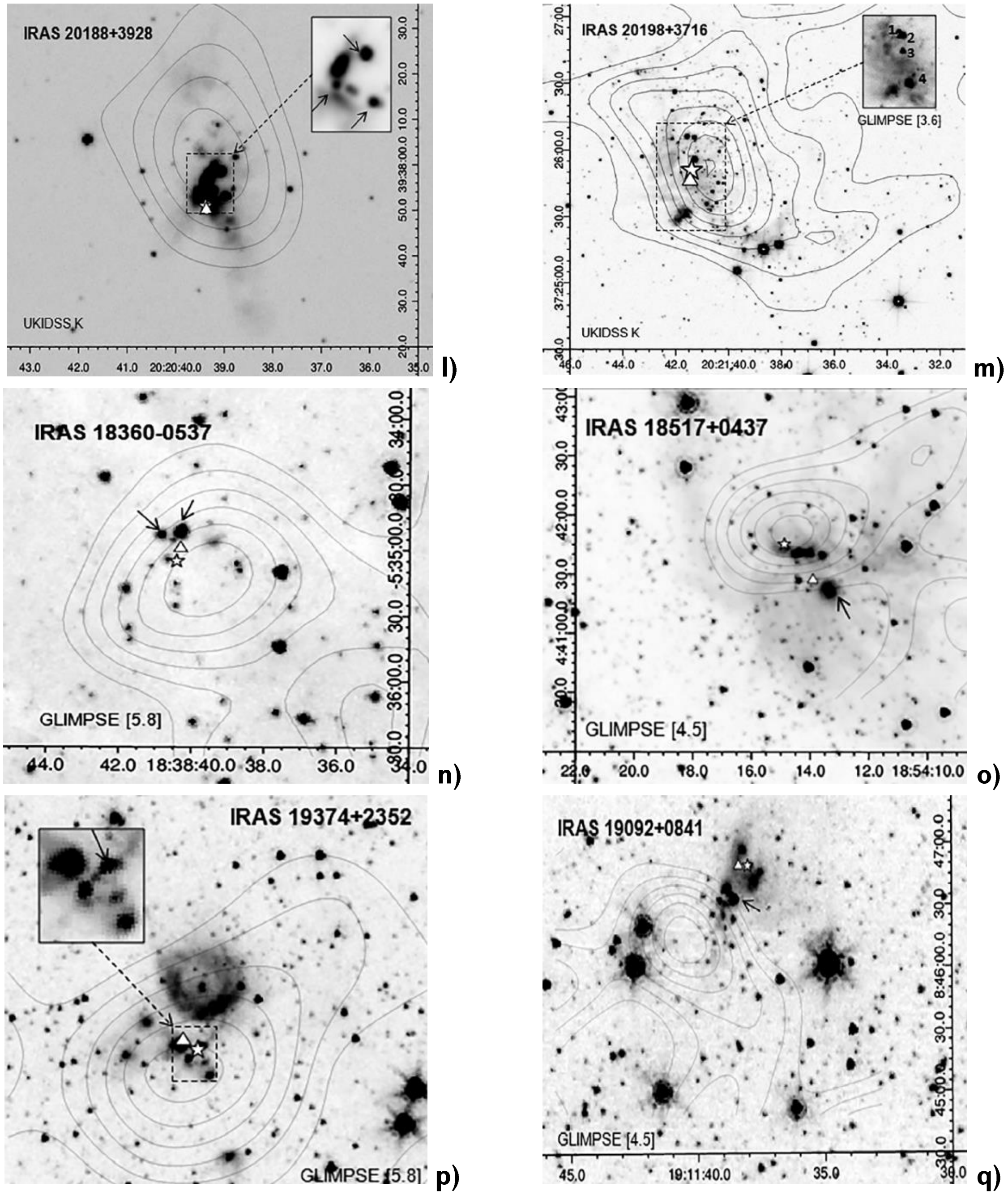

Figure 4. NIR and MIR images and isodenses of the considered regions [16]. IRAS and MSX sources are indicated by stars and triangles, respectively.

In order to confirm the existence of clusters in the vicinity of the IRAS sources, and to refine their sizes, we also constructed the radial density distribution of stars with respect to the geometric center of the group. The stellar density was determined in rings of width 0.1′ by dividing the number of stars by the surface area. The standard error for the number of stars in each ring is used as a measure of uncertainty. The radius of the clusters was considered the value from which according to Poisson statistics the fluctuations of the stellar density in the rings become random. Figure 5 is an example of the radial density distribution of stars relative to the IRAS05168+3634 source and it shows that starting from 1.5′ radius, the density of the cluster does not exceed the average density of the field. In addition, Figure 4 **a)** shows nonuniform distribution of objects within the cluster and they form subgroups corresponding to the shape of the isodense. Table 2 lists main parameters of the discovered clusters.

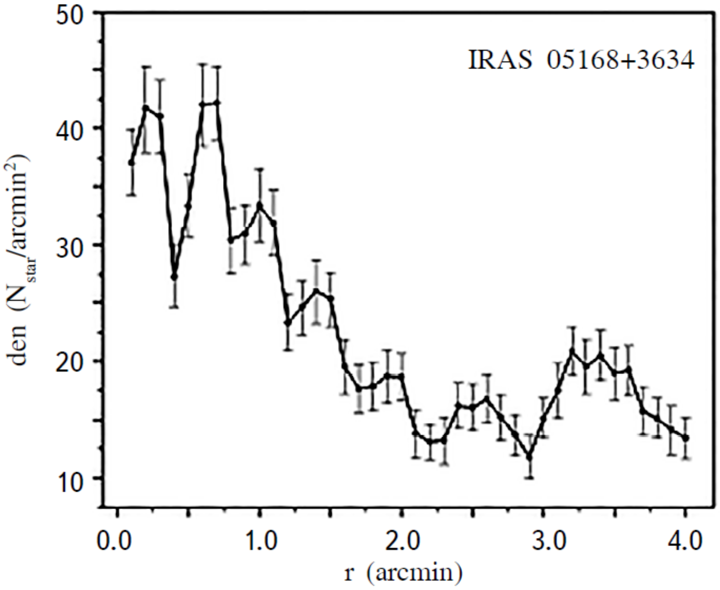

Figure 5. Radial distribution of the stellar density relative to IRAS05168+3634 source [16]. Vertical lines are standard errors.

The number of probable YSO candidates for all regions (N_{YSO}, see Table 2) has been estimated by their position on (J-H) vs (H-K) c-c diagram. In some cases, it exceeds the excess number (N_{obj}) of stars relative to the average stellar density of the field. For those regions where clusters of YSOs were identified in the MIR, we used colour indices from [4] and [81].

We have also compared the LF of stellar objects in the clusters and their fields. For this purpose, we have compiled two samples for each region: (1) objects in the cluster and (2) objects within the ring of 3R and 6R radii. The number of stars in the second sample was reduced to the surface of the cluster. The measure of consistency between the LFs for these two samples (P_{KS}, Table 2) was determined using the Kolmogorov-Smirnov test.

Table 2. Main parameters of the compact clusters

N	IRAS	D (kpc)	A_v	R′ (pc)	N_{obj}	N_{YSO}	d (stars/pc^2)	P_{KS}
(1)	(2)	(3)	(4)	(5)	(6)	(7)	(8)	(9)
UKIDSS GPS								
1	05137+3919	4.5, 11	1.7	1.5 (2.0, 4.8)	239	84	6.6, 1.2	0.001
2	05168+3634	6.1	3.6	1.5 (2.7)	93	80	4.1	0.003
3	05358+3543	1.8	5.4	1.2 (0.6)	154	73	136	0.007
4	18151-1208	3	2.8	0.3 (0.3)	20	14	71	0.027
5	18316-0602	3.2	3.9	0.5 (0.4)	53	38	68	0.001
6	18507+0121	3.9	5.3	0.4 (0.5)	45	13	57	0.010
7	19110+1045	6, 8.3	2.9	0.3 (0.5, 0.7)	52	53	66, 34	0.469
8	19213+1723	4.3	0.5	0.3 (0.4)	19	30	38	0.000
9	19388+2357	4.3	3.0	0.3 (0.4)	7	24	14	0.019
10	20056+3350	1.7	0.3	0.6 (0.3)	93	53	329	0.041
11	20188+3928	3.9	5.1	0.5 (0.6)	13	-	12	0.031
12	20198+3716	0.9, 5.5	2.6	1.3 (0.3, 2.0)	385	298	1362, 28	0.001
GLIMPSE								
13	18360-0537	6.3	2.8	0.4 (0.7)	13	12	8.4	0.039
14	18517+0437	2.9	5.6	0.3 (0.3)	4	5	14	0.022
15	19092+0841	4.5	2.6	0.4 (0.5)	7	5	8.9	0.136
16	19374+2352	4.3	2.6	0.8 (1.0)	25	8	8.0	0.039
No cluster found								
17	18174-1612	2.1	7.3	-	-	-	-	-
18	18385-0512	2.1	2.2	-	-	-	-	-
19	19410+2336	2.1, 6.4	4.4	-	-	-	-	-
20	20126+4104	1.7	4.9	-	-	-	-	-

Notes. (1) the sequence number, (2) IRAS source, (3) distance (when distance to the source has different estimates, we provided both values), (4) interstellar extinction [58]; [59]; [179], (5) radii of the clusters, (6) the

---

excess number of objects, (7) the number of probable YSOs, (8) surface density defined relative to the excess number of objects, (9) measure of consistency between the luminosity functions in the cluster and field.

3.2. Results of the search for compact clusters

We were able to detect compact clusters in 12 and 4 regions based on NIR and MIR data, respectively. Totally, this represents 80% of the considered regions. In IRAS20188+3928 region, we were not able to detect stars with distinct IR excess. It should be noted, however, undoubtedly a certain number of YSOs fall between the reddening vectors (Figure 3 **a)**), and our N_{YSO} value is only a lower limit of the total number of YSOs in this region. In IRAS19110+1045 and IRAS19092+0841 regions, the coincidence between the LFs of the clusters and field is greater than 10%. Nevertheless, other criteria, i.e. high surface stellar density and essential number of objects with a distinct IR excess confirm that the detected stellar clusters are real formations in these regions. Figure 4 **a)**, **b)** and **c)** show that the two identified clusters (IRAS05168+3634 and IRAS05358+3543) have a bimodal structure. The sub-groups located directly in vicinities of the IRAS sources have radii of 0.5 and 0.2 pc and surface densities of 10 and 199 stars/pc^2, respectively, which exceeds the density in the cluster as a whole. We were not able to detect clusters in four regions.

Table 2 shows there are no particular differences in the distances or interstellar extinction for the regions where a cluster was detected with NIR (1-12 rows) and MIR (13-16 rows) data or where we were not able to detect any group (17-20 rows). Table 3 shows parameters of the YSOs associated with IRAS sources and they are the central objects in the detected compact clusters.

IRAS 05137+3919. It is a bimodal star-forming region; one of the sub-groups concentrated in the vicinity of the IRAS source. The IRAS source with high probability is associated with close pair of YSOs and one of them is the objects at very early Class I evolutionary stage. Our preliminary study already revealed significantly more PMS objects than was obtained in the previous studies [110], [68], as well as more complicated structure of the region.

IRAS 05168+3634. This is a bimodal cluster; one of the sub-groups is concentrated around the IRAS source. The IRAS source is associated with a YSO in Class I evolutionary stage. Our results somewhat differ from similar earlier works. The cluster in this region has already been identified in 2MASS image [110]. The isodense is similar to ours but the number of possible members of the cluster is considerably smaller, most likely because of the difference in the photometric limit of the data. [68] examined the region within ~20" radius immediately surrounding the IRAS source.

IRAS 05358+3543. This is the already known binary cluster named Sh 2-2332RNE and Sh 2-2331RSW. Within our defined 1.1' radius, which corresponds to the size of the cluster, the SFE exceeds 20% (**Yan et al. 2010**). After 1.1' radius SFE≈5%, which is lower than the minimum SFE for star-forming regions [112]. In the (J-H) vs. (H-K) c-c diagram, the central object is located in the region of Herbig Ae/Be stars.

IRAS 18151-1208. This previously unknown compact group of YSOs is associated with GSH 018+02+27 HI cloud [63]. The central object has an essential IR excess and appears to be in Class I evolutionary stage. In previous papers, the ZAMS spectral type of this object was estimated to be B0.

IRAS 18316-0602. This previously unknown compact group of YSOs is located in the RAFGL 7009S HII region. As in the previous case, the central object has a very essential IR excess and can be classified as Class I evolutionary stage object. In previous papers, the ZAMS spectral type of this object was also estimated to be B0-B1.

IRAS 18507+0121. Previously, there were discovered IR stellar objects in this region with ages younger than $3x10^6$ yr [180]. They have also been identified in the MIR (G3CC 61, [147]). [196] proposed two stars: “A” and “B” (see Figure 4 **e)**), as YSO candidates associated with the IRAS. According to the 2MASS data, only “B” object has an IR excess, which can be assumed to be a Herbig Ae/Be star. In addition, according to data from the GLIMPSE survey, this region contains at least three more YSOs (“C”, “D”, “E”) which could be classified as Class I evolutionary stage objects. “E” object is a binary. It is possible that IRAS and MSX sources refer to “D” and “E” objects, respectively, as they are located very close to them. “C” object was of special interest. It is not detected in the 2MASS images and K image in [196] but has substantial brightness in the GPS UKIDSS and GLIMPSE images. This object is an already known eruptive variable [154].

IRAS 19110+1045. This is a previously unknown compact group of YSOs. The isophotes of the YSO associated with the IRAS source in the UKIDSS K image are somewhat elongated, which indicates its binarity (see Figure 4 **f)**).

IRAS 19213+1723. This compact cluster has already been identified in NIR [68]. Our estimated radius value, however, is smaller. The IRAS and MSX sources appear to be associated with an object of the Class II evolutionary stage.

IRAS 19388+2357. As in the previous case, this group has already been identified in NIR [68]. The YSO, the most likely associated with the IRAS source, is detectable only in the longer MIR wavelength range (see Figure 4 **h)**). This is a close pair of YSOs for which the brightness increase on the images in the longer wavelength range significantly exceeds that of the other objects in the cluster. Photometric data is only available in [5.8] and [8.0] μm bands, which is insufficient for their classification.

IRAS 20056+3350. This cluster has already been included in a list of stellar clusters discovered by Gaussian filtering of the UKIDSS survey (G071.312+00.827, [186]). We obtained its radius and the number of members. The YSO associated with the IRAS in NIR is resolved only in the K band, where its binarity is also quite evident. According to WISE photometric data, it can be classified as YSO with Class I evolutionary stage [104].

IRAS 20188+3928. This group is the central part of the G077.46+01.76 cluster [26], which was discovered on 2MASS images. At least three YSOs at Class I evolutionary stage are located in vicinity of the IRAS source.

IRAS 20198+3716. This young group is the richest one in our list and it is the central part of the Berkeley 87 cluster, which has an age of 1-2 Myr [195]. In vicinity of the IRAS source, the four objects are embedded in the gas-dust matter standing out with their brightness in the *Spitzer* images (see Figure 4 **m)**). The “3” object has the smallest IR excess and according to the 2MASS data, it is closest to the IRAS source. Objects “1” and “2” can be classified as Class I evolutionary stage objects. It is possible that IRAS is associated with the group of these young stars as a whole.

IRAS 18360-0537. This group was also identified in [147] (G3CC 59) as a deeply embedded cluster. The two YSOs are closest to the IRAS source and according to the MIR photometry data, they can be classified as Class I evolutionary stage objects.

IRAS 18517+0437. This region is the poorest in our list of young groups, which is identified here for the first time. The brightest object, surrounded by a spherical nebula, is the closest to the IRAS and does not have essential IR excess according to NIR data. It can be classified as Class III evolutionary stage object. Notably, corrected coordinates of the IRAS [1] are far from the above-mentioned star. It can be assumed that its counterpart YSO is deeply embedded in a gas-dust matter indistinguishable in the IR images.

IRAS 19374+2352. A group of young stars has previously been discovered in this region [68], but we were not able to identify it in NIR. Instead, this group is well resolved in MIR (see Figure 4 **p)**). A star with Class I evolutionary stage is associated with the IRAS source. Its elongated isophote suggests that it is a binary object.

IRAS 19092+0841. The group of YSOs in this region was also identified in [68] and was classified as a deeply embedded cluster. The object associated with the IRAS and MSX sources is still ambiguous. According to the photometric data, the brightest point object with an IR excess is a star with Class I evolutionary stage (see Figure 4 **q)**). There is, however, a bright IR nebula in the immediate surrounding of the IRAS and MSX sources, where we were not able to identify any point sources. It is possible that a deeply embedded YSO is located in this region that is not detectable in the images.

IRAS 18174-1612. We were not able to identify any stellar objects associated with the IRAS source in this region.

IRAS 18385-0512. In the immediate vicinity of the MSX, but at a considerable distance from the IRAS, there is a triplet of YSOs that can be classified as Class I evolutionary stage objects based on the WISE data.

IRAS 19410+2336. We were not able to discover a region with high surface stellar density in the neighborhood of this source. [147], however, identified a deeply embedded stellar cluster. Three YSOs at Class I evolutionary stage are close to the MSX and IRAS sources. Moreover, “A” is a binary object. The indications for the YSOs are the same as in [196].

IRAS 20126+4104. One YSO at Class I evolutionary stage is associated with the MSX and IRAS.

Table 3. Parameters of the central YSOs

N	YSO	$\Delta1('')$	$\Delta2('')$	$\Delta3('')$	α_{MSX}	α_{IRAS}	Class
(1)	(2)	(3)	(4)	(5)	(6)	(7)	(8)
GPS UKIDSS							
1	-	-	-	-	1.8	1.6	Binary
1.1	CPM 15 A	6.1	6.0	2.5	-	-	-
1.2	CPM 15 B	7.1	6.2	5.8	-	-	Class I
2	J05201643+3637186[1]	4.3	0.1	1.1	2.1	2.6	Class I
3	J05390992+3545172[1]	7.3	4.0	2.0	2.8	2.2	HAe/Be
4	J18173150-1206179[1]	15.5	0.5	0.6	2.9	2.5	Class I
5	J18342090-0559458[1]	16.5	1.6	1.9	2.4	2.6	Class I
6	-	-	-	-	3.6	2.8	Group
6.1	J18531775+0124547[1](B)	5.3	12.9	13.7	-	-	HAe/Be
6.2	G034.4043+00.2297[2](C)	14.3	5.1	6.1	-	-	Class I
6.3	G034.4035+00.2287[2](D)	16.7	1.3	2.1	-	-	Class I
6.4	G034.4032+00.2279[2](E)	19.6	2.4	1.4	-	-	b, Class I
7	J19132208+1050538[1]	2.3	3.5	1.3	3.7	1.5	b, Class I
8	J19233728+1729024[1]	4.4	0.6	1.0	3.0	1.5	HAe/Be
9	G059.8329+00.6719[2]	5.3	31.7	3.3	3.1	2.0	b, ?
10	J200731.37+335940.9[3]	2.7	2.8	4.0	2.3	2.1	b, Class I
11	-	-	-	-	4.7	1.6	Group
11.1	J20203907+3937586[1]	7.5	5.4	6.0	-	-	Class I
11.2	J20203934+3937552[1]	3.3	2.1	2.9	-	-	Class I
11.3	J20203902+3937531[1]	4.3	3.4	2.9	-	-	Class I
12	-	-	-	-	3.7	1.5	Group
12.1	J20214157+3726061[1]	14.3	16.1	14.6	-	-	Class I
12.2	J20214129+3726057[1]	12.8	15.6	6.0	-	-	Class I
12.3	J20214128+3725559[1]	3.2	6.2	2.9	-	-	HAe/Be ?
12.4	J20214085+3725359[1]	17.8	16.8	2.9	-	-	HAe/Be

Table 3. continued

GLIMPSE							
13	-	-	-	-	3.7	2.5	b
13.1	G026.5123+00.2822[2]	15.8	9.0	5.6	-	-	Class I
13.2	G026.5116+00.2844[2]	14.3	11.3	8.0	-	-	Class I
14	J18541340+0441210[1]	12.5	36.2	3.5	2.2	2.9	?
15	G059.6024+00.9119[2]	20.8	1.2	3.5	3.0	2.2	b, Class I
16	G043.0377-00.4513[2]	18.4	16.9	14.6	1.5	3.1	Class I
A cluster not found							
17	-	-	-	-	4.4	2.8	-
18	J184113.21-050900.3[3]	19.4	39.6	1.1	3.7	2.4	t, Class I
19	-	-	-	-	3.3	2.0	Group
19.1	J19431084+2344047[1] (B)	11.5	5.3	6.6	-	-	Class I
19.2	J19431121+2344039[1] (A)	6.1	0.6	1.3	-	-	b, Class I
19.3	J19431120+2344117[1] (C)	8.3	7.3	7.0	-	-	Class I
20	J201426.10+411331.5[3]	2.1	0.0	3.2	5.0	1.6	Class I

(1) the sequence number of IRAS source (see Table 2), (2) name of a point source in the 2MASS[1], GLIMPSE[2], and WISE[3] databases, (3-5) shift of the YSO from corrected coordinates of IRAS source [1] and MSX sources, (6,7) the slope of SED ($\alpha = (log\lambda_1 F_{\lambda_1} - log\lambda_2 F_{\lambda_2})/(log\lambda_1 - log\lambda_2)$) in the MSX and IRAS bands (60 - 100 μm), (8) classification of the object based on the c-c diagram (b - binary, t - triplet).

3.3. Conclusions

According to NIR and MIR data, out of 20 IRAS sources, we were able to statistically identify compact groups of YSOs in the vicinity of 12 and 4 IRAS sources, respectively. This represents 80% of the overall number of regions that were studied and is substantially higher than the results based on data from the 2MASS survey (see **INTRODUCTION**). In four regions (IRAS 18151-1208, 18316-0602, 18517+0437, and 19110+1045) clusters were discovered for the first time. The five identified compact groups (IRAS 05168+3634, 05358+3543, 18507+0121, 20188+3928, and 20198+3716) are substructures of more extended clusters and presumably are knots of secondary (or higher) star formation waves. We were not able to identify a compact group in the vicinities of 4 IRAS sources (IRAS 18174-1612, 18385-0512, 19410+2336, 20126+4104). The IRAS 18385-0512 and 19410+2336 sources, however, are associated with a triplet and at least four YSOs, respectively, which can essentially be considered as small groups. In the case of IRAS 20126+4104, the YSO has the highest SED slope for an MSX source, i.e., it is presumably in a very early stage of evolution and is surrounded by a massive gas-dust envelope which causes considerable absorption in the immediate vicinity. This is why the group was not found in NIR range. Unfortunately, this region was not included in the GLIMPSE survey and the WISE images do not have sufficient resolution for stellar group identification in the vicinity of this YSO. The situation for IRAS 18174-1612 is somewhat different. We were unable to identify it with a stellar object. Its source is presumably a very young and deeply embedded protostar that could only be detected at longer wavelengths or the source could be of extragalactic origin.

There is no significant difference between the distances and interstellar extinction values which is also characterised by α_{IRAS} value for the range in which the clusters have been detected. The radii and surface stellar densities of the detected clusters have significant scatter and lie in the ranges of 0.3-2.7 pc and 4-1360 stars/pc^2, respectively. The latter value of the density in the IRAS 20198+3716 corresponds to a near distance estimate (0.9 pc). It is much higher than the density in the other groups. We can assume that the far distance estimate (5.5 pc) is more realistic. The surface stellar density distribution of the detected clusters corresponds to the peak in the density distribution of low-mass YSOs at relatively close distances (<500 pc) for young clusters [**34**].

It is known that IRAS sources coordinates have substantial errors, which makes difficulties to cross-match in other wavelengths. Thus, for identifying the YSOs associated with them, we used corrected coordinates of the IRAS sources [**1**]. In most cases, distance from the IRAS to the most probable (with respect to its photometric parameters) YSO is considerably smaller (Table **3**); this increases the accuracy of identification.

The identified YSOs are not always located at the center of the discovered cluster (see Figure **4**). This can be explained by density gradient of the interstellar medium in the cluster, which significantly distorts the real picture. In 12 out of 19 identified regions (~63%), the IRAS sources are associated with a binary or even a group of YSOs.

In contrast to insignificant difference in the distance and interstellar extinction among the discovered groups, there are some differences in the evolutionary stages of the central object. Among the central objects identified in NIR, there are YSOs that can be classified as objects with a later Class II evolutionary stage based on their JHK photometric parameters. Four of these are substructures of a more extended stellar cluster.

Taking into account the above-mentioned results, at least for these 20 regions, we may conclude that around middle- and high-mass YSO, in a certain stage of evolution, a group of young stars was formed and with modified selection criteria (depth of images, longer wavelength range), the percentage of detected groups should increase. A similar result was obtained for 20 near located clusters [41].

Undoubtedly, the search and detection of compact star-forming regions can be considered as just an initial stage of research. There is a whole series of questions that will require a more detailed approach and more extensive databases: at what evolutionary stage YSO forms compact groups in its vicinity? Does the richness of a cluster depend on the mass and age of the central object as, for example, in clusters concentrated around Herbig Ae/Be stars [193]? How do the properties of clusters depend on the parameters of the surrounding medium? Do the properties of the young stellar population reflect which process dominates in the formation of the cluster, namely continuous self-condensating or external triggering?

To address the above issues, we chose and studied in detail three star-forming regions from the list given in Table 2. The main selection criteria of these three regions are their considerable extent and multicomponent complex structure, which implies the presence of several local nests of star formation. The regions are little studied, but at the same time, there is sufficient observational data for their detailed study. Besides, the preliminary studies have shown that the star-forming regions differ in their stellar composition and structural properties [16]. As a result, we have chosen three star-forming regions, namely IRAS 05137+3919, 05168+3634, and 19110+1045. The next chapter presents the results of a detailed analysis of these regions, which includes the study of both the stellar population and the ISM. These star-forming regions are also of interest because they are located at large distances, which will allow us to test the capabilities of the databases at our disposal.

CHAPTER 4

4. REGIONS FOR DETAIL STUDY

The following Sections present a detailed study of the above-mentioned 3 star-forming regions. All three regions, despite their certain differences, are united by one aspect - they are regions of active star formation. The aims of the study are: 1) determination of ISM parameters, namely the distribution of $N(H_2)$ hydrogen column density and T_d dust temperature; 2) the search for young stellar clusters; 3) identification of the clusters' members using their IR properties; 4) investigation of structural properties of the young stellar clusters; 5) determination of age and age spread of the clusters' members; 6) construction of the Luminocity Functions (LFs) and Mass Functions (MFs) for the clusters.

4.1. IRAS05137+3919

4.1.1. Introduction

One of the subjects of this thesis is a young stellar cluster located in the vicinity of IRAS05137+3919 associated with the CPM 15 YSO [36]. Different manifestations of active star formation have been observed in this region, which includes H_2O [190], OH [61], CH_3OH [191], and NH_3 [142] masers, HCO^+ and CS emission [146], and CO and H_2 outflows [203]; [196]. A group of young stars with a high density has been identified, on the bases of the 2MASS survey and NICMOS-3 observations, in the immediate vicinity of IRAS05137+3919 [110]; [68]. Based on IR and submillimeter data, the luminosity of CPM 15 is $L = 2.55x10^5\ L_\odot$ and it has an O8 spectral type [145]. However, there are large differences in the distance estimations for CPM 15, and this undoubtedly affects the luminosity estimation. The distance estimates based on radio observations have a large variation: from ~4.4 kpc (^{13}CO, ^{12}CO, [42], [200]) to 10.8 kpc (NH_3, [142]). Several authors used 11.5 kpc value to determine the luminosity of this object.

4.1.2. Dust emission

Figure 6 shows the colour-composite image of three Hi-GAL bands (PACS 160 μm and SPIRE 350 and 500 μm) covering the IRAS05137+3919 star-forming region. The region stands out sharply in terms of brightness. Figure 15 shows two images of the region in MIR range (*Spitzer* 3.6 and 4.5 μm). In the 3.6 μm band, the central region surrounding the CPM 15 nebula is saturated. Significant brightness in both IR ranges testifies that there are both relatively hot and cold components of gas-dust matter in this region. The hotter component is concentrated mainly in the central region, i.e. in the vicinity of the CPM 15, while the colder component extends noticeably further.

Using the modified single-temperature blackbody fitting (see Section 2.2), we have determined the main parameters (N(H_2) and T_d) of cold composing gas-dust matter in the IRAS05137+3919 star-forming region. Figure 7 shows the N(H_2) and T_d distribution maps. The density and temperature maps show that the star-forming region stands out sharply in terms of brightness with a relatively high density and temperature, which fully includes the identified young stellar cluster (see text below). The maxima of both column density (~1.0×10^{23} cm^{-2}) and dust temperature (22 K) are located in the cluster centre and almost coincide with position of the IRAS source. Towards the periphery, both parameters decrease up to 2.2×10^{22} cm^{-2} and 11 K. The mass is 3.1×10^4 $M_\odot$ for 4.5 kpc distance, and 1.8×10^5 $M_\odot$ for 11 kpc distance.

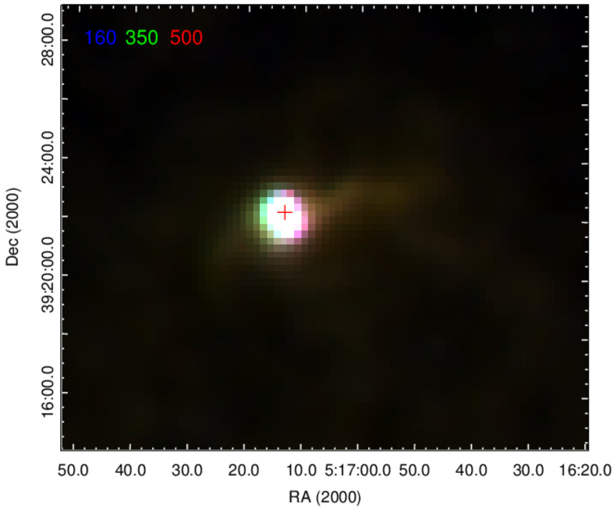

Figure 6. Colour-composite image of IRAS05137+3919 star-forming region: 160 μm (blue), 350 μm (green), and 500 μm (red). The position of the IRAS source is indicated by red cross.

In general, the χ^2 has a low value ($\chi^2 < 0.01$). However, in the center of the stellar cluster, close to the IRAS source, the χ^2 noticeably increases, reaching 0.16 value. This discrepancy with the modified single-temperature blackbody model is explained by several reasons. These include, for example, the fact that in this region, as already shown above, there is a mixture of hot and cold gas-dust matter. Undoubtedly, the radiation from the hot component also affects the long-wavelength range. As a consequence, the single-temperature model cannot give a sufficiently accurate estimate of the parameters. In addition, the final result is also influenced by the fact that different structures of the star-forming region are located along the line of sight.

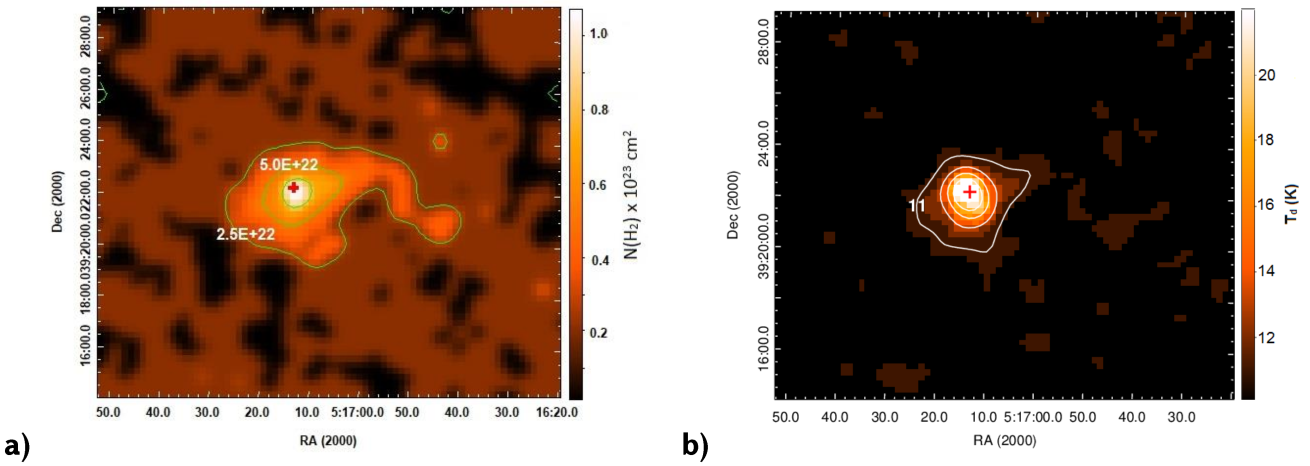

Figure 7. Maps of column density (**a**) and dust temperature (**b**) of the region surrounding IRAS05137+3919 source. On the $N(H_2)$ map, the external isodense corresponds to the $2.5x10^{22}$ cm^{-2} value and the interval between isodences is also $2.5x10^{22}$ cm^{-2}. On the T_d map the external isotherm corresponds to 11 K and interval between isotherms is 2.5 K. The positions of IRAS sources are marked by crosses.

4.1.3. Young stellar population

To confirm the existence of a cluster in the vicinity of the IRAS source, we constructed a radial distribution of the stars density relative to the position of IRAS05137+3919 as shown in Figure 8, which yielded a 1.5′ radius for the cluster. We conducted further studies for IRAS05137+3919 star-forming region within a determined 1.5′ radius. The stellar density in the region with a radius of 1.5′ is 38 stars/arcmin^2, which is twice the density of the field (19 stars/arcmin^2). The excess number of stellar objects in the cluster is 115. It should be noted that our estimate of the cluster radius is in good agreement with earlier works [110]; [68].

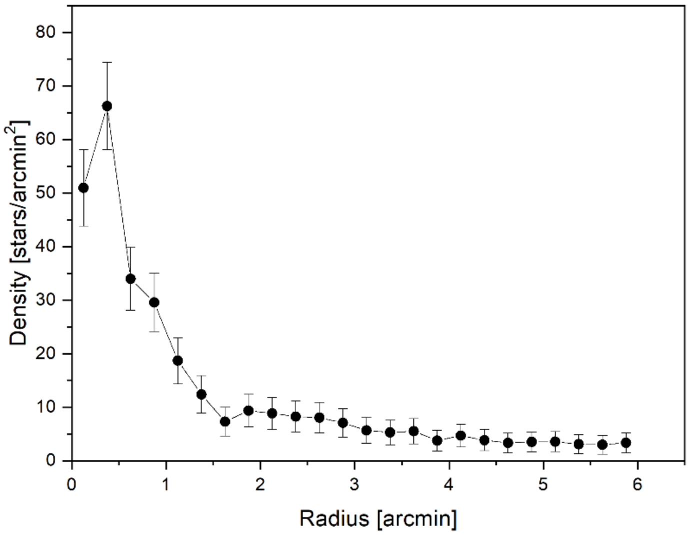

Figure 8. Radial distribution of the stellar density relative to IRAS05137+3919. Vertical lines are standard errors.

The selection of YSOs in the IRAS05137+3919 star-forming region was based on two c-c diagrams, namely (J-H) versus (H-K) and (J-K) versus [3.6]-[4.5], which are shown in Figure 9 **a)** and **b)**. All indications in Figure 9 **a)** and **b)** correspond to the ones presented in Figure 3 **a)** and **c)**. Figure 9 **a)** shows the positions of 253 objects located within 1.5′ radius relative to the IRAS05137+3919 source. 72 YSO candidates were selected using the (J-H) versus (H-K) c-c diagram.

Only 79 objects out of 253 above-mentioned ones have been detected in the *Spitzer* 3.6 and 4.5 μm bands. Figure 9 **b)** shows positions of those 79 objects in (J-K) versus [3.6]-[4.5] c-c diagram. Totally, 33 YSO candidates were selected using the (J-K) versus [3.6]-[4.5] c-c diagram.

We selected as YSOs those objects with IR excess by at least one c-c diagram. In total, we selected 84 YSOs. This is almost 1.5 times greater than the earlier estimate of the cluster members [68]; this can be explained by the image depths we have used. The selection criterion does not, of course, reveal all YSOs in this region. Nevertheless, it is ~73% of excess over the number of stars in the field. In Figure 9 **a)** and **b)** the selected YSOs are marked by blue circles and black dots are non-classified ones.

Table 4 shows the photometric data of 84 YSOs and stellar magnitudes in the *Spitzer* 3.6 and 4.5 μm bands are available only for 33 YSOs. We constructed SEDs for these 33 YSOs using the SED fitting tool (see Section 2.4). This procedure was done using wavelengths ranging from 1.1 μm to 22 μm, in particular, J, H, K (UKIDSS); B, R, J, H, K (2MASS); 3.6 and 4.5 μm (*Spitzer* IRAC), and 3.4, 4.6, 12, and 22 μm (WISE). The SED fitting process was carried out for both distance estimations: 4.5 and 11 kpc. We used A_v and distance ranges of 0.1–20 mag, and 4–5 kpc and 10–12 kpc, respectively. The best model was chosen from all proposed models by the SED fitting tool. Notably, the χ^2 value for the overwhelming majority does not exceed 30. Table 5 presents parameters of 33 YSOs at near and far distances: 4.5 and 11 kpc.

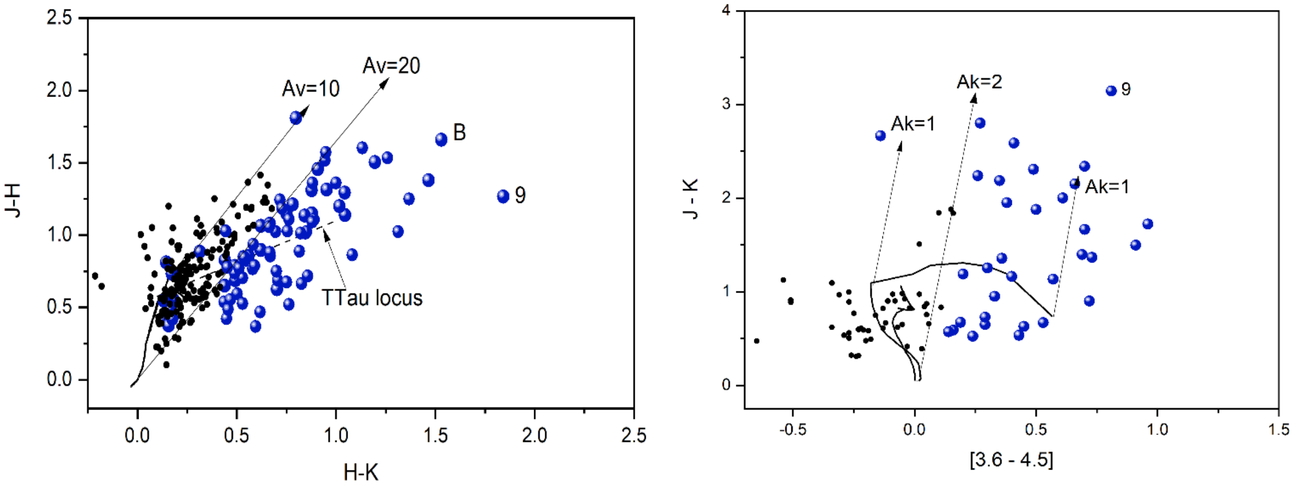

a) **b)**

Figure 9. **a)** (J-H) vs. (H-K) and **b)** (J-K) vs. [3.6]-[4.5] c-c diagrams for IRAS05137+3919 star-forming region [151]. All lines are the same as in Figure 3. The blue circles are selected YSOs and black dots are non-classified ones. Not all non-classified objects are presented in these diagrams. Southwest component B of CPM15 YSO and the reddest object with number 9 are labeled.

Table 4. NIR and MIR photometric data of selected YSOs in IRAS05137+3919

N	α(2000) (hh mm ss)	δ(2000) (dd mm ss)	J (mag)	H (mag)	K (mag)	[3.6] μm (mag)	[4.5] μm (mag)
(1)	(2)	(3)	(4)	(5)	(6)	(7)	(8)
1	05 17 08.97	39 22 38.5	18.18	17.06	16.23	15.79	15.41
2	05 17 10.35	39 21 06.8	15.71	15.35	15.19	14.93	14.69
3	05 17 10.41	39 21 09.6	17.25	16.72	16.58	14.93	14.74
4	05 17 10.73	39 22 24.2	16.68	16.14	15.95	16.02	15.73
5	05 17 10.75	39 21 40.4	18.75	17.44	16.51	16.04	15.78

Table 4. continued

6	05 17 10.96	39 22 02.2	15.99	15.32	14.83	14.04	13.64
7	05 17 11.13	39 21 47.0	17.42	15.97	15.09	13.82	13.12
8	05 17 11.56	39 21 56.9	15.87	14.99	14.38	14.04	13.13
9	05 17 11.93	39 21 44.7	17.36	15.71	14.22	10.98	10.17
10	05 17 11.98	39 21 47.8	14.30	13.78	13.12	10.58	10.13
11	05 17 12.01	39 21 52.2	16.74	15.60	14.58	11.52	10.86
12	05 17 12.20	39 21 55.5	15.87	14.79	13.48	11.99	11.26
13	05 17 12.37	39 21 40.9	18.93	17.55	16.13	14.09	13.82
14	05 17 12.45	39 22 21.3	13.99	13.58	13.40	13.02	12.86
15	05 17 12.47	39 23 05.2	17.32	16.18	15.44	14.71	14.21
16	05 17 12.54	39 21 49.6	17.87	16.37	15.21	12.64	12.78
17	05 17 12.55	39 22 36.2	14.78	14.38	14.24	14.21	13.78
18	05 17 12.67	39 22 04.6	15.98	15.14	14.59	14.17	13.48
19	05 17 12.69	39 21 55.4	18.06	16.26	15.48	14.13	13.72
20	05 17 12.87	39 23 29.9	16.43	15.95	15.78	15.78	15.49
21	05 17 12.88	39 22 34.9	16.83	16.10	15.93	15.33	14.61
22	05 17 13.28	39 22 34.2	18.89	17.60	16.58	14.74	14.25
23	05 17 13.41	39 22 43.2	17.87	16.80	16.14	15.57	14.61
24	05 17 13.44	39 21 52.6	14.28	14.00	13.48	11.88	11.31
25	05 17 13.75	39 21 18.3	17.09	16.21	15.90	15.74	15.54
26	05 17 14.09	39 21 22.1	17.63	16.81	16.38	16.47	16.17
27	05 17 14.46	39 21 22.1	19.42	18.23	17.24	15.90	15.55
28	05 17 14.46	39 22 00.0	19.30	17.73	16.81	15.04	14.34
29	05 17 15.18	39 21 02.8	17.42	16.92	16.75	15.90	15.37
30	05 17 15.85	39 22 16.2	17.20	15.99	15.23	14.54	14.29
31	05 17 15.99	39 22 34.8	18.12	17.30	16.76	15.66	15.30
32	05 17 16.36	39 22 12.1	18.60	17.46	16.60	15.88	15.27

Table 4. continued

33	05 17 19.27	39 23 02.6	17.78	16.98	16.83	16.41	16.08
34	05 17 06.6	39 21 40.4	19.86	18.78	17.92	-	-
35	05 17 06.68	39 22 32.9	18.88	18.19	17.66	-	-
36	05 17 06.82	39 22 43.4	19.88	19.03	17.97	-	-
37	05 17 07.19	39 22 47.1	19.67	19.16	18.42	-	-
38	05 17 07.39	39 23 12.1	18.67	18.32	17.73	-	-
39	05 17 07.99	39 21 16.9	17.96	17.55	17.11	-	-
40	05 17 08.06	39 21 08.6	18.32	17.81	17.28	-	-
41	05 17 08.15	39 22 05.2	20.00	18.49	17.56	-	-
42	05 17 08.68	39 21 39.1	19.68	18.97	18.13	-	-
43	05 17 09.03	39 22 43.9	18.07	17.23	16.70	-	-
44	05 17 09.1	39 21 35.3	19.05	18.17	17.37	-	-
45	05 17 09.45	39 23 28.9	19.17	18.71	18.11	-	-
46	05 17 09.6	39 21 40.4	20.08	18.48	17.37	-	-
47	05 17 09.78	39 21 39.6	19.37	18.36	17.53	-	-
48	05 17 09.92	39 22 46.1	18.23	17.51	17.02	-	-
49	05 17 10.86	39 21 28.4	17.66	16.48	15.77	-	-
50	05 17 11.00	39 21 33.7	18.80	18.12	17.43	-	-
51	05 17 11.23	39 22 02.2	18.74	18.21	17.78	-	-
52	05 17 11.29	39 21 51.5	18.93	17.68	16.35	-	-
53	05 17 11.58	39 20 58.4	19.54	18.89	18.08	-	-
54	05 17 11.61	39 22 20.0	18.36	17.51	16.85	-	-
55	05 17 11.79	39 21 54.9	16.72	15.49	14.78	-	-
56	05 17 11.85	39 21 52.4	17.22	16.21	15.38	-	-
57	05 17 11.96	39 22 24.8	19.25	18.48	18.03	-	-
58	05 17 12.01	39 21 52.2	16.74	15.60	14.58	-	-
59	05 17 12.62	39 22 26.1	19.24	18.14	17.39	-	-
60	05 17 12.63	39 21 14.8	19.53	19.05	18.60	-	-

Table 4. continued

61	05 17 12.74	39 21 20.1	19.06	18.28	17.70	-	-
62	05 17 13.24	39 22 22.8	17.71	16.69	15.41	-	-
63	05 17 13.36	39 21 54.2	15.33	14.75	14.25	-	-
64	05 17 13.36	39 21 17.8	19.08	18.15	17.57	-	-
65	05 17 13.45	39 22 55.6	19.42	18.37	17.72	-	-
66	05 17 13.45	39 22 01.8	18.00	16.99	16.19	-	-
67	05 17 13.48	39 22 23.6	17.15	15.80	14.82	-	-
68	05 17 13.59	39 21 54.2	15.98	14.96	14.52	-	-
69	05 17 13.66	39 22 21.8	18.50	17.40	16.53	-	-
70	05 17 13.7	39 22 19.0	13.45	12.19	10.28	-	-
71	05 17 13.79	39 22 34.1	19.08	18.32	17.82	-	-
72	05 17 14.12	39 21 53.9	18.60	17.84	17.27	-	-
73	05 17 14.38	39 22 21.9	17.62	16.10	14.87	-	-
74	05 17 14.39	39 21 11.2	17.89	17.15	16.47	-	-
75	05 17 14.46	39 21 59.9	16.82	15.77	15.16	-	-
76	05 17 14.58	39 20 52.7	19.67	18.65	17.91	-	-
77	05 17 15.76	39 22 39.3	18.90	18.06	17.54	-	-
78	05 17 15.84	39 22 46.4	19.53	18.66	18.01	-	-
79	05 17 15.85	39 22 16.2	17.20	15.99	15.23	-	-
80	05 17 15.88	39 21 56.2	19.00	17.65	16.78	-	-
81	05 17 16.63	39 22 48.6	18.71	18.17	17.71	-	-
82	05 17 17.87	39 21 38.6	19.11	18.09	17.41	-	-
83	05 17 19.49	39 21 33.4	18.81	18.03	17.55	-	-
84	05 17 19.76	39 21 40.5	19.71	19.04	18.31	-	-

Notes. (1) - ID number of YSO, (2),(3) – position taken from the UKIDSS survey, (4)–(8) - apparent magnitudes

Based on the parameters for these YSOs, we can make some conclusions for the whole region. For the near distance, the average A_v and distance values are 1.8 mag and 4.4 kpc, respectively, and the median age is 1.6x10^5 yr. The YSOs have spectral classes from B6 to M2 with respect to their bolometric luminosity and temperature. For the far distance, the average A_v and distance values are 3.0 mag and 10.9 kpc, respectively. The median age is the same as in the near distance case: 1.9x10^5 yr and the spectral classes of the stars are in B0 to G0 interval, which is, of course, explained by the difference in the distance estimate.

Table 5. Parameters derived from [171] models SED fitting for two distances.

N	4.0 < D < 5.0 kpc						10.0 < D < 12.0 kpc					
	A_v (mag)	LogD (kpc)	Age (yr)	Mass ($M_\odot$)	T (K)	L ($L_\odot$)	A_v (mag)	LogD (kpc)	Age (yr)	Mass ($M_\odot$)	T (K)	L ($L_\odot$)
(1)	(2)	(3)	(4)	(5)	(6)	(7)	(8)	(9)	(10)	(11)	(12)	(13)
1	2.6	0.60	4.3e+4	0.2	2844	0.5	12	1.00	9.7e+5	5.4	17490	650
2	0.1	0.67	5.2e+5	3.3	4870	21	2.8	1.02	3.5e+6	5.2	17089	579
3	0.2	0.60	9.9e+4	1.6	4270	24	4.5	1.06	8.3e+6	3.5	13009	121
4	0.1	0.67	1.6e+5	0.2	3051	1.2	1.5	1.00	3.2e+6	2.9	10643	77
5	3.2	0.60	1.3e+5	0.2	3018	0.5	12	1.04	2.8e+6	3.8	8736	75
6	0.6	0.60	2.3e+6	2.0	4873	4.0	2.5	1.02	7.2e+5	3.3	4965	18
7	0.4	0.70	4.0e+3	3.1	4246	128	4.1	1.08	4.8e+4	8.5	6156	127
8	2.1	0.67	1.2e+5	5.3	4629	128	2.3	1.00	2.2e+5	6.2	6070	333
9	3.9	0.60	5.7e+3	4.1	4217	258	7.3	1.00	1.4e+4	13.1	6881	7310
10	3.9	0.60	1.8e+6	7.6	13257	3040	4.4	1.02	2.0e+6	12.0	28197	10900
11	2.4	0.60	1.3e+6	4.5	4595	131	0.1	1.08	2.3e+5	7.0	11317	1600
12	0.4	0.60	9.1e+4	1.5	4269	2.5	1.8	1.02	2.3e+4	10.8	6660	3900
13	1.9	0.63	5.4e+4	0.5	3760	7.1	3.7	1.06	1.9e+4	1.2	4100	44
14	1.8	0.67	2.9e+6	2.7	6347	31	0.3	1.04	3.3e+5	4.4	4952	82
15	1.8	0.60	2.0e+4	1.0	4024	18	1.9	1.04	9.0e+3	3.6	4300	139
16	1.0	0.67	1.9e+5	5.1	4772	97	0.1	1.04	9.7e+4	6.4	4655	257
17	0.9	0.67	7.2e+6	1..9	6458	13	4.5	1.00	1.4e+6	3.3	5032	35
18	2.6	0.65	2.0e+6	1.8	4708	5.1	2.6	1.06	2.3e+5	6.2	6070	333

Table 5. continued

19	3.1	0.70	7.1e+4	3.8	4622	106	16	1.00	4.6e+3	4.5	4206	297
20	0.2	0.67	7.2e+6	1.4	4787	1.3	4.2	1.00	1.7e+6	2.3	4921	5.8
21	1.4	0.63	9.4e+4	2.0	4327	30	2.0	1.08	1.6e+4	9.7	4768	1840
22	2.0	0.63	3.5e+4	0.7	3925	7.4	4.4	1.08	5.5e+4	3.6	4410	101
23	1.5	0.67	1.1e+4	1.1	4089	2.7	0.3	1.04	1.0e+4	7.4	4370	502
24	5	0.63	4.1e+6	5.5	17504	669	4.5	1.00	3.7e+5	6.3	14311	1540
25	1.5	0.63	1.6e+6	0.6	3848	61	2	1.04	8.3e+4	4.8	4480	141
26	1.1	0.65	3.6e+5	1.6	4455	12	4.6	1.06	1.9e+5	2.8	4517	41
27	4.4	0.65	4.5e+5	1.0	4217	4.2	6.1	1.04	6.4e+6	3.3	12689	104
28	2.1	0.60	3.3e+5	2.7	4660	21	1.0	1.02	5.4e+4	5.7	4782	183
29	0.1	0.63	1.2e+6	4.9	16482	14	0.1	1.00	2.5e+4	3.6	4380	110
30	3.7	0.60	6.8e+6	5.0	12318	644	31	1.00	3.3e+5	5.5	6006	212
31	1.0	0.67	1.3e+4	3.9	4313	195	6.5	1.02	7.2e+3	7.3	4814	621
32	1.4	0.65	6.0e+4	1.9	4299	44	19	1.08	5.0e+4	2.7	4361	111
33	0.6	0.70	5.8e+4	0.6	3878	4.8	5.7	1.00	9.4e+4	2.2	4341	41

Notes. (1) ID number of members taken from Table 4, (2)-(7) parameters obtained by SED fitting tool for χ^2_{best} model at distances of 4-5 kpc; (8)-(13) parameters obtained by SED fitting tool for χ^2_{best} model at distances of 10-12 kpc.

4.1.4. Colour-magnitude diagrams

The colour-magnitude diagram (CMD) is a useful tool for studying the nature of the stellar population within star-forming regions and for estimating its spectral types. The distribution of the 33 identified YSOs in the K versus (J-K) CMDs are shown in Figure 10. We used the K versus (J-K) diagram because with this combination we get the maximum contrast between the IR excess produced by the presence of the disk, which affects mostly K, and the interstellar extinction, which has a greater effect on J. The zero-age main sequence (ZAMS, thick solid curve) and PMS isochrones for ages 0.1 and 1 Myr (thin solid curves) are taken from [183]. We used the conversion table of [101]. The J and K photometry of the selected YSOs are corrected for two different distances: 4.5 and 11 kpc.

According to the COBE/DIRBE and IRAS/ISSA maps [179], the average interstellar extinction toward the IRAS source is A_v = ~1.7 mag. This value well corresponds to A_v value in the near distance case obtained with SED fitting tool. Correction of the J and K magnitudes for the members was done with the interstellar extinction estimated with SED fitting tool for each distance case, i.e. A_v = ~1.8 and 3.0 mag for the near and far distances, respectively.

NIR excess, shown in the c-c diagrams (Figure 9), is usually caused by the presence of disks around young stars; thus, by incorporating theoretical accreting disk models, the excess effect on the CMD can be accurately represented by vectors of approximately constant slope for disks around Class II T Tauri stars. The components of the vector are (1.01, –1.105) and (1.676, 1.1613) in magnitude units [128]. More massive YSOs are usually much more embedded than T Tauri stars, thus, this correction is unlikely to apply to such objects. However, the presence of a spherical envelope around the disc should cause a greater decrease in J–K for the same variation in the K than in the case of a 'naked' disc [44]; accordingly, the [128] correction can be used to obtain a lower limit of stellar mass in the region for two different distances. For the total content of the region based on the excess vector analysis, the following result is derived. At a distance of 4.5 kpc, approximately 80% of the total content have <1 solar mass, and the remaining 20% of objects have 1–3 solar masses. At a distance of 11 kpc, approximately 42% of the total content of the region have <1 solar mass, and about 51% of objects have 1–7 solar masses. There are only six objects with mass >7 solar masses.

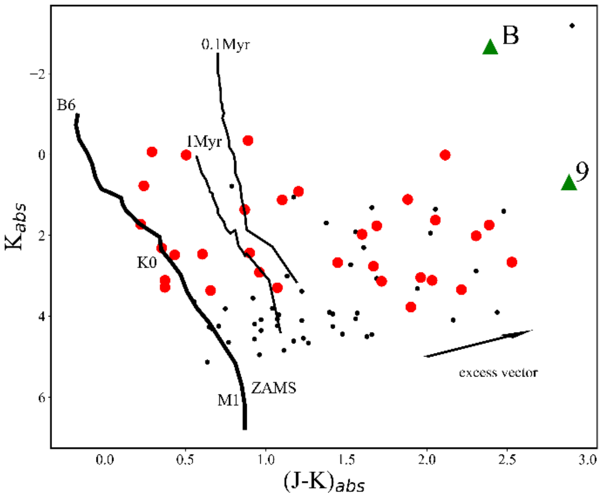

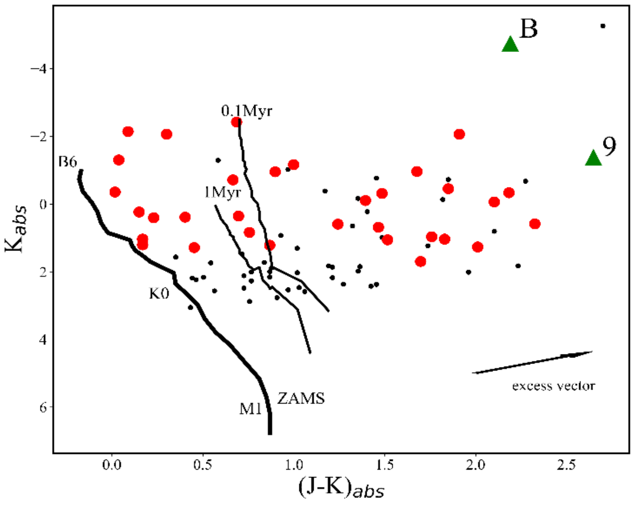

Figure 10. K vs. (J–K) colour-magnitude diagrams for identified YSOs in the IRAS05137+3919 region. The PMS isochrones for the 0.1 and 1 Myr [183] and ZAMS are drawn as solid thin and thick lines, respectively. The positions of a few spectral types are labelled. The J and K magnitudes of the YSOs are corrected for the interstellar extinctions determined according to SED fitting tool and distances 4.5 kpc (*left panel*) and 11 kpc (*right panel*), respectively. Red circles are selected YSOs with constructed SED and no-SED objects are black dots. Southwest component B of CPM15 YSO and the reddest object with number 9 are labeled. The solid arrow indicates the average slope of NIR excesses caused by circumstellar discs [128].

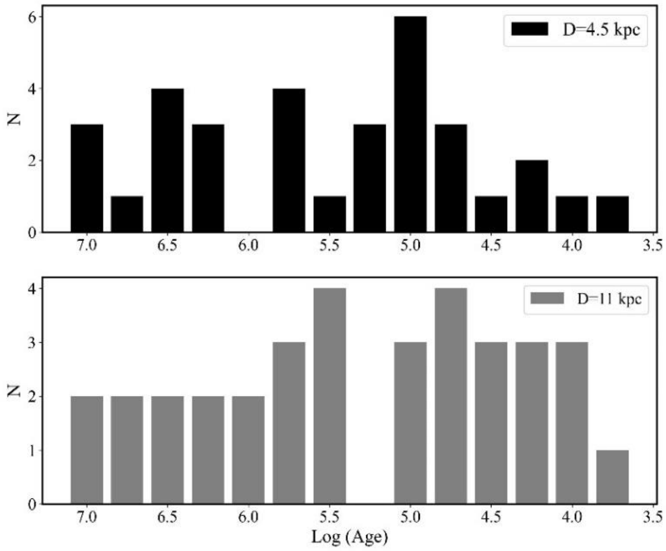

Figure 11. Histogram of evolutionary ages (by the SED fitting tool) for members at the near (*top panel*) and the far distances (*bottom panel*). The bin size corresponds to Log (Age) = 0.25.

Histograms for the different distances are shown in Figure 11. The histograms clearly show that the evolutionary age of stars in the region have very wide spread for both cases. The overwhelming majority of them are located in the range from 10^4 to 10^7 years. On the basis of the above, it can be assumed that, in general, the star formation process in the considered region is sequential. Based on the results obtained from different star formation regions, it seems that some clusters owe their origin to an external triggering shock and other clusters can be formed as independent condensations in molecular clouds (e.g. [66]; [205]). If the star formation is triggered, the age spread of new generation stars should be small, while in self-initiated condensations the age spread of young stellar clusters is large [205]. Indeed, many careful studies of star-forming regions find no clear evidence or at most very moderate age spreads of several Myr [125]. Moreover, in some cases, the measured age spread is less than the crossing time, which is well consistent with the scenario of the fast trigger nature of the star formation process ([164], and ref. therein). However, the age spread of the considered star-forming region is much larger, and, therefore, it can be concluded that the stellar population is formed as a result of independent condensations in the parent molecular cloud.

4.1.5. K luminosity function

The luminosity function in the K-band (KLF) is frequently used in studies of young clusters and star-forming regions as a diagnostic tool of the IMF and the star formation history of their stellar populations [205]; [120]; [100]. The observed KLF is a result of the IMF, the PMS evolution, and star-forming history; thus, the KLF slope is a potential age indicator of young clusters [115]. The KLF can be defined as $dN(K)/dK \propto 10^{\alpha K}$, where α is the slope of the power-law and N(K) is the number of stars brighter than K mag. The KLF slope is estimated by fitting the number of YSOs in 1 mag bins using a linear least-squares fitting routine. Since the interstellar extinction is independent of stellar mass [138], it does not affect the result; therefore we can use all the sources in the samples to define the slopes without the complication of extinction correction. Therefore, Figure 12 shows the observed KLF of YSOs detected in the region. The calculation of α slope of the KLF yielded 0.18 ± 0.02, which is lower than the typical values reported for young embedded clusters ($\alpha \sim$ 0.4; e.g., [121]; [112]; [23]. There are many studies on the KLFs of young clusters. [138] found similar values of α slopes around the W3 IRS 5 cluster (α = 0.24), and that it is consistent with an age of 0.3 Myr with a Miller-Scalo IMF. In addition, according to the calculation of [132], α values between 0.2 and 0.28 are consistent with an age range of 0.1-3 Myr. Therefore, the age of all IRAS05137+3919 star-forming region can be estimated between 0.1 and 3 Myr.

4.1.6. Structure of the cluster

Figure 13 shows the local density (LD) distribution for all selected YSOs (N = 84). An LD has been decided for each object on the surface with a radius equal to the distance to the closest n-th star. In this case, the LD was determined for the 8th nearest object. The LD value for the first isodense exceeds the field density with 3σ value. (0,0) position corresponds to the coordinates of IRAS05137+3919 source which is indicated by a star symbol. Figure 13 also contains the positions of SCUBA [57] and MSX sources which are indicated by triangles and circles, respectively.

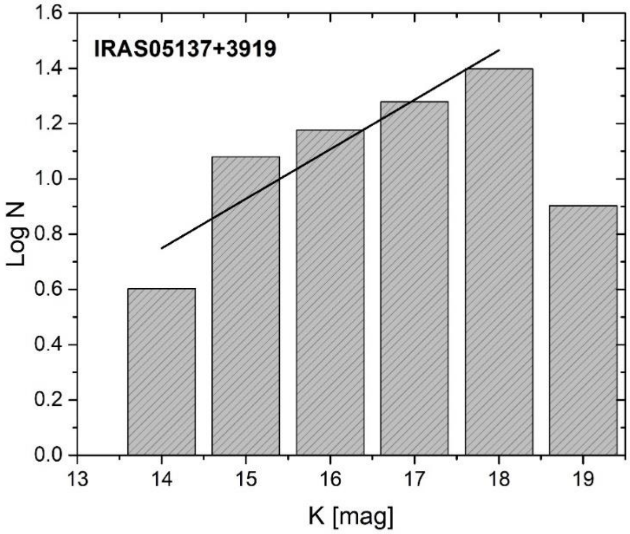

Figure 12. K luminosity function derived for the selected YSOs as a histogram of the number of stars vs. apparent K magnitude. The bin size corresponds to 1 mag.

The LD distribution shows that the YSOs are distributed nonuniformly over the field of the cluster and form two clearly distinct subgroups: A and B located near the emission peaks in the IR, submillimeter, millimeter, and centimeter ranges (Mol8A, Mol8B, [146]; [145]). Notably, the maximum surface stellar densities are shifted slightly from the emission peaks, as well as from IRAS05137+3919 source. We examined each group separately.

Group A. The central object in group A is CPM 15 YSO, which has a luminosity of L = 2.55x10^5 $L_\odot$ for a distance of 11.5 kpc. However, in UKIDSS and [196] images, it can be clearly seen that this object is binary (see Figure 14). The southwest component (component B, [196]) is resolvable in the UKIDSS all three bands, while the northwest component A is essentially unresolvable in the J and H bands but has almost the same brightness as component B in the K band.

Using secondary standards with the help of DAOPHOT package in IRAF program, we have measured the stellar magnitudes of these stellar objects: J = 13.5 mag, H = 12.2 mag, K = 10.8 mag (component B); K = 10.6 mag (component A). The error in the stellar magnitudes is ~0.1 mag. In the (J-H) versus (H-K) c-c diagram (Figure 9) component B falls in the region of Herbig Ae/Be stars.

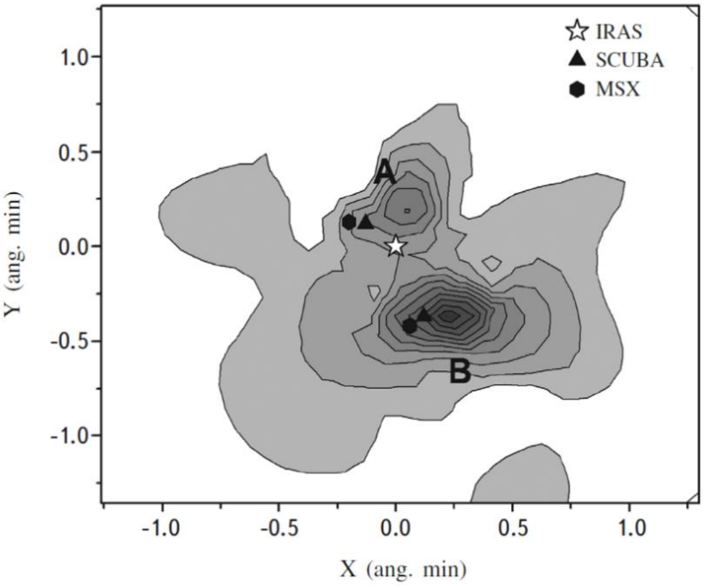

Figure 13. The local density distribution of YSOs [151]. The triangles, circles, and star show the location of SCUBA, MSX and IRAS sources, respectively.

We have also used the J, H, K photometric data to construct SED [172]; [171] of component B for both distance cases. Table 6 shows the results of SED fitting tool. It should be noted that the accuracy of SED parameters constructed with three data points is very low, but in this case, there is no other photometric data available, since the emission in longer wavelengths (MSX, SCUBA, radio range) is associated with the pair of objects. In the first case (4 < D < 5 kpc), according to the mass and accretion material ratio of the star, it can be classified as a middle mass young star, specifically, as a Herbig Ae/Be object [95]. Taking into account the relation between the luminosity of the star to the envelope mass surrounding it, in both distance cases the star can be classified as a Class I evolutionary stage object (Class I, [177]). In the near distance case, the luminosity of the star corresponds to B3-B5 spectral types, and in the far distance case - B1-B2 [148]. CPM 15 A has a luminosity in K-band comparable to CPM 15 B, but appears to be a younger object.

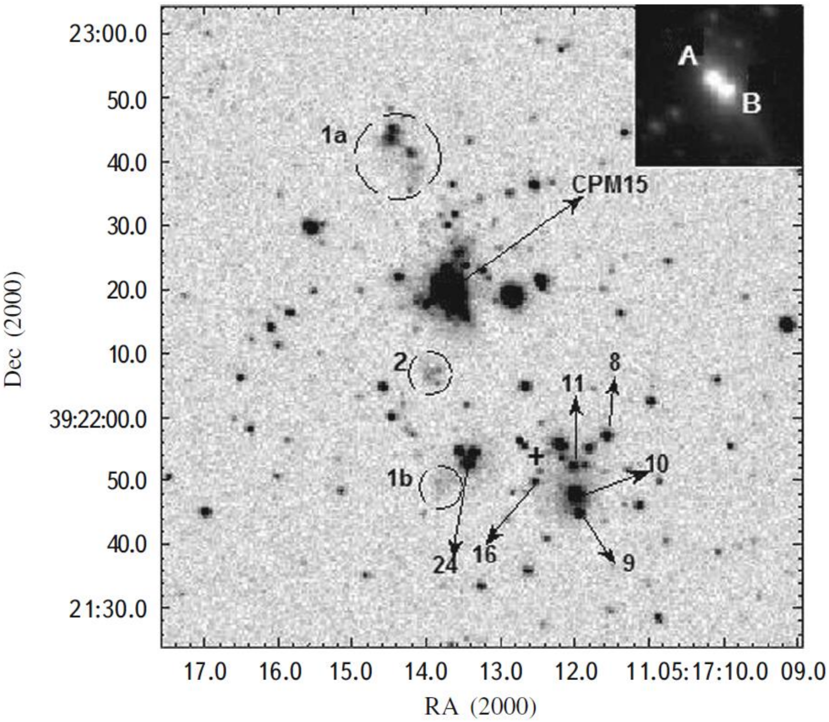

Figure 14. UKIDSS K-band image of IRAS05137+3919 star-forming region [151]. The CPM15 and several important objects are labeled. The second emission peak in the submillimeter and IR ranges are indicated by the cross.

Table 6. Parameters of the CPM 15 B

D (kpc)	χ^2	A_v (mag)	LogD	Age (yr)	Mass ($M_\odot$)	T_{eff} (K)	L ($L_\odot$)	M_{star} ($M_\odot$)	M_{env} ($M_\odot$)
4 < D < 5	1.68	2.0	0.70	1.2×10^5	6.8	5020	517	2.5×10^{-7}	3.2
10 < D < 12	2.73	2.8	1.04	1.7×10^5	7.7	13150	3140	3.4×10^{-8}	4.4

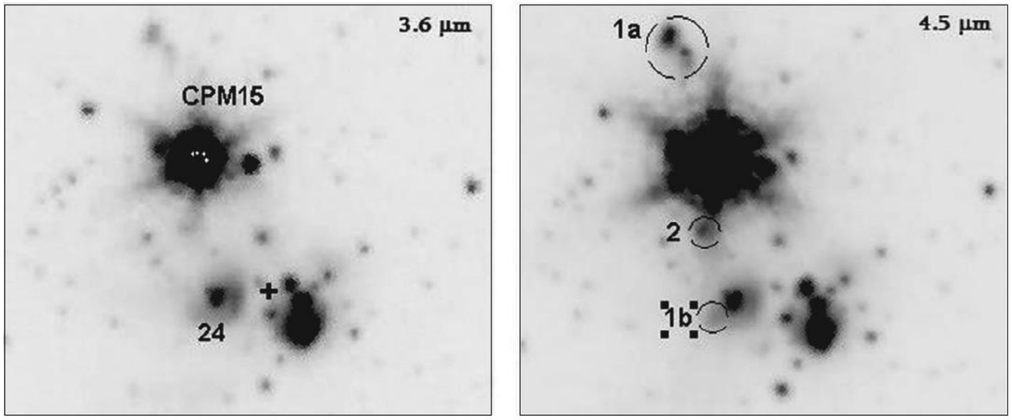

Figure 15. MIR images of the IRAS05137+3919 star-forming region [151]. *Left and right panels* show the region in *Spitzer* 3.6 and 4.5 μm bands, respectively. The indications are the same as in Figure 14.

[196] show that the two components of CPM 15 are the sources of a colimated bipolar outflow detected in H_2 υ= 1– 0 S(1) (2.1218 μm) and Brγ (2.166 μm) spectral lines. Both outflows are visible in MIR wavelengths, in particular, in the *Spitzer* 4.5 μm image (see Figure 15 right panel). In this range there are a significant number of neutral hydrogen emission lines and, in contrast to the other bands, this range is free of PAH emission. For this reason, the diffuse emissions which are relatively bright in this band are likely to be a result of neutral hydrogen shock excitation. The outflows are also seen in the K-band images (see Figure 14) where hydrogen emission occurs in 2.12-2.17 μm range. The indications of the outflows in Figure 14 and Figure 15 are the same as in [196].

Group B. The second group of stars is located around the second emission peak in the submillimeter and IR ranges; their positions are indicated by the cross in Figure 14 and Figure 15. The longer wavelength emissions peak between two nebulae and are not clearly associated with any of the stellar objects in this region. It appears that this radiation is initiated by heated gas-dust material located in this region. The sources of HCO^+ and CS emission are also located in this region [146].

Notably, a significant number of stellar objects with middle and high masses (for the far distance case) are concentrated in the group B. The sequence numbers of these objects from Table 4 and Table 5 are indicated in Figure 14 and Figure 15. One of the youngest objects, namely No. 9, which is located in the nebula and has the highest IR excess in NIR, belongs to this group (see Figure 9).

Object No. 24 is also of great interest in group B. In MIR images (Figure 15), it is clear that this object is surrounded by a spherical nebula and emission intensity from the nebula in the 3.6 μm range is ~1.5 times higher than in the 4.5 μm range. The brightest part of the nebula is located to the west of No. 24 and has the same coordinates as the source of HCO^+ emission with a radial velocity of -26.8 km/s [146]. It is unlikely that the HCO^+ emission source can be the SW part of the colimated bipolar outflow from the CPM 15 A as assumed in [196]. It is known that the jet must have negative radial velocities, while counterjet, which is generally less bright, should have a positive velocity. In this case, the SW part of the CPM 15 A outflow is, indeed, a counterjet. The fact that the maximum emission of HCO^+ occurs right on the brightest part of the spherical nebula suggests that this emission is the result of a collision of the expanding nebula with the interstellar medium. The nebula mass determined from the intensity of HCO^+ emission is 1.1 and 8 $M_{\odot}$ for the two distance cases, respectively [146]. The sizes of the nebula derived from the 3.6 μm image for distances of 4.4 and 10.9 kpc are 0.1 and 0.26 pc, respectively. Assuming that the radial velocity of the HCO^+ emission (26.8 km/s) is the nebula expansion velocity, then its age is 3.7 (D = 4.5 kpc) or 9.5×10^3 yr (D = 10.9 kpc).

As noted above, in the 4.5 μm image (Figure 15), the components of the colimated outflow can be resolved, including 1b which [196] suggests it is part of a bow shock of the outflow from CPM 15A. Its position relative to No. 24 star is such that the shock excitation of hydrogen, in this case, might be initiated precisely by No. 24 star rather than by CPM 15 A.

4.1.7. Conclusions

The analysis of the surface stellar density distribution in the vicinity of IRAS 05137+3919 which was identified in the UKIDSS database revealed a stellar cluster with ~1.5′ radius. The surface stellar density in the cluster exceeds density in the field twice. Based on NIR and MIR photometric data (J, H, K, 3.6 μm, and 4.5 μm), we identified 84 YSOs in the cluster; this is undoubtedly a lower limit of the total number of young stars in the star-forming region. On one hand, this incompleteness is explained by the imperfection of the selection method and, on the other hand, by the large distance to the cluster which would undoubtedly primarily affects on detection of low-mass objects. The selected YSOs are distributed nonuniformly in the star-forming region and form two subgroups; one is located around CPM 15, while the second group contains a significant number of middle-mass objects surrounded by gas-dust nebulae. The maxima of hydrogen column density ($1.0\mathrm{x}10^{23}$ cm^{-2}) and dust temperature (22 K) coincide with position of the IRAS source. From the IRAS to the periphery both values decrease up to $0.25\mathrm{x}10^{23}$ cm^{-2} and 11 K, respectively. The cluster as a whole can be attributed to the R-associations.

There have been substantial discrepancies in the cluster distance in previous papers. Two different distance estimations were examined here: 4.3-4.5 kpc and 10.8-11.5 kpc. Therefore, we considered both distance values constructing SEDs of the YSOs. Nevertheless, the median age for two distances differs insignificantly and equals $1.6\mathrm{x}10^5$ and $1.9\mathrm{x}10^5$ yr, respectively. The KLF of the star-forming region shows unusually low value for the α slope: 0.18 ± 0.02. According to the value of the KLF slope, the age of IRAS05137+3919 star-forming region can be estimated between 0.1 and 3 Myr. So the large spread of the evolutionary ages makes it possible to assume that the star formation process in this region has a continual self-condensing nature.

The distance estimation is very important for the CPM 15 YSO classification associated with IRAS05137+3919; it has been classified as a high-mass YSO with O8 spectral type for 11 kpc distance. Notably, CPM 15 is the source of collimated powerful outflow that is detected in both radio and IR wavelength ranges. It is known that low- and middle-mass YSOs typically have a collimated outflow. This is still an open question for high-mass YSOs ($M > 10\,M_\odot$). To answer this question, it will require sufficiently reliable observational data that includes the precise estimation of luminosity and mass of the object. It should be noted, that with increasing detector resolution, the detection of binary, triplet, and multi-component objects in compact star-forming regions is increasing, which previously were classified as high-mass YSO [103]; [152]. By analogy, CPM 15 YSO turned out to be binary on UKIDSS and [196] images. We were able to classify one of the CPM 15 components as a middle-mass object for both distance cases.

4.2. IRAS05168+3634

4.2.1. Introduction

A star-forming region in the vicinity of IRAS05168+3634 is also known as Mol 9 in the catalogue of [142]. Within a 2 arcmin radius of IRAS05168+3634, three objects have been detected with magnitudes of the

MSX survey [62], one of which is associated with IRAS05168+3634. [203] have discovered a molecular outflow in this region.

IRAS05168+3634 is a luminous young stellar object (YSO) with an estimated L = 24x10^3 L$_\odot$ [196]; it is located in a high-mass star-forming region in the pre-UC HII phase [198]. There have been various detections in the region: H_2O maser emission [203], NH_3 maser emission [142], CS emission [35], a new detection of 44 GHz CH_3OH methanol maser emission [73], the SiO (J = 2–1) line [85], the main lines at 1665MHz and 1667MHz OH maser [173], and four ^{13}CO cores [80]. [143] have detected 6 cm radio emission 102 arcsec away from IRAS05168+3634. Compact HII regions and H_2O maser are sites of ongoing high-mass star formation which have not completely disrupted the surrounding dense, molecular gas. Thus, we have an opportunity to examine the stellar population in its initial configuration, before the rapid dynamical evolution which may occur once the molecular gas is cleared by stellar winds and the expanding region [116].

The embedded stellar cluster in this region was detected in the NIR and MIR by various authors [110]; [68]; [16]. [16] shown that this is a bimodal cluster with 1.5 arcmin radius from the geometric center of the cluster that does not coincide with IRAS05168+3634. One of the subgroups is concentrated around IRAS05168+3634 and it should be noted that it does not contain a rich population compared to other concentrations.

The distance estimations of this region are different. A kinematic distance was estimated at 6.08 kpc [142] based on systemic local standard of rest (LSR) velocity V_{LSR} = -15.5±1.9 km/s. The trigonometric parallax of IRAS 05168+3634 with VERA is 0.532±0.053 mas, which corresponds to a distance of $1.88^{+0.21}_{-0.17}$ kpc, placing the region in the Perseus arm rather than the Outer arm [174]. This large difference in estimated distances causes some significant differences in physical parameters for individual members.

4.2.2. Structure of the molecular cloud

The IRAS05168+3634 star-forming region has a more complicated structure in the FIR wavelengths than in the NIR and MIR. The complex structure of the region is clearly visible, especially in the images of the

Herschel PACS 160 μm and SPIRE 250, 350, 500 μm bands. Figure 16 shows the region in different wavelengths from NIR to FIR. Moving toward longer wavelengths in the *Herschel* PACS 160 μm and the SPIRE 250, 350, 500 μm bands images, the cloud filaments surrounding IRAS05168+3634 become more visible and it is obvious that the IRAS05168+3634 star-forming region is not limited in 1.5 arcmin radius from the geometric center [16] but is more extended and is located within a 24 arcmin radius molecular cloud where the center of the molecular cloud is the conditionally selected source IRAS05168+3634. Studying the common star-forming region in the molecular cloud, it turns out that apart from IRAS05168+3634, there are four IRAS sources (IRAS 05184+3635, 05177+3636, 05162+3639, and 05156+3643) embedded in the same molecular cloud. On the MIR [4.5] μm band image can be clearly seen that these IRAS objects, like IRAS05168+3634, have a concentration of sources around them. There is very little information about these IRAS sources. IRAS 05184+3635 and 05177+3636 are associated with dark clouds DOBASHI 4334 and 4326, respectively [58]. [42] assessed the distances of IRAS 05184+3635 and 05177+3636 based on the ^{13}CO velocities: -17 km/s and -15 km/s, respectively, as a result of which both IRAS 05184+3635 and 05177+3636 were evaluated at the same 1.4 kpc distance. The latter value coincides with the distance of IRAS05168+3634 based on trigonometric parallax. This also indicates that these IRAS sources are most likely to be found in the same molecular cloud. On the other hand, [200] estimated the distance of IRAS05184+3635 based on the CO (J = 1 - 0) line parameters, taking into account the same -17 km/s velocity value, at a distance of 9.4 kpc. Notably, it is hard to say which of the estimated distances is correct. There are two objects near IRAS05177+3636 detected at submillimeter wavelengths [57]. IRAS05162+3639 is associated with the H_2O maser [190]. A high proper motion star has been detected in the LSPM-NORTH catalog 0.35 arcmin from the IRAS05156+3643 [126] probably compatible with IRAS05156+3643 within the error bars.

We have constructed the distribution map of stellar surface density within a 48′x48′ region to investigate the structure of each concentration in the molecular cloud, using photometric data of the *Herschel* PACS Point Source Catalog: 160 μm and Extended Source List (red band). The density was determined simply by dividing the number of stellar objects in a 200″x200″ area with a step size of 100″. Figure 17 shows the distribution map of stellar surface density based on *Herschel* PACS 160 μm photometry.

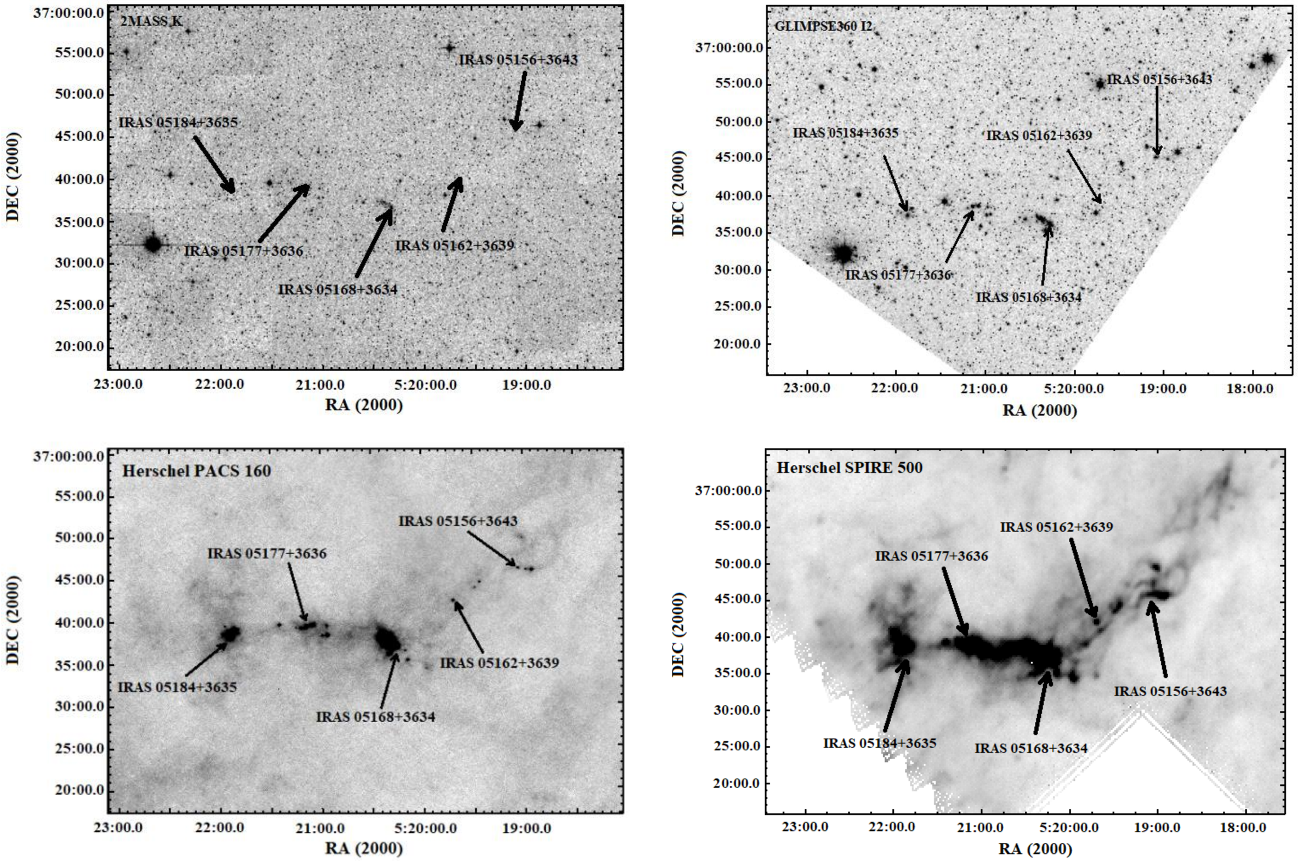

Figure 16. The IRAS05138+3634 star-forming region at different wavelength ranges. *Top left* and *right panels* show the region in NIR (2MASS K-band) and MIR (GLIMPSE 360 I2-band) wavelengths, respectively. The *bottom left* and *right panels* show the region in FIR wavelengths: *Herschel* PACS 160 μm and SPIRE 500 μm, respectively. The positions of five IRAS sources are indicated by arrows.

In the case of the homogeneous distribution of stars in the field, it is known that the number of stars is comparable to the surface area occupied by those stars [2]. We wanted to determine how much the distribution of stars in this field differs from the homogeneous distribution. Table 7 shows the surface area of all subregions according to the isodences in Col. 2 and the number of stars on those surface areas in Col.3. The labels S_{TR} and S_{Total} are the total surface area of five subregions and the surface area within a 24 arcmin radius (IRAS05168+3634 is considered the center), respectively. The ratios of S_{TR}/S_{Total} = 0.02 and N_{TR}/N_{Total}=0.7 indicate what fraction of the surface area within a 24 arcmin radius is the total surface area of the subregions and how much of the objects in the whole field are on the total surface area of the subregion, respectively.

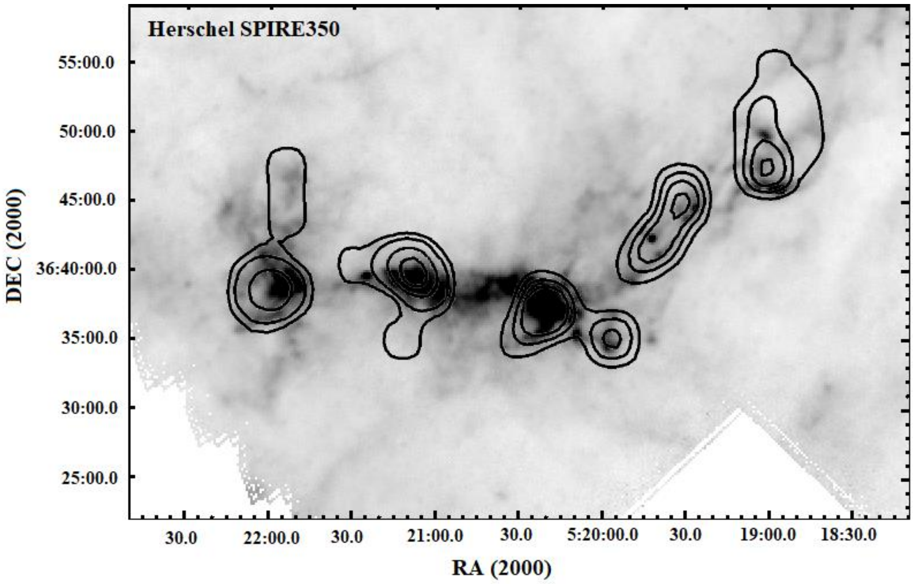

Figure 17. Stellar surface density distribution based on *Herschel* PACS 160 μm photometry. The stellar surface density distribution map is overplotted on the *Herschel* SPIRE 350 μm image. The surface density of the last isodences exceeds the average value of the field surface density on 1σ.

Table 7. Sizes and contents of the subregions.

Name	Surface area (arcmin^2)	Objects
(1)	(2)	(3)
IRAS 05184+3635	5.245	6
IRAS 05177+3636	10.072	7
IRAS 05168+3634	11.14	7
IRAS 05162+3639	5.384	6
IRAS 05156+3643	10.068	6
-	S_{TR} = 41.909	N_{TR} = 32
-	S_{Total} = 1808.64	N_{Total} = 43

Notes. (1) Name of the subregions, (2) approximate surface area of each subregion based on *Herschel* PACS 160 μm catalogue data, (3) number of objects in each subregion based on *Herschel* PACS 160 μm catalogue data.

From these values, it is possible to estimate the difference between the distribution of stars in our field and the homogeneous distribution. As a result, the distribution of stars in our field is 35 times different from the homogeneous distribution, which is a fairly high value. On the other hand, the distribution of sources in the field repeats the shape of the molecular cloud seen in FIR wavelengths, which suggests that the distribution of these subregions is not accidental, that is, they are connected to each other and belong to the same molecular cloud. From this, we can conclude with a high probability that all five IRAS star-forming regions are at the same distance. Since only the IRAS05168+3634 star-forming region has estimated distances (see Section 4.2.1), we can say that IRAS 05184+3635, 05177+3636, 05162+3639, and 05156+3643 are also located at a distance of 6.08 kpc (kinematic estimation) or $1.88^{+0.21}_{-0.17}$ kpc (based on the trigonometric parallax). These distance estimations are used in future calculations.

4.2.3. Dust emission

The $N(H_2)$ and T_d maps of the wider region surrounding five IRAS sources (05168+3634, 05184+3635, 05177+3636, 05162+3639, and 05156+3643) are shown in Figure 18. On the maps, the outer contours correspond to 0.9×10^{23} cm^{-2} (that exceeds the average $N(H_2)$ of the surrounding molecular cloud by σ) and 11 K, respectively. The maps show that the star-forming region, which includes five IRAS objects, clearly stands out against the background of the surrounding molecular cloud both with a higher density and temperature. The relatively hotter gas-dusty matter forms dense condensations around IRAS objects. An exception is the IRAS05162+3639 sub-region, near which on the $N(H_2)$ map there is practically no region with a relatively higher density. In this regard, around IRAS05162+3639 source, in essence, no group of YSOs has been identified, but only 5 stars (see Section 4.2.4). In addition, in the vicinity of IRAS05162+3639 and IRAS05156+3643 sources, in contrast to the other three IRAS sources, no increase in temperature is observed. In general, in the whole star-forming region T_d varies from 11 to 24 K, and $N(H_2)$ - from ~1.0 to 4.0×10^{23}cm^{-2}. A detailed analysis of each sub-region is given below.

In general, the χ^2 within the star-forming region is relatively small: 0.01–0.02. This is most likely because the temperature regime in this region is more suitable for the model we have applied [139]. However, directly in the center of IRAS05168+3634 sub-region, the χ^2 value increases up to ~1.5. In this case, the increase of χ^2 is most likely explained by the quality of the images (see Section 2.2). Moreover, a whole strip of bad pixels passes through the bright condensation in IRAS05168+3634 subregion, which whatever filtering cannot completely remove. This is most likely the reason for the increase in the χ^2 value in this region.

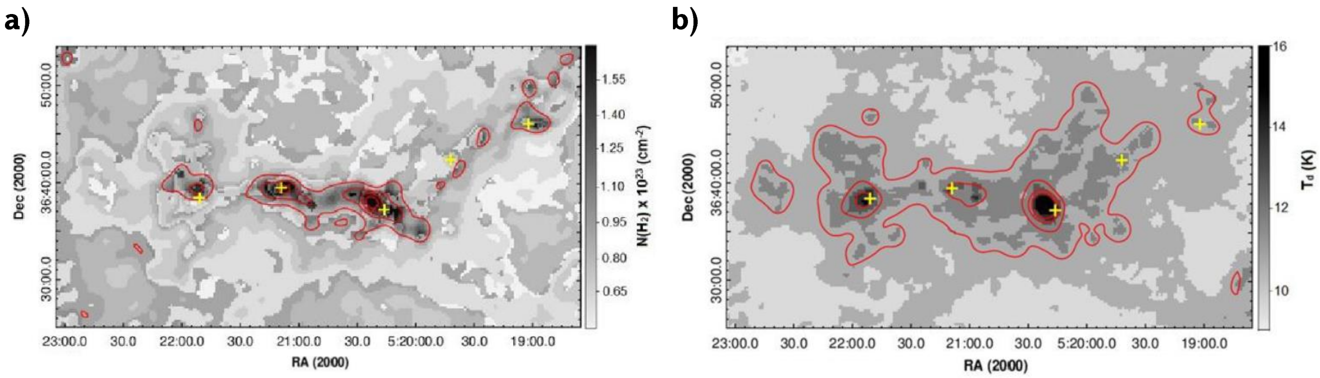

Figure 18. Maps of N(H_2) column density **a**) and T_d dust temperature **b**) of IRAS 05168+3634 star-forming region. On the N(H_2) map the outer isodense corresponds to 0.9x10^{23} cm^{-2}, and the interval between isodenses is ~0.4x10^{23} cm^{-2}. On the T_d map, the outer isotherm corresponds to 11 K, and the interval between isotherms is 1 K. The positions of IRAS are marked by crosses.

4.2.4. Stellar population

The IR excess object identification in this star-forming region was carried out with four c-c diagrams, namely (J-H) versus (H-K), K-[3.6] versus [3.6]-[4.5], [3.4]-[4.6] versus [4.6]-[12], and [3.4]-[4.6] versus [4.6]-[22]. Figure 19 shows the mentioned c-c diagrams where all the indications correspond to the ones presented in Figure 3 **a)**, **b)**, **f)**, and **g).** We added to our list those objects classified as YSOs in at least two c-c diagrams.

In total, we selected 1224 YSOs within a 24 arcmin radius, and they are indicated with filled circles in c-c diagrams (Figure 19). IRAS and MSX sources are indicated by triangles and squares, respectively, and they are labeled in the diagrams. Unfortunately, with this kind of selection of YSOs we cannot find the exact number of YSOs. T Tauri objects with comparably small amounts of NIR excesses may be located in the reddening band, and therefore are excluded from the selection. On the other hand, there can be fore-/background objects among the selected YSOs.

Figure 20 shows the distribution of classified YSOs in the field. Class I and Class II objects are indicated by filled circles and crosses, respectively. It can be clearly seen from the image that Class II objects are distributed more homogeneously on the field than Class I objects, which are located in certain areas and show clear concentrations. This confirms the assumption that, unlike the Class II objects, Class I objects did not have enough time to leave their birthplaces after formation. There are several Class I objects in the field that are far from the main concentrations, and because the distribution of Class I objects is closer to the initial distribution it can be argued that the Class I objects either have some measurement errors in magnitudes or that they do not belong to the molecular cloud. Since the distribution of stars and clearly visible concentrations repeat the shape of the molecular cloud, the probability of superposition is very small because in that case there would be other similar concentrations in the field, which are not detected outside the molecular cloud filaments.

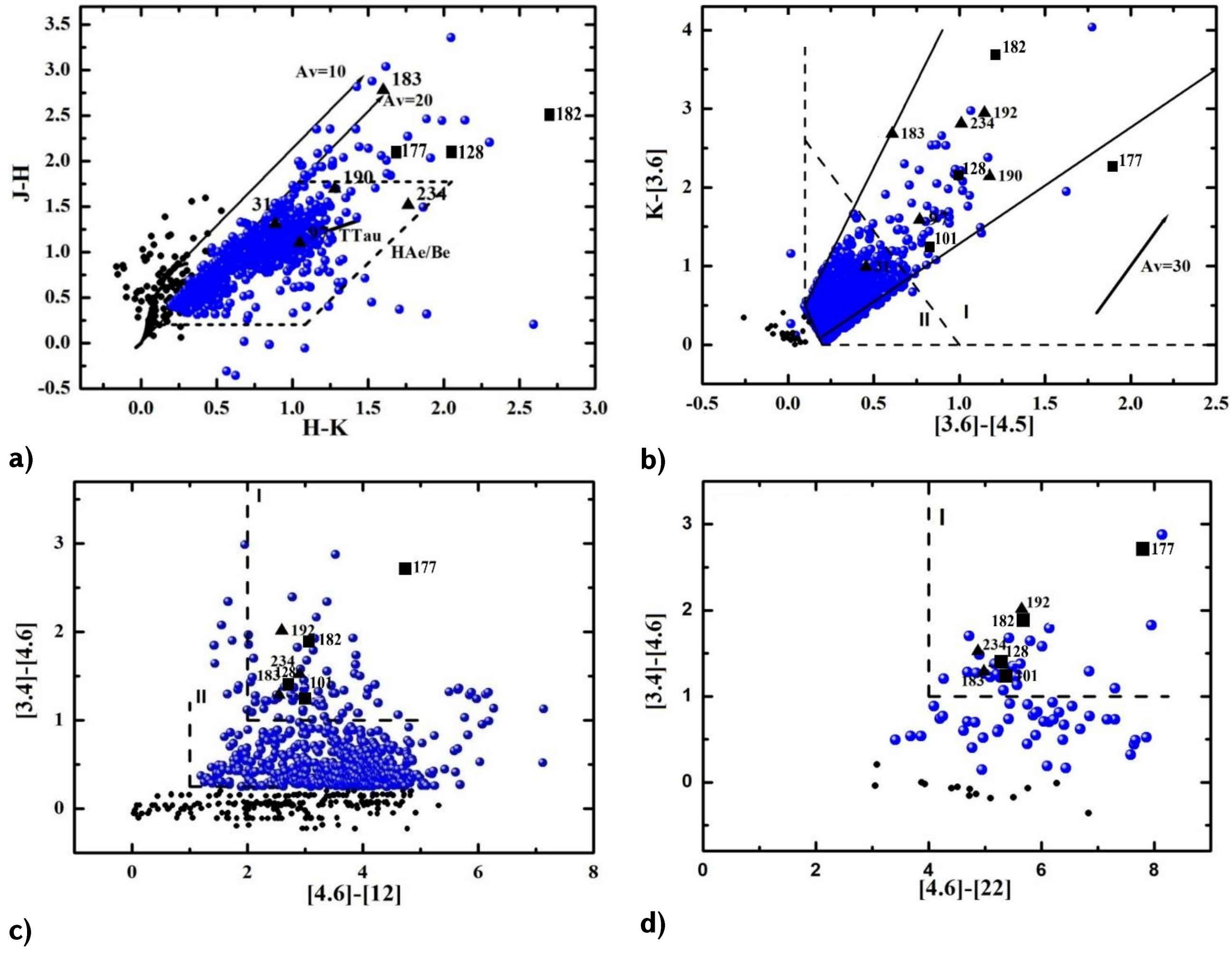

Figure 19. (J–H) vs. (H–K) **a),** K-[3.6] vs. [3.6]–[4.5] **b),** [3.4]–[4.6] vs. [4.6]–[12] **c),** and [3.4]–[4.6] vs. [4.6]–[22] **d)** c-c diagrams for the IRAS05168+3634 star-forming region [156]. All the lines in diagrams are the same as in Figure 3. The blue circles are selected YSOs and black circles are unclassified ones. Not all unclassified objects are presented in these diagrams. IRAS and MSX sources are indicated by triangles and squares, respectively, and they are labeled (see Table 9 and Table 10).

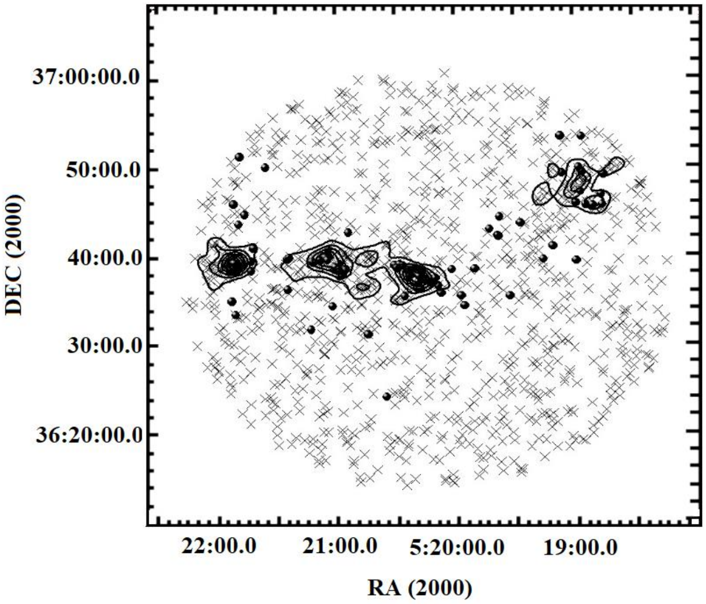

Figure 20. Stellar surface density distribution based on c-c diagrams [156]. Class I and Class II evolutionary stage objects are indicated by filled circles and crosses, respectively.

Table 8. Geometric centers of subregions

IRAS	α(2000) (hh mm ss)	δ(2000) (dd mm ss)	α(2000) (hh mm ss)	δ(2000) (dd mm ss)	Radius (arcmin)
(1)	(2)	(3)	(4)	(5)	(6)
05184+3635	5 21 53.2	36 38 20.4	5 21 52.6	36 39 07.1	2.5
05177+3636	5 21 09.4	36 39 37.1	5 21 02.8	36 38 28.5	3.5
05168+3634	5 20 16.4	36 37 18.7	5 20 22.3	36 37 33.9	3
05162+3639	5 19 38.4	36 42 25.0	5 19 38.4	36 42 25.0	0.25
05156+3643	5 19 03.6	36 46 15.7	5 19 04.0	36 48 02.0	2.8

Notes. (1) Name of subregions, (2),(3) coordinates of IRAS sources, (4),(5) coordinates of geometric centers, (6) radius of each subregion according to YSOs surface density distribution in the molecular cloud.

Since the region is quite large, the probability of being fore-/background objects within the selected Class II objects is very high, and in the case of Class I objects that possibility is small as they are not detected outside the molecular cloud filaments. In order to minimize the number of incorrect Class II objects, further investigations will only be performed on concentration areas. For that purpose, we have constructed a map of the distribution of stellar surface density within a 48′x48′ region to investigate the structure and size of each concentration in the molecular cloud, using the coordinates of selected YSOs. The contours of the distribution of stellar surface density are overplotted in Figure **20** and four subregions are clearly seen, each one surrounding one IRAS source. We refined the radius of each subregion relative to their geometric centers based on the density distribution of selected YSOs. The stellar density was determined for each ring of width 0.1′ by dividing the number of stars by the surface area. The radius of the subregions was considered the value from which according to Poisson statistics the fluctuations of the stellar density in the rings become random. Table **8** presents the coordinates of IRAS sources in Cols. 2 and 3, the coordinates of geometric centers are in Cols. 4 and 5, and the radii based on stellar density distribution are in the last column. There is no evidence of a real concentration only around IRAS05162+3639. On the other hand, two objects from the GPS UKIDSS-DR6 catalog were identified with IRAS05162+3639 as a result of a cross-match, i.e., IRAS05162+3639 is probably a binary object, and three more Class I objects are located very close to it, but they do not show any real concentration. Therefore, the 0.25′ value of radius given in Table **8** is conditional and includes these three Class I objects and the binary associated with IRAS05162+3639. As was already mentioned above, the objects within the determined radii will be explored in greater detail, so further studies will be conducted for the 240 YSOs of 1224 selected from c-c diagrams; this total number of objects falls within the already-defined radii of five subregions. However, with this kind of choice, we lose a large number of objects that are actually located in the molecular cloud filaments but are left out of the determined radius of subregions. Otherwise, we would increase the number of nonmembers. Therefore, in this case, it would be possible to insist that the objects belonging to the molecular cloud were chosen as accurately as possible and that each subregion represents a separate star-forming region. Table **9** shows the catalogue of 10 selected YSOs out of 240[1] with NIR and MIR photometry, while Table **10** presents the fluxes for those 10 YSOs which have FIR photometry. In the *Herschel* SPIRE 250, 350, 500 μm catalogs, the photometry of objects

---

[1] The full tables are available in VizieR On-line Data Catalog: J/A+A/622/A38

was determined by four methods: Timeline Fitter value (TML), Daophot, Sussextractor, and Timeline Fitter 2 (TM2). For the slightly extended sources that were accepted in the *Herschel* SPIRE 250, 350, 500 μm catalog, the TM2 value provides the best guess for an extended flux [79]. All selected YSOs in subregions that have measured fluxes at the 250, 350, 500 μm wavelengths are classified as extended sources in the *Herschel* SPIRE 250, 350, 500 μm catalogs. Taking into account the above, only TM2 photometry is presented in Table 10.

Table 9. Members of subregions with NIR and MIR photometry.

ID	α(2000) (hh mm ss)	δ(2000) (dd mm ss)	J (mag)	H (mag)	K (mag)	[3.6] (mag)	[4.5] (mag)	W1 (mag)	W2 (mag)	W3 (mag)	W4 (mag)	CI
(1)	(2)	(3)	(4)	(5)	(6)	(7)	(8)	(9)	(10)	(11)	(12)	(13)
11	5 21 52.1	36 38 5.11	17.54	16.81	16.41	16.25	16.02	-	-	-	-	II
31	5 21 53.2	36 38 20.4	15.48	14.17	13.28	12.29	11.84	-	-	-	-	II/I
85	5 21 8.95	36 39 31.9	13.20	12.27	11.56	9.96	9.31	-	-	-	-	I
96	5 21 9.08	36 39 32.8	14.38	13.29	12.53	-	-	9.15	7.89	5.07	2.89	I
97	5 21 9.39	36 39 37.1	13.25	12.15	11.10	9.52	8.75	-	-	-	-	I
101	5 20 59.6	36 38 26.8	12.76	11.64	10.54	9.31	8.48	9.67	8.41	5.39	3.03	I
128	5 21 5.50	36 39 37.3	15.55	13.45	11.41	9.27	8.27	9.44	8.04	5.31	2.75	I
177	5 20 25.3	36 38 28.8	17.68	15.59	13.91	11.65	9.75	12.21	9.49	4.76	1.70	I
182	5 20 19.6	36 36 22.9	18.41	15.89	13.19	9.52	8.31	9.88	7.99	4.91	2.32	I
183	5 20 16.4	36 37 18.7	14.18	11.40	9.80	7.12	6.52	7.66	6.37	3.83	1.39	I
190	5 19 41.8	36 42 24.6	17.84	16.15	14.87	12.73	11.55	-	-	-	-	I
192	5 19 42.0	36 42 30.0	-	16.59	13.48	10.53	9.39	11.25	9.24	6.64	3.59	I
234	5 19 3.62	36 46 15.7	14.64	13.13	11.36	8.55	7.54	9.05	7.53	4.63	2.66	I
239	5 18 55.5	36 45 59.8	16.7	14.23	12.09	9.92	8.95	10.17	8.87	6.75	4.19	I

Notes. (1) ID number in final list of the sources, (2),(3) position taken from the UKIDSS survey, (4)–(12) apparent magnitudes, (13) classification of YSOs according to c-c diagrams. W1–W4 are four WISE survey bands. The full table is available in VizieR On-line Data Catalog: J/A+A/622/A38.

4.2.5. Colour–magnitude diagrams

Figure 21 shows the distribution of the 240 identified YSOs in the K versus J-K CMDs (see also Section 4.1.4) with different symbols for each subregion. The J and K photometry of the selected YSOs are corrected for two different distances: 6.1 and 1.88 kpc, because, as mentioned above, all subregions with high probability are located at the same distance (see Section 4.2.2).

According to the COBE/DIRBE and IRAS/ISSA maps [179], we have estimated the A_v values toward five IRAS sources provided in Table 11. There is data of observations of ^{13}CO cores, providing N_{H2} = $4.5x10^{21}$ cm^{-2} column density [80], only in the IRAS05168+3634 star-forming region and using the conversion factor between column density and interstellar extinction $N_{H2} = 9.4 \times 10^{20}$ cm^{-2} (A_v mag) [30] have we received a value of $A_v = 4.8$ mag. The average of both interstellar extinction values ($A_v = 4.5$ mag) for the IRAS05168+3634 star-forming region is used to correct the J and K magnitudes. Correction of the J and K magnitudes for the other four regions was done with the interstellar extinction taken from the COBE/DIRBE and IRAS/ISSA maps.

Table 10. Members of subregions with FIR photometry.

ID	Name	[8.28] (mJy)	[12.13] (mJy)	[14.65] (mJy)	[21.3] (mJy)	[12] (mJy)	[25] (mJy)	[70] (mJy)	[160] (mJy)	[250] (mJy)	[350] (mJy)	[500] (mJy)
(1)	(2)	(3)	(4)	(5)	(6)	(7)	(8)	(9)	(10)	(11)	(12)	(13)
31	IRAS05184	109	266	-	-	440	523	1415[a]	-	-	-	-
97	IRAS05177	224	-	-	-	738	1590	-	-	-	-	-
101	G170.7247	171	-	-	-	-	-	814	1444	-	-	-
128	G170.7196	181	-	-	-	-	-	1261	3683	-	-	-
177	G170.6589	159	-	859	-	-	-	5163	-	-	-	-
182	G170.6758	185	662	525	-	-	-	1735	5052[b]	-	-	-
183	IRAS05168	891	1450	1370	2450	1160	6340	4472	11125	-	-	-
190	IRAS05162	-	-	-	-	250	269	1545	2814	-	-	-
192	IRAS05162	-	-	-	-	250	269	1545	2814	-	-	-
234	IRAS05156	455	-	797	-	649	947	853	1128	2031	-	-

Notes. (1) ID number of IRAS and MSX sources taken from Table 9, (2) names of IRAS and MSX sources, (3)–(6) measured fluxes in MSX catalog, (7)–(8) measured fluxes in IRAS catalog, (9)–(10) measured fluxes in *Herschel* PACS 70 and 160 μm catalogs, (11)–(13) measured fluxes in *Herschel* SPIRE 250, 350 and 500 μm catalogs, (a)-Fluxes taken from *Herschel* PACS: extended source list catalog in blue band (70 μm), (b)-Fluxes taken from *Herschel* PACS: Extended source list catalog in red band (160 μm). The full table is available in VizieR On-line Data Catalog: J/A+A/622/A38.

In general, the selected YSOs are distributed to the right of 0.1 Myr isochrones, especially in the case of 6.1 kpc distance, and this distribution confirms that they are YSOs. The YSOs associated with IRAS and MSX sources are located within the range of the largest IR excess sources in both CMDs. Only a few identified as YSOs objects in the CMDs are located to the left (open circles) of ZAMS, which means nonmembership, i.e., they are probably fore-/background objects. At different distances, the numbers of non-members are different, but it must be taken into account that the J and K magnitude corrections we made for objects belonging to an individual subregion using interstellar extinction values estimated toward IRAS sources only, which means those values would be different from the interstellar extinction values toward each object, and as a result, some objects fall left of ZAMS. Thus, those objects were not removed from the list of YSOs (Table 9), but are shown as black circles in both CMDs. The results of the selection with the c-c diagrams and CMDs are presented in Table 11 separately for each subregion depending on the distance.

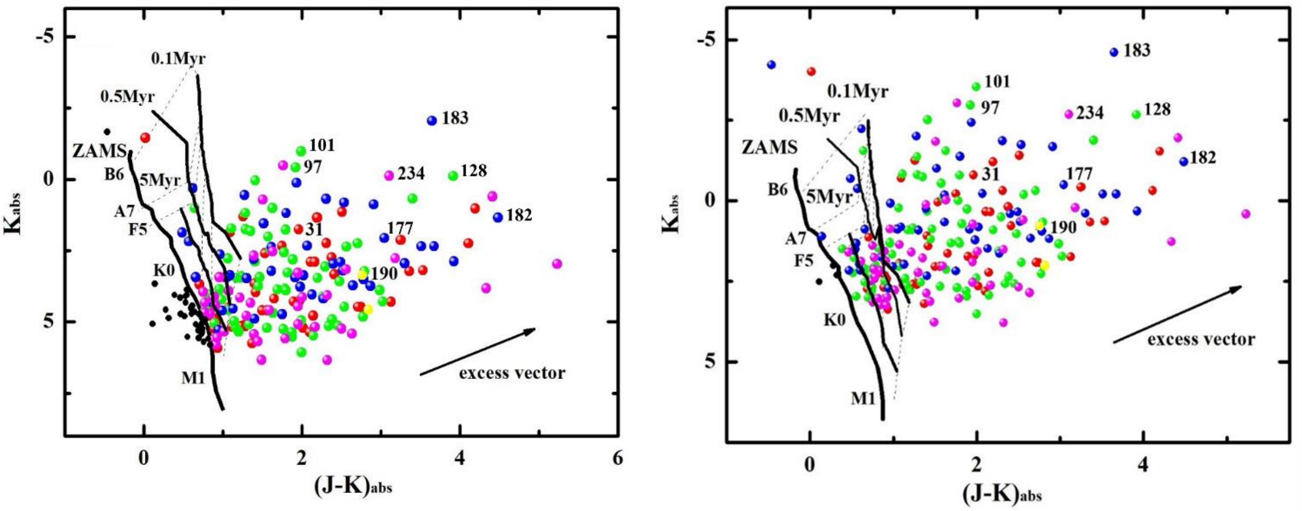

Figure 21. K vs. (J-K) CMDs for the identified YSOs in subregions of IRAS05168+3634 star-forming region. The PMS isochrones for 0.1, 0.5, and 5 Myr by [183] and ZAMS are drawn as solid thin and thick lines, respectively. Dashed lines represent the evolutionary tracks of different masses. The positions of a few spectral types are labeled. The J and K magnitudes of the YSOs are corrected for the interstellar extinctions determined according to the COBE/DIRBE and IRAS/ISSA maps and distances 1.88 kpc (left panel) and 6.1 kpc (right panel), respectively. The arrow indicates the average slope of NIR excesses caused by disks around YSOs, as determined by [128]. The objects belonging to different subregions are shown as follows: IRAS 05184+3635 (red circles), IRAS 05177+3636 (green circles), IRAS 05168+3634 (blue circles), IRAS 05162+3639 (yellow circles), and IRAS 05156+3643 (pink circles). Black circles indicate objects considered members of subregions, but in the CMD they are located to the left of ZAMS. The IRAS and MSX sources are labeled (see Table 9).

According to the results of c-c diagrams and CMDs, within the selected radius of each subregion, the youngest is the IRAS05168+3634 star-forming region since Class I objects represent a fairly large percentage. The next youngest subregion by Class I objects is IRAS05177+3636, and it should be noted, even though there is no real concentration around IRAS05162+3639, that only the Class I objects are inside the conditionally selected radius. Finally, the subregions around IRAS 05184+3635 and 05156+3643 in the outer part of the molecular cloud are the oldest. However, it must be kept in mind that Class II objects have had enough time after formation and have left their birthplaces, so perhaps most of them are beyond the determined dimensions of subregions. Table 11 shows the percentage of Class I objects in each subregion.

Table 11. Characteristics of subregions

IRAS	c-c diagram		CMD 1.9 kpc		CMD 6.1 kpc		ClassI	A_v (mag)	Mass limit ($M_\odot$)		α slope
-	Mem	ClassI (%)	Mem	ClassI (%)	Mem	ClassI (%)	-	-	1.9 kpc	6.1kpc	-
(1)	(2)	(3)	(4)	(5)	(6)	(7)	(8)	(9)	(10)	(11)	(12)
05184	52	21	48	23	52	21	11	1.4	0.3-1.5	0.8-5	0.12±0.04
05177	79	28	65	34	79	28	22	1.34	0.2-2.2	0.7->7	0.2±0.02
05168	57	43	45	54	56	45	24	4.3 (4.5)	0.5-2.5	0.9->7	0.21±0.05
05162	5	-	5	-	5	-	5	1.23	-	-	-
05156	47	20	40	23	47	20	9	1.03	0.2-1.6	0.6-3	0.15±0.04

Notes. (1) Name of subregions, (2) and (3) number of YSOs and the fraction of Class I objects (in percent) according to the CMDs, (4)–(7) number of YSOs and the fraction of Class I objects (in percent) according to the CMDs in different distances, (8) number of Class I evolutionary stage objects, (9) interstellar extinction according to the COBE/DIRBE and IRAS/ISSA maps, (10)–(11) mass completeness limits of each subregion in two distances, (12) α slope of KLF of each subregion.

The distribution of the YSOs on the K versus J-K CMD can be used to estimate their approximate age and mass based on the evolutionary models for objects with ages older than 1 Myr [164]. It is evident from Figure 21 that the YSOs in the molecular cloud, in general, are distributed to the right of 1 Myr isochrone, where the estimation of age and mass of those YSOs will be incorrect.

However, the CMDs show a certain distribution of mass in each subregion. Table 11 shows the results of mass completeness limit determination (see Section 4.1.4). Objects located in the IRAS 05184+3635, 5168+3634, and 05156+3643 star-forming regions are explicitly targeted at specific mass ranges for two distances, and for objects in the IRAS05177+3636 star-forming region, there is no similar dependency. It can be seen in CMDs and from estimated values of mass completeness limit shown in Table 11 Cols. 10 and 11. For the total content of four real subregions based on excess vector analysis, the following result is derived. At a distance of 1.88 kpc, approximately 80% of the total content of the subregions have <1 solar mass, and the remaining ~20% of objects have 1–3 solar masses. Only two objects have >7 solar masses that are clearly distinguished from the rest of the objects in the CMDs. At a distance of 6.1 kpc, approximately 20% of the total content of the subregions have <1 solar mass, about 70% of objects have 1–3 solar masses, and the mass was estimated in the range 3–7 solar masses in only 7% of the cases. There are only five objects with mass >7 solar masses.

4.2.6. K luminosity function

Due to the uncertainty in the selected YSO ages (see Figure 21), it is impossible to derive an individual mass for each source and therefore the mass-luminosity relation cannot be constructed in order to get the IMF. Nevertheless, it is possible to construct the KLF to constrain the age of the embedded stellar population in each star-forming region independently (see also Section 4.1.5). Figure 22 shows the observed KLFs of YSOs detected in four subregions separately. In the case of the IRAS05162+3639 subregion, there are not enough YSOs to construct the KLF and so it is impossible to estimate the value of the α slope. The KLFs corresponding fitted slopes are provided in Table 11, which are lower than the typical values reported for young embedded clusters (α~0.4; e.g., [121]; [112]; [23]) and within the errors, the KLFs for all four subregions seem to match each other. For clusters up to 10 Myr old, the KLF slope gets steeper as the cluster gets older [3]; [120]. There are many studies on the KLFs of young clusters. [138] found similar values of α slopes around the W3 IRS 5 cluster (α = 0.24), and that it is consistent with an age of 0.3 Myr with a Miller-Scalo IMF. [157] estimated the KLF slope of NGC7538 to be α = 0.28±0.02 and with an age of ~1 Myr.

In addition, according to the calculation of [132], α values between 0.2 and 0.28 are consistent with an age range of 0.1-3 Myr. The α values of the observable subregions are close to this range of values; therefore, the age of all four subregions can be estimated between 0.1 and 3 Myr, which also closely reflects the location of stellar objects relative to the isochrones. The KLF of the IRAS05156+3643 star-forming region differs from the other subregions, i.e., a sharp decline does not occur in the end, which means that in this case the KLF reflects the real picture of the subregion, and in the remaining cases the decline is abrupt, reflecting the completeness limit of the survey. The KLF of IRAS05156+3643 star-forming region complicates the resolution of the α slope value, but in any case, it falls within the 0.15–0.28 range.

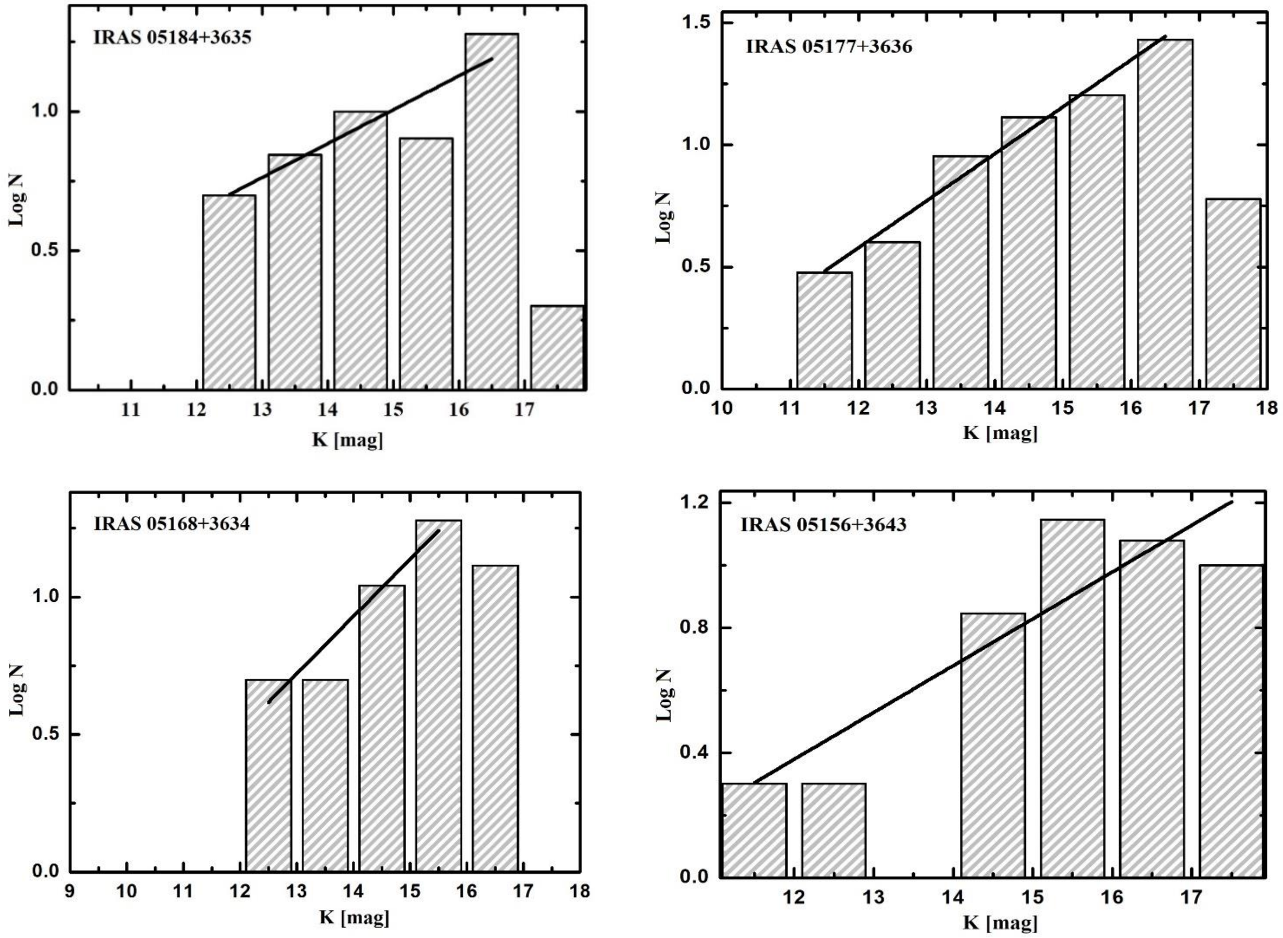

Figure 22. K luminosity functions are derived for the subregions as a histogram of the number of stars in logarithm vs. apparent K magnitude [156]. The bin size corresponds to 1 mag. The linear fits are represented by the straight lines and the slopes obtained are given in each figure.

4.2.7. SED analysis

The SEDs are constructed for 45 Class I and 75 Class II evolutionary stage YSOs. This procedure was done using J, H, and K (UKIDSS); 3.6 and 4.5 μm (*Spitzer* IRAC); 3.4, 4.6, 12, and 22 μm (WISE); 8.28, 12.13, 14.65, and 21.3 μm (MSX); 12 and 25 μm (IRAS); and 70 and 160 μm (*Herschel* PACS) photometric data. The SED fit was carried out using both distance estimations: 1.88 and 6.1 kpc. We used the ranges of the A_V and the distances of 1-40 mag, and 5.5-6.5 kpc and 1.6-2 kpc, respectively.

Figure 23 shows the constructed SEDs for those objects associated with IRAS sources in the near and far distances. Table 12 shows the weighted means and the standard deviations of parameters for IRAS and MSX sources with χ^2 - χ^2_{best} < 3N at near and far distances: 1.88 and 6.1 kpc. The numbering of the objects was done according to Table 9.

According to the results of SED fitting tool at distances of 1.88 and 6.1 kpc, objects associated with IRAS and MSX sources can be classified as middle-mass YSOs (Table 12), which confirms the results obtained in the c-c diagrams and CMDs. The results of the SED fitting tool, in general, confirm the age estimations obtained by the KLF slope for each subregion. The ratio between disk accretion and envelope infall rates of our objects correspond closely to those parameters given for Class I objects in [78].

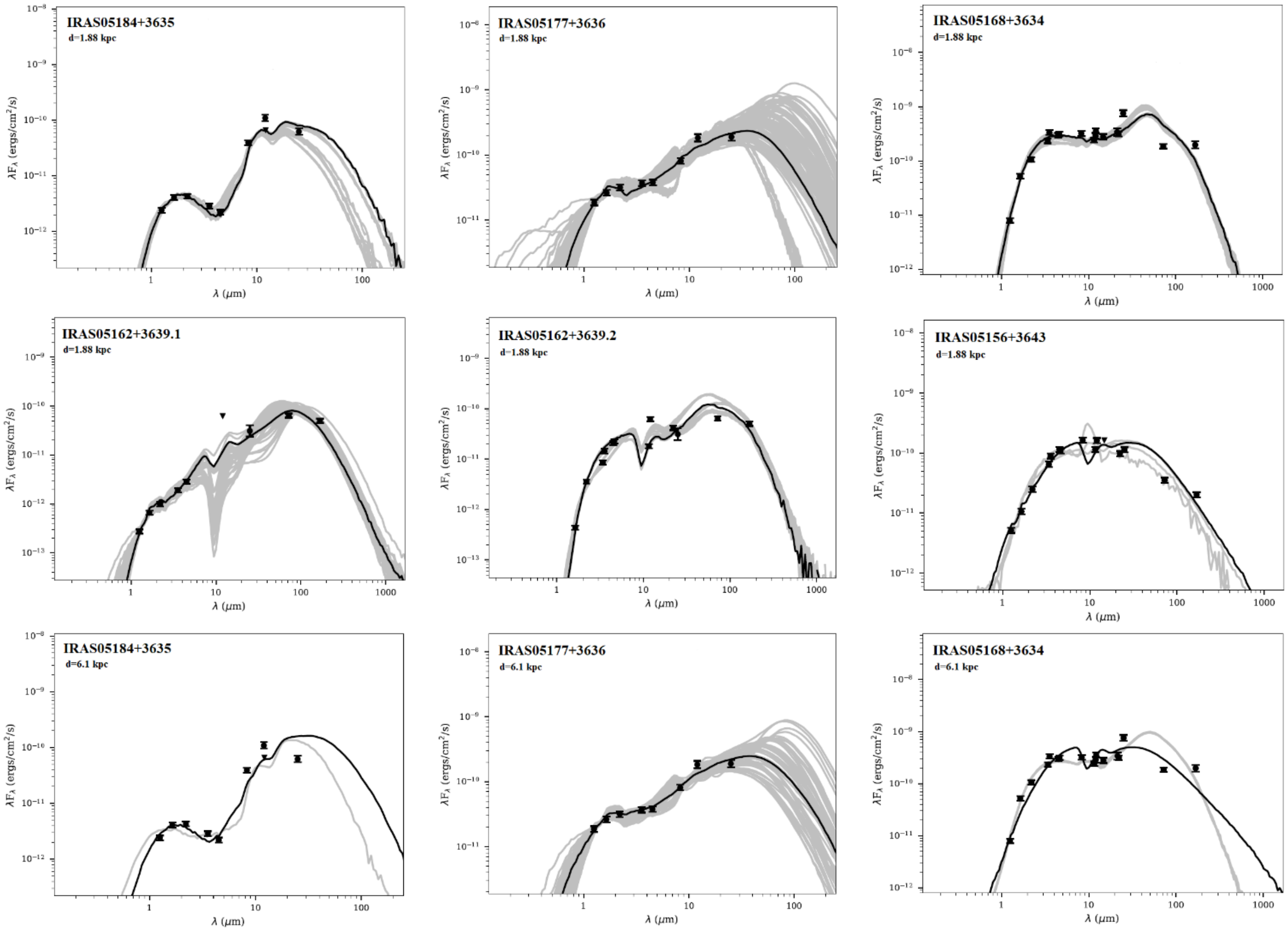

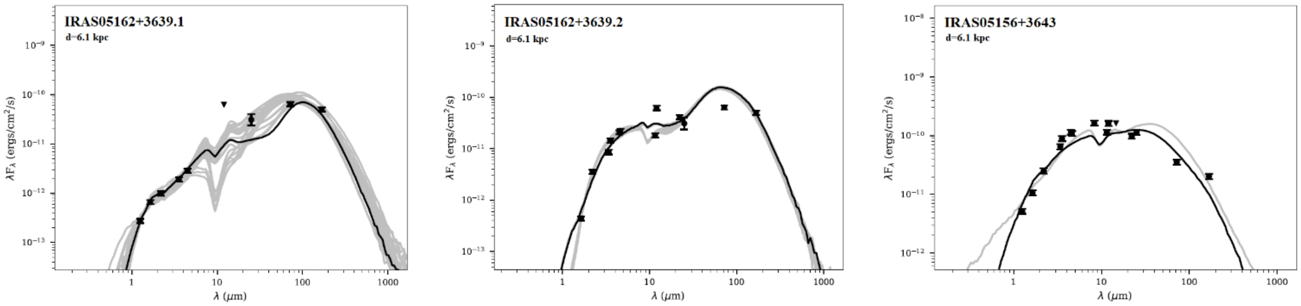

Figure 23. Infrared SEDs of IRAS sources are fitted to the models of [171] for distances of 1.88 and 6.1 kpc [156]. The filled circles represent the input fluxes, while triangles represent upper limits from the respective clumps. The black line shows the best fitting model and gray lines show the subsequent good fits.

Table 12. Parameters derived from [171] models SED fitting for two distances.

ID	A_v (mag)		Stellar age (Log)(yr)		Stellar mass ($M_\odot$)		Temperature (Log)(K)		MdotE (Log)($M_\odot$yr^{-1})		MdotD (Log)($M_\odot$yr^{-1})		L_{Total} (Log)($L_\odot$)	
	1.88	6.1	1.88	6.1	1.88	6.1	1.88	6.1	1.88	6.1	1.88	6.1	1.88	6.1
(1)	(2)	(3)	(4)	(5)	(6)	(7)	(8)	(9)	(10)	(11)	(12)	(13)	(14)	(15)
31	12.1	6.9	6.6	5.9	3.1	6.8	4.1	4.1	0.0	-5.3	-8.4	-7.6	1.9	3.0
85	9.3	3.8	5.9	5.8	3.7	5.2	3.8	4.0	-4.8	-4.6	-7.0	-6.7	2.0	2.6
96	0.6	0.2	3.2	3.5	0.3	2.3	3.5	3.6	-5.3	-4.6	-4.9	-4.6	1.2	2.3
97	4.4	3.0	5.8	4.1	2.6	5.5	3.8	3.6	-4.1	-3.5	-6.0	-5.0	2.4	2.6
101	8.6	2.0	6.3	6.0	4.2	5.5	3.9	4.2	-6.2	-7.3	-7.7	-7.1	2.2	2.9
128	19.5	8.1	5.9	6.0	4.5	5.5	3.9	4.2	-7.0	-8.3	-7.5	-6.4	2.4	2.8
177	6.0	8.9	5.0	5.1	1.9	6.6	3.6	3.9	-4.8	-4.5	-5.0	-4.3	2.0	3.1
182	23.5	11.4	6.5	5.5	4.9	5.5	4.2	4.1	0.0	-4.7	-8.6	-4.7	2.7	3.7
183	15.3	6.9	6.0	5.9	5.1	7.1	4.2	4.3	-7.4	-5.2	-8.0	-4.4	2.8	3.4
190	6.3	7.8	4.8	4.2	1.0	3.1	3.6	3.6	-3.9	-3.3	-6.3	-5.7	1.2	2.1
192	34.6	19.5	5.9	6.0	4.5	5.4	3.9	4.2	-5.6	-7.2	-7.5	-6.7	2.2	2.8
234	2.1	1.4	6.2	3.8	3.4	2.9	4.1	3.6	-6.0	-4.7	-4.8	-4.6	3.2	2.3
239	22.8	14	5.6	6.0	4.4	4.7	3.7	4.1	-5.1	-5.6	-8.9	-6.1	2.0	2.6

Notes. (1) ID number of sources taken from Table 9, (2)–(15) weighted means and standard deviations of parameters obtained by fitting tool for all models with best χ^2- χ^2_{best} < 3N at two distances: 1.88 and 6.1 kpc. The full table is available in VizieR On-line Data Catalog: J/A+A/622/A38.

4.2.8. Substructures of the molecular cloud

In this section, we give an overview of the substructures of four clearly visible subregions found in the molecular cloud surrounding IRAS05168+3634. Figure 24 shows the LD distribution of selected YSOs (N = 240) within the obtained radii (see Section 4.2.4) on the K-band images. The value of LD for the first isodense exceeds the density of a field with a value of 3σ. We investigate separately the substructures of subregions, and the distributions of Class I and Class II evolutionary stage objects in the subregions. Each of the subregions is an embedded cluster.

The LD distribution of all the YSOs in the subregions shows elongated structures. The elongated structure was also evident in some of the earlier studies of clusters [40]; [94]. The elongation appears to be a result of the primordial structure in the cloud, and the elongation is aligned with the filamentary structure seen in the parent molecular cloud [6] and they are often composed of subregions [115]; [45]; [136]; [5]. All subregions have an expressed elongation and each consists of subgroups.

Figure 24 **a)** shows the LD distribution of YSOs in the IRAS05184+3635 star-forming region. The IRAS05184+3635 star-forming region has a bimodal structure and the main concentration of objects is located v40 arcsec northwest (NW) of IRAS05184+3635, which is associated with a MSX object (G170.8276+00.0098). A young star of intermediate-mass (3.1±0.6$M_{\odot}$) and evolutionary age of ~10^6 years (ID 31 in Table 9) is associated with the IRAS source (or MSXG170.8276+00). There are two more MSX sources here: G170.8321+00.0045 and G170.8319+00.0086. According to Table 9, in the vicinity of these sources, in addition to the ID 31 stellar object, within a radius of 11″–14″, only one stellar object of the II evolutionary class has been identified (ID 11 in Table 9), which mass and evolutionary age have not been determined.

The LD distribution of YSOs in the IRAS05177+3636 star-forming region is shown in Figure 24 **b)**. The IRAS05177+3636 star-forming region also has a bimodal structure and consists of two main subgroups, each with an elongation. There are three MSX sources in the IRAS05177+3636 star-forming region, one of them (G170.7268-00.1012) is associated with IRAS05177+3636. An intermediate-mass YSO with 2.6±1.3$M_{\odot}$ mass and an evolutionary age of less than 10^6 years (ID 97 in Table 9) is associated with the IRAS source. The second MSX source (G170.719-00.1118) is located in the northeast (NE) subgroup with IRAS05177+3636; it is associated to a YSO with intermediate-mass (4.5±0.7$M_{\odot}$) and an evolutionary age less than 10^6 years (ID 128 in Table 9). The third (G170.7247-00.1388) is in the second subgroup ~2.2 arcmin to the southwest (SW) of IRAS05177+3636. It should be noted, however, that IRAS05177+3636 and all the MSX sources are on the edges of two subgroups. There are two BGPSv2 objects in the immediate vicinity of the IRAS source: G170.724-00.105 and G170.733-00.103. Besides the IRAS object, two more YSOs are located closest to the BGPSv2 objects: the intermediate-mass star (3.7±0.7$M_{\odot}$) with less than 10^6 years evolutionary age (ID 85 in Table 9) and the low-mass star

($0.3 \pm 0.2 M_{\odot}$), apparently at a very early evolutionary stage (ID 96 in Table 9). It has an evolutionary age of less than 10^5 years.

The LD distribution in IRAS05168+3634 star-forming region demonstrates unique elongation (Figure 24 **c)**). There are no clearly visible subgroups, but three poles associated with MSX sources can be seen. One of the subgroups is located around IRAS05168+3634. The intermediate-mass YSO ($5.1 \pm 0.3 M_{\odot}$) with an evolutionary age of about 10^6 years is associated with the IRAS (ID 183 in Table 9), which is the dominant object in the given subgroup. IRAS05168+3634 is identified with MSX G170.6575-00.2685. Another subgroup is found to the NE of IRAS05168+3634. [143] detected 6 cm radio emission 102 arcsec away from IRAS05168+3634 whose coordinates are α_{2000}=05:20:23.53, δ_{2000}=+36:38:17.58. As in the previous region, the BGPSv2 object is located at the column density and dust temperature maximum. It is a dense core G170.661-00.249. The location of the second MSX G170.6589-00.2334 object (associated with intermediate-mass YSO (ID 177, $1.9 \pm 0.7 M_{\odot}$) with an evolutionary age of ~10^5 years) is ~2.118 arcmin NE of the IRAS05168+3634 position. The third subgroup in the IRAS05168+3634 star-forming region is located to the southeast (SE) of the IRAS05168+3634.

The MSX G170.6758-00.2691 object in the IRAS05168+3634 star-forming region is ~1.135 arcmin SE of the IRAS05168+3634 position and is located in the subgroup. It is also associated with an intermediate-mass YSO ($4.9 \pm 0.5 M_{\odot}$) with an evolutionary age of ~10^6 years (ID 182 in Table 9). In the case of the IRAS05168+3634 subregion, the IRAS and MSX sources are also located in the edges of subgroups.

The IRAS05156+3643 star-forming region has the most complex structure (Figure 24 **d)**). It consists of three subgroups that show elongated structures, and one of them is even composed of two smaller subgroups. IRAS05156+3643 is out of these three subgroups. This IRAS object is associated with MSX G170.3964-00.3827 (ID 234 in Table 9). It is the star with ~$3.8 \pm 3.6 M_{\odot}$ mass and evolutionary age of ~10^6 years. According to coordinates and 2MASS JHK photometric data, this stellar object corresponds to the high proper-motion star LSPM 1267-0099892 from the LSPM-NORTH catalog [126]. Taking into account the high accuracy of parallax measurements and proper motion in *Gaia* EDR3, we tried to identify the stellar object associated with IRAS05156+3643. According to the coordinates, it is the object with ID 187051701258568960 in *Gaia* EDR3. Unfortunately, the parallax measurement accuracy is not high enough and is $\varpi / \sigma_{\varpi} = 1.7$. According to the transformations of [20], the low distance estimation is ~2.2

kpc, what is close to the parallax estimation for the star-forming region. Using the Galactocentric transformations of [99], we computed peculiar velocity of this star for 2.2 kpc distance: V_{pec} = 57 km/s. The BGPS object (BGPSv2 G170.384-00.407) is localized precisely in the region of the N(H_2) maximum. A YSO with ID 239, 4.4±0.3$M_\odot$. mass and evolutionary age of ~10^6 years is associated with it.

The LD distribution on the IRAS05162+3639 star-forming region cannot provide any information because there are only five objects. It should be noted that all of these five objects were classified as Class I evolutionary stage objects, and that two of them were identified with IRAS05162+3639. It is the object with ID 190 (1.0±0.4$M_\odot$ mass and evolutionary age of ~10^5 years), as well as the object with ID 191 (0.6±0.1$M_\odot$ mass and evolutionary age of ~10^6 years). This binary needs a separate study and it should be noted that the results obtained from the SED are likely to be incorrect.

If the observed morphologies of embedded clusters result from the filamentary and clumpy nature of the parental molecular clouds, then the younger Class 0/I objects, which have the least time to move away from their star formation sites, should show more pronounced structures than the older, PMS Class II and Class III stellar objects. However, there is no difference between the distributions of Class I and II objects in the field of the subregions, but there is a big difference between the distributions of Class I and II objects in the molecular cloud as a whole (Figure 19).

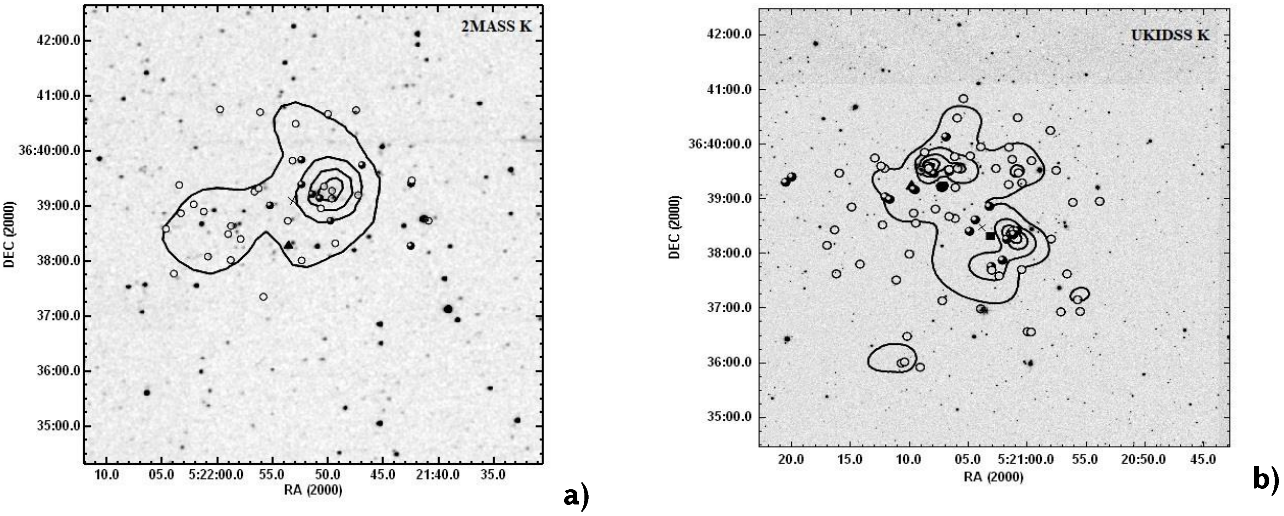

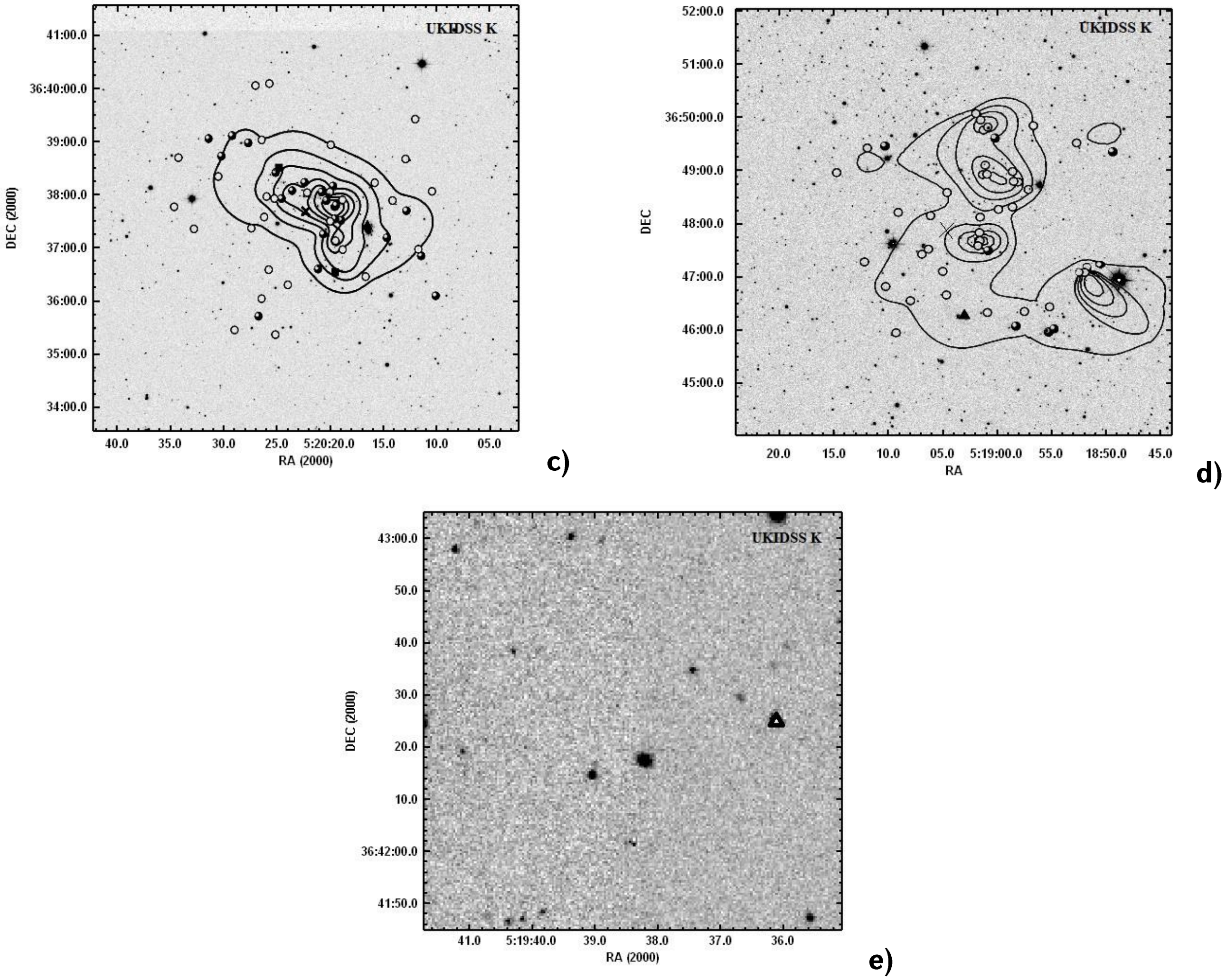

Figure 24. LD distribution of the YSOs and spatial distribution of Class I and Class II objects superposed on the K-band images [156]. **a**) - IRAS05184+3635, **b**) - IRAS05177+3636, **c**) - IRAS05168+3634, **d**) - IRAS05156+3643, **e**) - IRAS05162+3639. Filled and open circles represent the Class I and Class II objects, respectively. The triangles and squares show the location of IRAS and MSX sources, respectively, which are also classified as Class I objects. The geometric center of each subregion is indicated by a cross.

4.2.9. Distance of the star-forming region

As mentioned in the Introduction of this Chapter, the results for the distance of IRAS05168+3634 star-forming region are quite different. In order to clarify the distance, we attempt to identify the list of YSOs in the *Gaia* EDR3 database. In total, we were able to identify 65 objects, but only for 11 of them the parallax measurement accuracy is high enough ($\varpi/\sigma_{\varpi} > 5$). The data of these 11 objects are shown in Table 13. Such a small number of objects identified with sufficient accuracy is quite expected. The embedded in a dense ISM cluster contains YSOs, which are surrounded by optically thick circumstellar disks and envelopes. In combination, this makes cluster members difficult to access optically. The number of identified objects is not sufficient for a detailed statistical study, but nevertheless allows us to draw some conclusions about the distance of the star-forming region as a whole. Distances of 6 out of 11 stars in Table 13 are close to the parallax estimation with VERA for IRAS05168+3634 (~1.9 kpc, [174]). Their positions and ID numbers in Table 13 are shown on Figure 25. We can see that these stellar objects are scattered in almost all sub-regions, with the exception of only IRAS05162+3639. Moreover, one of them, the 97th, is associated with IRAS05177+3636. We would like to remind that direct measurements of distances were made only for IRAS05168+3634. The result obtained from *Gaia* EDR3 data can be considered as one more argument in favor of the fact that all sub-regions are embedded in the single molecular cloud and belong to the same star-forming region, which is located at ~1.9 kpc distance.

Table 13. *Gaia* EDR3 data

N	***Gaia* EDR3**	**ϖ (mas)**	**σ_{ϖ} (mas)**	**PM (mas/yr)**	**LD (pc)**	**HD (pc)**	**V_{pec} (km/sec)**
(1)	(2)	(3)	(4)	(5)	(6)	(7)	(8)
1	184011624623256704	0.520	0.025	3.054	1780	1963	26±1.5
14	184013166513879808	7.795	1.234	18.875	116	162	16±1.0
60	184053612223579136	0.558	0.052	2.846	1597	1936	20±2.0
82	184059620881914880	2.443	0.39	1.875	376	516	10±0.5
91	184053436128920448	1.683	0.261	2.755	532	758	11±0.3
97	184059350299876608	0.541	0.087	2.525	1608	2290	17±4.0
101	184053401769173888	0.965	0.13	2.864	897	1139	12±0.5
132	184055536368961792	1.279	0.019	11.533	744	769	36±1.0
143	184054746094985984	0.505	0.053	2.819	1749	2170	22±3.0
219	187052182295036672	0.648	0.092	2.854	1319	1820	17±3.0
227	187051877354793984	0.583	0.109	3.428	1534	2662	22–40
234	187051701258568960	0.401	0.236	3.428	2224	4780	51–110

(1) – ID numbers are taken from Table 9, (2) – a source designation in *Gaia* EDR3, (3) - (5) – parallax, parallax error and proper motion obtained from *Gaia* EDR3 database, (6), (7) – low and high distances obtained through [20], (8) – peculiar velocity obtained by using the Galacto-centric transformations of [99].

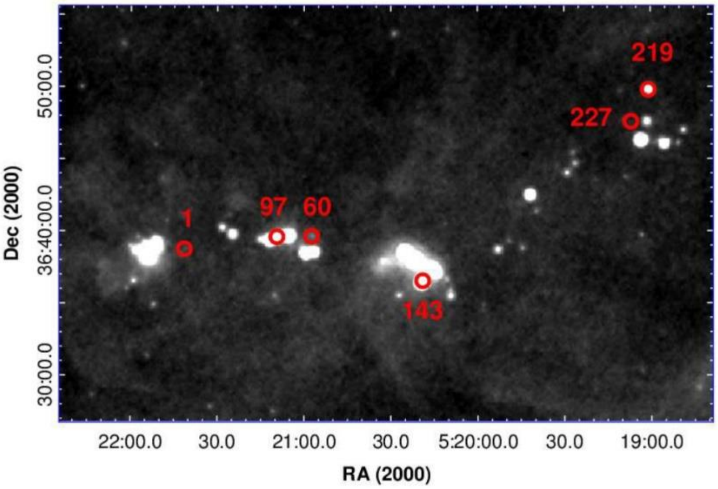

Figure 25. W4 image of the IRAS05168+3634 star-forming region [153]. The positions (red circles) and ID numbers of 6 stars, which, according to the *Gaia* EDR3 data, are located at a distance of ~2 kpc (see Table 13) are marked.

4.2.10. ISM and stellar content

Table 14 shows the main parameters of ISM in the IRAS sub-regions, including N(H_2), T_d, ISM masses, and the stellar content. Taking into account the number of identified stellar objects, the average value of their masses, as well as the ISM mass in the surrounding cloud, we find that SFE ($M_{stars}/(M_{stars}+M_{ISM})$) in all sub-regions is less than 0.1%. Even if we take into account that not all stellar objects were detected, the SFE value still indicates an active star formation process in the entire region.

Table 14. Parameters of the stellar content and ISM in IRAS sub-regions

IRAS / Param.	05156+3643	05162+3639	05168+3634	05177+3636	05184+3635
n_{star} (arcmin^{-2})	1.9	25.5	2.0	2.1	2.6
N(H_2)(x10^{23} cm^{-2})	1.1-1.6	0.9-1.0	1.1-3.8	1.1-2.3	1.1-1.5
T_d (K)	11-12	11-12	11-24	12-13	12-15
*ISM Mass ($M_{\odot}$)	(1.7±0.05)x10^4	-	(2.1±1.6)x10^5	(9.2±0.3)x10^4	(4.0±0.1)x10^4

*ISM masses are determined in the area limited by the isodence corresponding to 1.1x10^{23} cm^{-2} value, which exceeds the average hydrogen column density in surrounding medium by 2σ. The error bars are due to the average value of the uncertainty of parameters (χ^2) in the sub-regions and the uncertainty in estimating the distance to the star-forming region.

The BGPSv2 objects identified in the three sub-regions (IRAS 05156+3643, 05168+3634, and 05177+3636) are located at maximum density and temperature. On the one hand, this is an expected fact, since these 1.1 mm sources are good indicators of dust emission and, therefore, star-forming clumps. On the other hand, this confirms the reliability of our results. However, another key, brightest stellar objects, including those associated with the IRAS and MSX sources, localized as regions of N(H_2) and T_d maxima, as well as significantly displaced from them. We also want to note that in most cases, the evolutionary age of associated with the BGPSv2, IRAS, and MSX sources intermediate-mass stellar objects is about 10^6 years.

The dust temperature, excluding IRAS05168+3634 sub-region, is only a few degrees higher than that in the surrounding molecular cloud. According to our results, no high-mass stars were found in the cluster, which is probably the reason for the relatively low temperature in this region. A small increase in T_d to 15 K in the IRAS05184+3635 sub-region, most likely, can be explained by the highest stellar density. Since only 5 stellar objects were detected in IRAS05162+3639 sub-region, we do not take it into account in the comparison. As mentioned above, in IRAS05168+3634 sub-region, it was identified a high-mass star-forming region in pre-UC HII phase [142], which could be the reason why the dust temperature in this region is significantly, almost 10 K, higher.

4.2.11. Origin of the star-forming region

If we classify the evolutionary stage of sub-regions in relation to the percentage of Class I and Class II YSOs, then IRAS05168+3634 sub-region can be considered the “youngest”. The next “youngest” sub-region by the percentage of Class I stellar objects is IRAS05177+3636. At the same time, IRAS 05168+3634 and 05177+3636 sub-regions have the highest N(H_2) and ISM mass. The sub-regions around IRAS 05184+3635 and 05156+3643 in the outer part of the molecular cloud, according to the same criterion, are the “oldest”. It should be noted once again that since there is no real concentration around IRAS05162+3639, we do not consider this region. On the other hand, if we consider the position of stellar objects on the CMD, it is clearly seen that stars from all sub-regions have a wide spread relative to the colour index $(J-K)_{abs}$ and, therefore, isochrones. For clarity, we also built the evolutionary age histograms of sub-regions’ members, defined using the SED fitting tool (see Section 0). Unfortunately, this information is available only for 50% of all identified members of the clusters. A histogram for the 1.9 kpc distance is shown in Figure 26. The histogram also shows that the evolutionary age of stars in all sub-regions has very wide spread. The overwhelming majority of them are located in the range from 10^5 to 10^7 years.

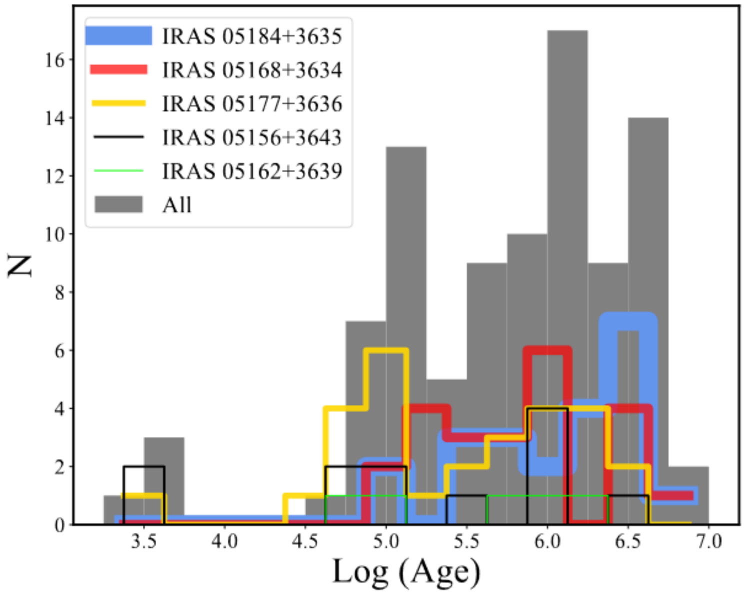

Figure 26. Histogram of the evolutionary ages determined by the SED fitting tool for members of the IRAS sub-regions [153]. The bin size corresponds to Log(Age) = 0.25.

Since, the age spread of the considered star-forming region is large, it can be concluded that the stellar population is formed as a result of independent and sequential condensations in the parent molecular cloud. Moreover, in those sub-regions where the mass of the initial, parent molecular cloud is greater, this process is more active and presumably has a longer duration. As a result, at the moment, the percentage of younger stars could be more.

4.2.12. Conclusions

Our investigations show that the IRAS05168+3634 star-forming region, considered in previous studies, has a more complicated structure in the FIR wavelengths. Studies in FIR wavelengths suggest that the IRAS05168+3634 star-forming region is located in a quite large molecular cloud within a region of approximately 24 arcmin radius (the center of the molecular cloud is conditionally selected as IRAS 05168+3634), which in turn consists of four additional star-forming regions. From the statistical analysis it follows that all IRAS star-forming regions are at the same distance: 6.1 kpc [142] or 1.88 kpc [174], i.e., there is a small probability that these star-forming regions may be the result of superposition. In addition, these regions repeat the shape of the molecular cloud. Also, the distances of IRAS 05184+3635 and 05177+3636 assessed based on the ^{13}CO velocities were evaluated at the same 1.4 kpc value, which coincides with the distance of IRAS05168+3634 based on trigonometric parallax. The intermediate-mass YSO associated with IRAS05156+3643 source is a runaway star with Vpec equal to ~50 km/s with the low distance estimation of ~2.2 kpc. Moreover, on the *Gaia* EDR3 database, it can be assumed that all sub-regions are embedded in the single molecular cloud and belong to the same star-forming region, which is located at ~1.9 kpc distance. However, we did all our calculations for both distances. It should be noted that even with such a different estimate of the distance, the main conclusions regarding the stellar population of the star-forming region do not change significantly.

We analyzed the stellar content of the molecular cloud and separately for each star-forming region associated with IRAS sources using the J, H, K UKIDSS-DR6; [3.6], [4.5] μm Spitzer GLIMPSE 360; and [3.4], [4.6], [12], [22] μm ALLWISE survey images and photometric data to construct c-c diagrams and CMDs, which are useful tools for identifying YSO candidates. Using NIR and MIR photometric data, we obtain the census of the young stellar populations and their characteristics within a 24 arcmin radius region surrounding the molecular cloud, which includes 1224 candidate YSOs, 240 of which are concentrated around five IRAS sources. We classified 71 YSOs as evolutionary stage Class I objects and 132–169 YSOs (depending on the distance) as evolutionary stage Class II objects within the radii of sub-regions. One can see, depending on the c-c diagrams and CMDs, the number of Class II evolutionary stage objects is changing, but the number of Class I evolutionary stage objects is not changing, and the conclusion is that the selection of Class I objects is highly accurate. Notably, unlike the Class II objects, the Class I objects are located mainly in the filaments of the molecular cloud, i.e., the distribution of Class I objects reflects the initial state of the parent molecular cloud. The estimated distances and the A_v of each sub-region were taken into account in the corrections of J and K magnitudes for the CMDs, which generates a great difference in the number of Class II objects. From the CMD analysis using evolutionary models of various ages by [183], there is a large distribution of ages, but the age of most of them is on the order of 10^5 years. A mass completeness limit has been quoted for two distances. Selected YSOs located in the IRAS 05184+3635, 05168+3634, and 05156+3643 star-forming regions are explicitly targeted at a specific mass range for two distances; for objects in the IRAS 05177+3636 star-forming region, there is no similar dependency. The members of the IRAS 05184+3635 and 05156+3643 sub-regions are targeted to a lower mass range, i.e., the members of IRAS05184+3635 are distributed in the ranges of 0.3–1.5 and 0.8–5 $M_{\odot}$ and the members of IRAS05156+3643 in the ranges 0.2–1.6 and 0.6–3 $M_{\odot}$ at distances of 1.88 and 6.1 kpc, respectively. Conversely, the members of the IRAS05168+3634 sub-region are distributed in a higher mass range, i.e., they are at 0.5–2.5 and 0:9 - > 7 $M_{\odot}$ at distances of 1.88 and 6.1 kpc, respectively.

We have also calculated the slope of the KLFs for four sub-regions, namely IRAS 05184+3635, 05177+3636, 05168+3634, and 05156+3643. The KLF of these subregions shows unusually low values for the α slope: 0.12–0.21. According to the values of the slopes of the KLFs, the age of all four sub-regions can be estimated between 0.1 and 3 Myr. There are not enough YSOs within the radius of the IRAS05162+3639 sub-region, so the KLFs for this sub-region were not constructed.

The SEDs were constructed for 45 and 75 YSOs with evolutionary stages Class I and Class II, respectively. This procedure was done using wavelengths ranging from 1.1 to 160 μm. According to the results of the SED fitting tool, IRAS 05184+3635, 05177+3636, and 05162+3639 can be classified as Class I for both distances. The sources IRAS 05168+3634 and 05156+3643 can be classified as flat-spectrum objects for both distances. At the distance of 6.1 kpc, all IRAS sources have 6–7 $M_{\odot}$, except for IRAS05156+3643, and one of the two objects associated with the IRAS05162+3639 binary object (both have 3 $M_{\odot}$ mass). At the distance of 1.88 kpc, estimated masses vary considerably only in the case of IRAS 05184+3635 and 05177+3636, and the mass estimation is the highest for IRAS05168+3634: 5 $M_{\odot}$. The results of the SED fitting tool, in general, are well correlated with the age estimations obtained by the KLF slope for each sub-region. According to the results of the SED fitting tool, at 1.88 and 6.1 kpc distances, IRAS and MSX sources can be classified as middle-mass YSOs, which confirms the results obtained in the c-c diagrams and CMDs.

All star-forming regions have complicated structures. They contained the subgroups, which are mainly associated with IRAS and MSX sources. The observed young sub-regions and parental molecular cloud morphologies are similar and elongated. This is particularly well expressed when only the youngest Class I/0 sources are considered. Perhaps the similarities in morphologies result from the distribution of fragmentation sites in the parent cloud. The Class I sources are often distributed along filamentary structures, while the Class II sources are more widely distributed. A similar distribution of Class II evolutionary stage objects can be explained by the fact that these objects have had enough time to leave their own birthplaces. In the case of Class I evolutionary stage objects, that time is small, and this is why they are located on the filaments of the parent molecular cloud, thus they clearly reflect the initial state of the parent cloud.

The determination of ISM physical parameters ($N(H_2)$ hydrogen column density and T_d dust temperature), as well as the comparative analysis of the properties of the ISM and YSOs revealed the following:

- The gas-dust matter has an inhomogeneous structure, forming relativity dense condensations around the majority of IRAS sources, which are interconnected by a filament structure.
- In general, in sub-regions T_d varies from 11 to 24 K, and $N(H_2)$ - from 1.0 to 4.0×10^{23} cm^{-2}. The masses of the ISM vary from 1.7×10^4 to 2.1×10^5 $M_\odot$.
- The SFE in the sub-regions is less than 0.1%.
- The identified BGPSv2 objects are located at the column density maximum. It should be noted that observations in the optically thin, minimally affected by temperature millimeter continuum provide one of the best methods to identify star-forming clumps [75]. It is quite expected that the BGPS object is localized precisely in the region of the $N(H_2)$ maximum.
- The sub-regions with the highest hydrogen column density and ISM mass have the largest percentage of YSOs with Class I evolutionary stage.

Based on the fact that the evolutionary ages of stars in all sub-regions have a very wide spread (from 10^5 to 10^7 years), we assumed that in the considered region the stellar population is formed as a result of independent condensations in the parent molecular cloud, and, therefore, the star formation process is sequential. In sub-regions where the mass of the initial, parent molecular cloud is greater, this process is most likely more active.

4.3. IRAS19110+1045 AND IRAS19111+1048

4.3.1. Introduction

The star-forming regions associated with IRAS 19110+1045 and 19111+1048 sources, referred to as G45.07+0.13 and G45.12+0.13 UCHII regions, respectively [199], are part of the Galactic Ring Survey Molecular Cloud (GRSMC) 45.46+0.05 large star formation complex [184], where several other UCHII regions are found. This complex is thus an ideal laboratory to investigate the early stages of massive star formations and their influence on natal environments.

From the images obtained at 2 and 6 cm radio wavelengths, [199] determined a spherical morphology of the ionised gas in the G45.07+0.13 and a cometary shape in G45.12+0.13. On 1.3 mm continual images, G45.12+0.13 has an elliptical shape, elongated from NE to SW [91]. At MIR wavelengths, both objects show extended emissions and each includes at least 2 UCHII regions [54], [55]. Given their proximity in the plane of the sky and similar LSR velocities, [98] suggested that G45.12+0.13 and G45.07+0.13 are at the same distance (8.3 kpc). [184] determined a kinematic distance of 6 kpc for the GRSMC 45.46+0.05 complex containing the two UCHII regions. [71] and [84] obtained near and far kinematic distances for both G45.07+0.13 and G45.12+0.13 of ~4.0 and ~8.0 kpc, respectively. The estimated far distance is consistent with the previous estimate by [98] and a more recent one based on the trigonometric parallax method (7.75±0.45 kpc, [202]). Therefore, we adopt a distance of 7.8 kpc in our study.

Multi-wavelength studies suggest that both regions are sites of active massive star formation, where IRAS 19111+1048 (G45.12+0.13) is in a more advanced stage [98]; [197]. [98] were the first to detect outflows from these sources. Their CO (J = 6 - 5) map shows bipolar outflows with an origin well centred on the radio position of both UCHII regions. The continuum-subtracted molecular hydrogen image in [160] shows a pair of faint H_2 emission knots in G45.07+0.13. Both regions contain type I OH masers [14], however, only G45.07+0.13 produces H_2O [97] and methanol maser emissions [90]; [33]. The probe of massive star-forming clumps, SO $J_k = 1_0 - 0_1$ (i.e. 30 GHz) emission, has also been detected in both regions [133].

The NIR data, as well as high-resolution radio measurements, enabled [197] and [169] to conclude that the IRAS19111+1048 region contains numerous ZAMS stars energising a compact and evolved HII region. [127] reached the same conclusion based on multi-wavelength images observed with SOFIA-FORCAST at wavelengths from ~10 to 40 μm. Based on integrated radio emission, these sources' spectral types are O6 - B0 and the power law index of the IMF is 5.3 ± 0.5 for the mass range $14<m/M_{\odot}<33$ [197]. [16] revealed a compact group of PMS objects (~50 members) in the vicinity of IRAS19110+1045.

4.3.2. Dust emission

In Figure 27, we present a colour-composite image (left panel) with three Hi-GAL bands (PACS 160 μm and SPIRE 350 and 500 μm) covering the molecular cloud. The G45.12+0.13 and G45.07+0.13 UCHII regions stand out sharply in terms of brightness. The black circles coincide with the positions and dimensions of radio continuum radiation [199]. These sources align well with the brightest part of the 850 μm emission (right panel). Figure 27 shows that both UCHII regions are embedded in a molecular cloud, with clear clump-like and filamentary structures. The images also indicate that the UCHII regions are connected by a relatively colder bridge and are thus very likely a physically bound system.

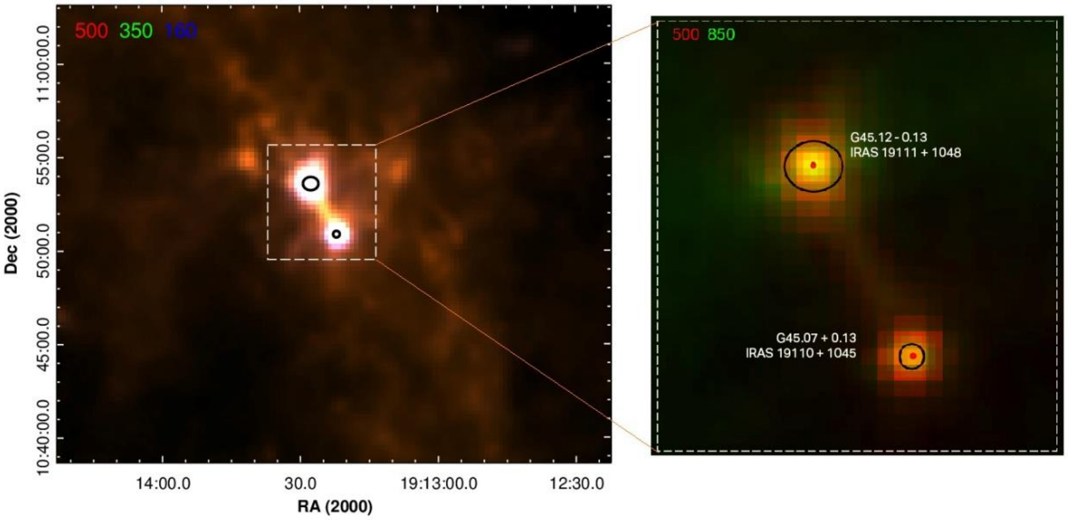

Figure 27. Colour-composite images of G45.12+0.13 and G45.07+0.13 UCHII regions. *Left panel: Herschel* 160 μm (blue), 350 μm (green), and 500 μm (red); *right panel:* zoomed area (white dotted square) at SCUBA 850 μm (green) and *Herschel* 500 μm (red). The positions and dimensions of the radio sources, obtained at 2- and 6-cm wavelengths in [199] are marked by black circles. A red dot represents the position of an IRAS source.

Figure 28 shows a colour-composite image of *Spitzer* IRAC 3.6 and 8.0 μm, and SPIRE 500 μm emission bands, illustrating that the UCHII regions are also very bright in the MIR wavelength range. This indicates a relatively high ISM temperature in the vicinity of the UCHIIs and, therefore, the presence of a significant number of hot stars [197]; [169]. Furthermore, the MIR image is saturated in the centre of both regions, which is the case for several UCHIIs [46]; [54]. In Figure 28, the arrow shows a small clumpy structure coinciding with the MSX G045.1663+00.0910 object. Three objects from the Bolocam Galactic Plane Survey (BGPS) are located within the external contour of *Herschel* 500 μm contour; of these objects 6535 and 6536 in the Bolocat V2.1 catalogue [64] are associated with IRAS 19110+1045 and 19111+1048, respectively. The third object (6737) is associated with MSX G045.1663+00.0910. In the distance estimates for these three BGPS objects are almost identical (7.5 - 7.9 kpc, [64]), consistent with the findings of [202] and confirming that they belong to the same star formation region. We also would like to highlight the filamentary structure directed NE towards the most extended part of the GRSMC 45.46+0.05 molecular cloud, to which UCHIIs G45.12+0.13 and G45.07+0.13 belong [184].

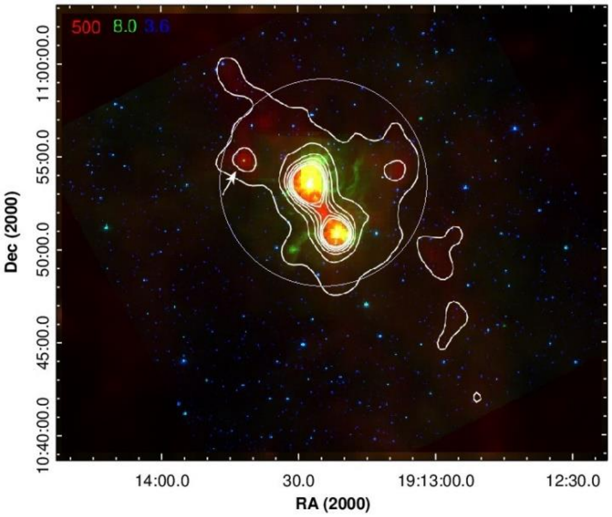

Figure 28. Colour-composite image of the G45.12+0.13 and G45.07+0.13 UCHII regions: *Spitzer* IRAC 3.6 μm (blue), 8.0 μm (green) and *Herschel* 500 μm (red). The latter is also shown with a white isophotes. The external isophot corresponds to a surface brightness of 0.55 Jy/pix, which exceeds the background σ = 0.18 Jy/pix by threefold. The difference between the isophotes level is 0.25 Jy/pix. The white arrow shows a small clumpy structure around the MSX G045.1663+00.0910 object. The circle outlines an area with a radius of 6 arcmin, which almost completely covers the region of study.

The N(H_2) and T_d maps of the wider region surrounding the G45.12+0.13 and G45.07+0.13 UCHII objects are shown in Figure 29. Both UCHII regions are distinct from the molecular cloud due to their high dust temperature and column density with an almost spherically symmetric distribution. This is fully consistent with the basic concept of UCHII regions about the presence of a hot, high mass stellar source and stellar wind, which leads to the blowing out of matter [187]. In general, within both regions, T_d varies from about 17 to 40 K and N(H_2) varies from about $3.0x10^{23}$ to $5.5x10^{23}$ cm^{-2}, consistent with other UCHIIs [48]. As can be seen in Figure 29, the temperature distribution in both UCHII regions has a pronounced spherical symmetry.

G45.07+0.13. In this region, the IRAS source is somewhat offset from the density maximum, which is ~$5.0x10^{23}$ cm^{-2}. Near IRAS19110+1045, the column density is ~$3.5x10^{23}$ cm^{-2}. This value agrees well with the data obtained in [48] (i.e. $3.0x10^{23}$ cm^{-2}) and is almost an order of magnitude smaller than the value of [91] ($2.7x10^{24}$ cm^{-2}). In both studies, the results were obtained based on millimetre observations. The IRAS source is located close to the dust temperature maximum (T_d = 42 K). This value is consistent with the data obtained in the submillimetre range (T = 42.5 K, [169]), and, within error, with the data presented in [91] (T = 82^{+25}_{-39} K). As shown in Figure 29, the dust temperature drops significantly from the centre to the periphery, reaching a value of about 18–20 K. Beyond around a 5-pixel (~1.2′ or ~2.6 pc) distance from the IRAS source, T_d remains constant. This may correspond to the extent of the region of influence of the ionising source(s). The size of this region correlates with the size of the extended emission (1′x1′, [54]), and this region's mass is ~$1.7x10^5$ $M_\odot$.

G45.12+0.13. In this region, the position of IRAS19111+1048 coincides with the maxima of both the column density ($5.5x10^{23}$ cm^{-2}) and temperature (35 K). Our N(H_2) value exceeds that presented in [48] by more than an order of magnitude, however, it is comparable with the value obtained through analysis of the multi-transition ^{13}CO emission [49]. The T_d value is in good agreement with the data presented in [169] (T = 39 K). The isotherms are slightly elongated towards the NW (Figure 29), which may relate to the presence of two UCHIIs (G45.12+0.13 and G45.13+0.14) that are separated from each other in a NW direction [54]. Similar to G45.07+0.13, the dust temperature in G45.12+0.13 drops significantly further from the centre, reaching a value of around 18–20 K in its periphery. The T_d decline levels out at around 7 pixels (~1.6′ or ~3.7 pc) from the IRAS source. As above, the size of this region correlates with the size of the extended emission (1.5′x1.5′, [54]). The larger radius of the ionised region indicates that the physical extent of ionized gas around IRAS19111+1048 is larger than that of its neighbour IRAS19110+1045 [197]. The mass of this region is ~3.4x10^5 $M_\odot$.

In both regions, the extent of the ionised area significantly exceeds the size of the UCHII radio cores. Previous studies have shown that many UCHII regions are surrounded by extended emission (on an arc-minute scale) produced by low-density ionised halos ([46]; [54]; [55], and ref. therein). The energy flux from these halos is quite large relative to that of the small UCHII cores, implying ionisation by a cluster of hot stars rather than a single star [46].

In Figure 29, a region with relatively high density (N(H_2)≈4.3x10^{23} cm^{-2}) and low temperature (T_d≈19 K) is positioned between the two UCHII regions. This region coincides with the bridge between the UCHII regions, which is also distinguishable in the *Herschel* and *Spitzer* images (Figure 27 and Figure 28), as well as on the H30α maps [48], suggesting that these UCHII regions are physically connected.

The distribution of the hydrogen column density in the surrounding molecular cloud has a complex, clumpy structure — in general, outwards from the UCHII regions, N(H_2) varies from about 3.0 to 0.5x10^{23} cm^{-2} and T_d varies from about 16 to 12 K. Figure 29 shows that the ISM forms a well–defined concentration around the BGPS 6737 object; here, the column density value increases to ~4.3x10^{23} cm^{-2}.

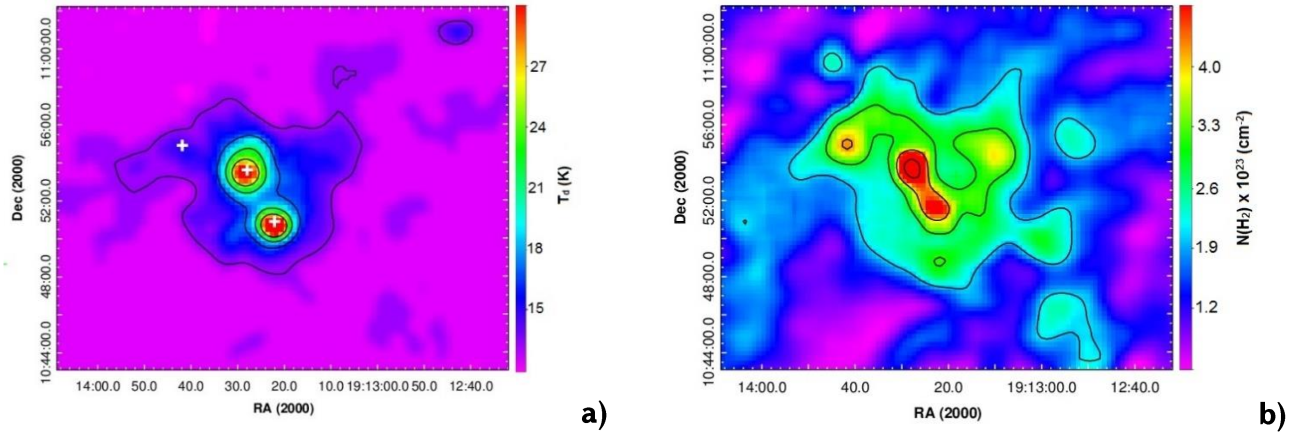

Figure 29. Maps of T_d (**a**) and N(H_2) (**b**) of the region surrounding G45.12+0.13 and G45.07+0.13 UCHII objects [17]. On the T_d map, the outer isotherm corresponds to 13 K and the interval between isotherms is 4 K. On the N(H_2) map, the outer isodense corresponds to 2.0x10^{23} cm^{-2} and interval between isodenses is 1.0x10^{23} cm^{-2}. The positions of the IRAS and BGPC 6737 sources are marked by white crosses.

4.3.3. Stellar population

To select and study the potential stellar members of the star-forming region, we focused on the part of the molecular cloud where the surface brightness at 500 μm exceeds the background brightness by 3σ. This forms a circle with a 6 arcmin radius around the geometric center α= 19:13:24.2, δ= +10:53:38, as shown in Figure 28. Taking into account the completeness limit of GPS UKIDSS-DR6 and provided noise probability, it yielded approximately 28 000 objects. The MIR and FIR catalogues were cross-matched with the GPS UKIDSS-DR6 catalogue within 3σ of the combined error matching radius (Col. 3 in Table 1).

To confirm the existence of clusters in the vicinity of both IRAS sources, we constructed the radial density distribution of stars with respect to IRAS 19110+1045 and 19111+1048 (grey line and black line, respectively, Figure 30). The stellar density was determined in rings of width 0.1′ by dividing the number of stars by the surface area. The standard error for the number of stars in each ring is used as a measure of uncertainty. The radial density distribution of the stars shows a well-defined concentration of stars around the IRAS19110+1045 source, confirming the existence of a cluster. Starting from a ~0.8′ radius, the stellar density does not exceed the average density of the field. The existence of a cluster around the IRAS19111+1048 source is not well-defined and no density concentration was recorded around the MSX G045.1663+00.0910 source.

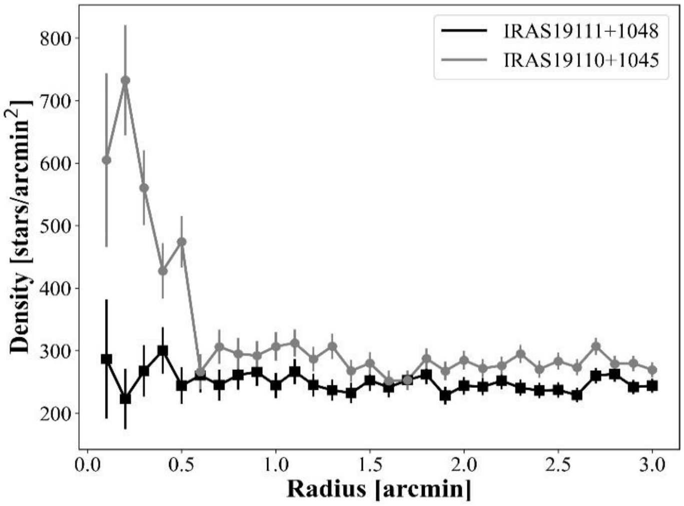

Figure 30. Radial distribution of the stellar densities relative to IRAS19111+1048 (black line) and IRAS19110+1045 (grey line) sources, respectively [17]. Vertical lines are standard errors.

Depending on the available data, we constructed six c-c diagrams for the selection of YSOs in this star-forming region. Figure 31 **a**) shows the (J-H) versus (H-K) c-c diagram. A total of 5,135 YSO candidates were selected using the (J-H) versus (H-K) c–c diagram. Other objects in the reddening band are generally considered to be either field stars or Class III objects with small NIR excess. The latter objects can be potential members of the star-forming region, however, differentiating between field stars and Class III objects is very difficult. Thus, we added to the final list those objects from this sample that were classified as Class I and Class II evolutionary stage YSOs in at least two other c–c diagrams.

Figure 31 **b**) shows the K-[3.6] versus [3.6]-[4.5] c-c diagram. A total of 1,016 YSO candidates were selected using this c-c diagram.

Figure 31 **c**) shows the [3.6]-[4.5] versus [5.8]-[8.0] c-c diagram with *Spitzer* IRAC wavelengths. Three sources exhibit colours in-consistent with Class I, Class II, or reddened photosphere models. One source exhibits a higher [3.6]–[4.5] colour value than Class II objects, but lower [5.8]–[8.0] colour than Class I objects. We identify this source as a reddened Class II object. The other two sources have [5.8]–[8.0] > 1.1, consistent with Class I objects, but [3.6]–[4.5] < 0.4, which is lower than predicted by Class I models [4]. Since these objects share the properties of Class I and Class II sources, we refer to them as Class I/II [137]. In total, 42 YSO candidates were selected using the [3.6]–[4.5] versus [5.8]–[8.0] c–c diagram.

Figure 31 **d**) shows the [3.6]–[5.8] versus [8.0]–[24] c-c diagram where we used *Spitzer* IRAC and MIPS wavelengths. We selected 17 YSO candidates using this diagram.

We also constructed two other c-c diagrams using the list of objects with good WISE detections, i.e. those possessing photometric uncertainty < 0.2 mag in WISE bands. Figure 31 **e**) and **f**) show the [3.4]-[4.6] versus [4.6]-[12] and [3.4]-[4.6] versus [4.6]-[22] c-c diagrams, respectively. A total of 130 YSO candidates were selected using these diagrams.

We also measured the α_{IRAC} slope values for each of the sources detected in all four IRAC bands (3-8 μm) and selected YSOs according to the criteria presented in Section 2.3.2. The selection of YSOs by α_{IRAC} slope is based on the same fluxes as used in the [3.6]–[4.5] versus [5.8]–[8.0] c-c diagram, however, in this case, 186 objects were added to the YSO candidates.

We firstly checked our list of YSOs for galaxies dominated by PAH emission. Notably, no sources on our list satisfy these conditions. By filtering the list of YSOs, we identify 26 sources that satisfied the conditions of the broad-line AGNs, 14 of which were already classified as YSOs from other c-c diagrams. In addition, 113 sources were identified as possible AGB stars among our list, 64 of which were already classified as YSOs in other c-c diagrams. Thus, in total, we removed 78 objects from the list of YSO candidates.

The investigated region is quite distant and large, thus, there is a high probability of selecting objects that do not belong to the molecular cloud. On the other hand, PMS objects with comparatively small NIR excesses may be located in the reddening band and are therefore excluded from the selection. To minimise the likelihood of making an incorrect selection, we selected YSOs on the criterion of being stars classified as objects with IR excess by at least two different selection methods, i.e. the c-c diagrams and α_{IRAC} slope. However, since the region has two saturated areas in the MIR band around the IRAS objects (IRAS19110+1045 with 25″ radius and IRAS19111+1048 with 50″ radius), this can lead to the potential loss of objects belonging to the molecular cloud. Accordingly, objects within those areas classified as YSOs based on only the NIR c-c diagram were included in the list of candidate YSOs. We selected the dominant evolutionary stage for each object in our chosen methods. In the case of equality, the older stage was selected. In the c-c diagrams (see Figure 31), Class I and Class II YSOs are indicated with blue filled circles. Non-classified objects are shown with black circles.

In total, we selected 909 YSOs within a 6 arcmin radius, which includes 849 Class II and 60 Class I objects. Among these, 56 objects were selected based on MIR photometric data.

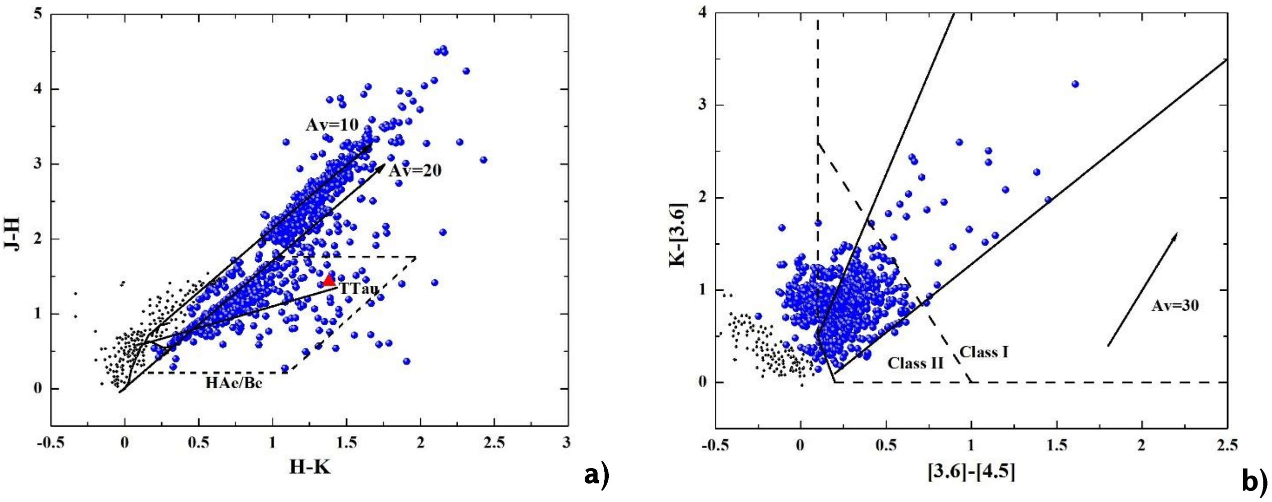

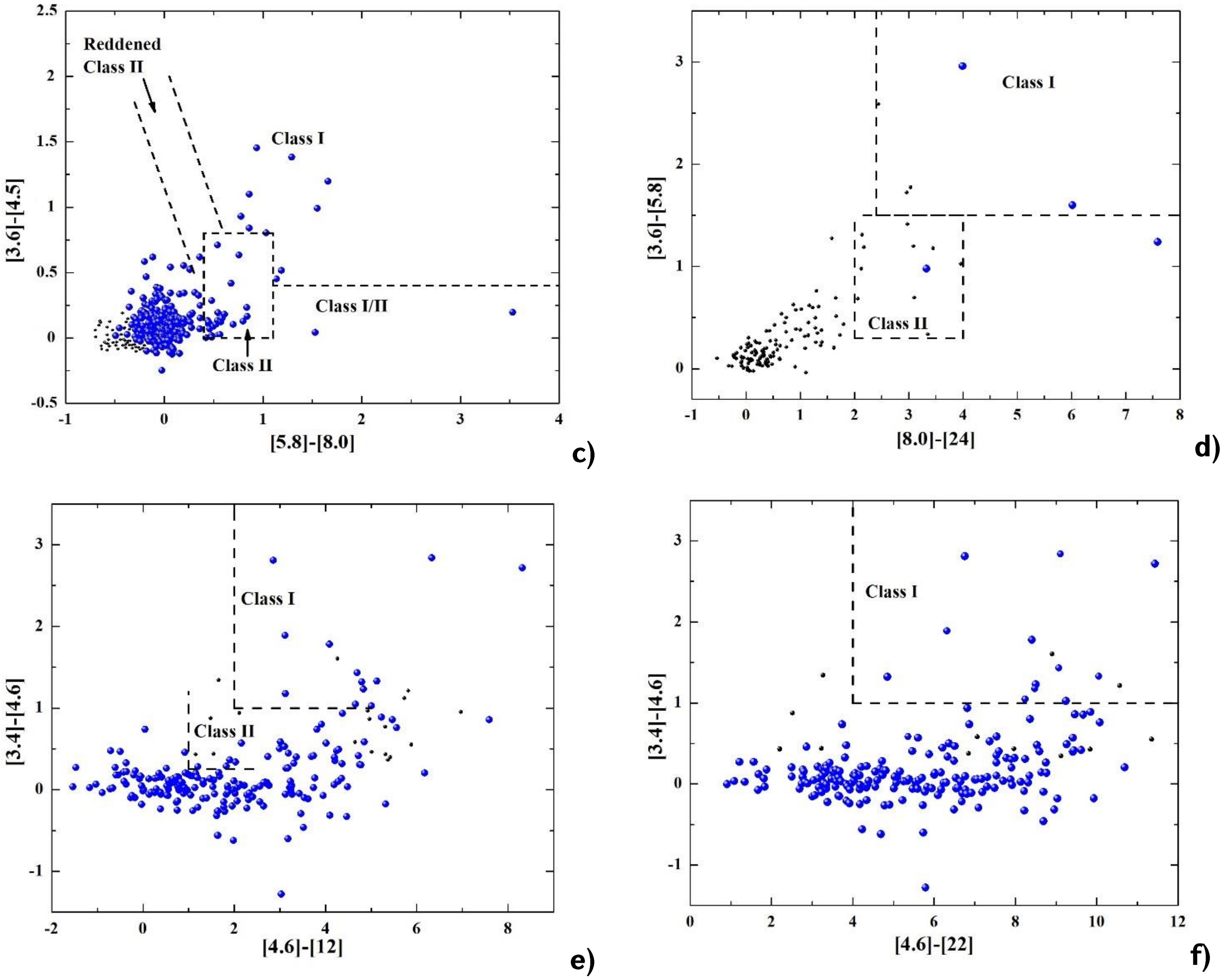

Figure 31. C-c diagrams of the IRAS 19110+1045 and 19111+1048 star-forming regions [17]: **a)** (J-H) vs. (H-K), **b)** K-[3.6] vs. [3.6]-[4.5], **c)** [3.6]-[4.5] vs. [5.8]-[8.0], **d)** [3.6]-[5.8] vs. [8.0]-[24], **e)** and **f)** are [3.4]-[4.6] vs. [4.6]-[12] and [3.4]-[4.6] vs. [4.6]-[22] diagrams, respectively. All the lines in diagrams are the same as in Figure 3. The blue circles are selected YSO candidates and black circles are non-classified ones. Not all non-classified objects are presented in these diagrams. IRAS19111+1048 source is indicated by a red triangle.

4.3.4. SED analysis

We used the command-line version of the SED fitting tool where numerous precomputed models are available. This procedure was performed using wavelengths ranging from 1.1 to 500 μm, in particular, J, H, and K (UKIDSS); 3.6, 4.5, 5.8, and 8.0 μm (*Spitzer* IRAC); 24 μm (*Spitzer* MIPS); 3.4, 4.6, 12, and 22 μm (WISE); 70 and 160 μm (*Herschel* PACS), 70, 160, 250, 350, and 500 μm (Hi-GAL). We considered as an upper limit the FIR fluxes that were identified as closest by coordinates to the NIR object to avoid possible errors. For interstellar extinction, we chose an interval of 10–1000 mag that would exceed the results obtained by COBE/DIRBE and IRAS/ISSA maps (A_v = 10–50 mag, [179]). The distance interval corresponds to the estimates made in the previous studies (6.5–9.5 kpc).

As we selected YSOs in two MIR–saturated regions using only their J, H, and K magnitudes, constructing their SEDs based on only three photometric data points does not provide a reliable basis for any conclusions (115 YSOs). Excluding these objects, we achieved relatively robust parameters for 431 of the 793 selected YSOs (16 Class I and 415 Class II) with χ^2<100 that composes 55% of the total number. The fact that reliable parameters could not be determined for the remaining 45% of objects can be explained by several reasons, which likely include errors in the identification and selection of objects.

To estimate the reliability of the results obtained by the SED fitting tool, we carried out the same analysis in a control field. For Control field 1, we selected a region located in the vicinity of but outside the GRSMC 45.46+0.05 star-forming region [184]. Figure 33 shows the position of the Control field 1 with the same 6 arcmin radius. The stellar population analysis of the Control field 1 involved the same steps previously described in Section 4.3.3. We selected 250 probable YSO candidates out of 33,676 objects identified in UKIDSS DR6. For the SED analysis, we used the same A_v ranges and distances. As a result, we obtained relatively robust parameters for only 12 objects with χ^2<100.

The stellar content analysis of Control field 1 allows us to conclude that the 431 YSOs (χ^2<100) selected by the SED fitting tool in our considered region are located with high probability at the same distance as two UCHII regions. By examining the distances corresponding to the models obtained with the SED fitting tool, we found that, for most objects, the best models correspond to a distance of 7.8 kpc. For the other 45% of the objects, the SED fitting tool did not yield a reliable result. In addition to the aforementioned reasons, this issue may relate to the presence of fore/background objects. The latter issue is especially likely because the region is distant.

4.3.5. Final catalogue

As noted earlier, we included objects in the initial UKIDSS DR6 selection with the catalogue parameter mergedClass = +1 (galaxy) and –3 (probable galaxy). Among these, there may be some artefacts or so-called non-stellar objects [186]. The reasons for their formation may be manifold, including nebulous structures, diffraction patterns of bright stars, bright stars at or near the border of the detector array, etc. To justify the reliability of the final list, we reviewed our sample for artefacts. For this purpose, following the advice of previous works (e.g. [129]; [186]), the parameter k_1ppErrBits was used. This parameter contains the quality error information for each source detected by the K filter. Among the 431 objects with robust SEDs, only one showed k_1ppErrBits = 64 (i.e. bad pixel(s)) and seven showed k_1ppErrBits = 4 194 304 (i.e. lies within a dither offset of the stacked frame boundary); we thus excluded these from the final list. Such a small percentage of artefacts (~2%) indicates sufficiently reliable filtering of stellar objects using the SED fitting tool.

We also performed a visual inspection of the 115 YSO candidates that were selected based only on their NIR photometric data. From our point of view, these objects are of the greatest interest as they are located in the immediate vicinity of the UCHIIs. The analysis results are shown in Figure 32. The surface brightness distribution of 20 faint objects indicates that they can be attributed to extended/non-stellar objects rather than point sources. In UKIDSS DR6, they were identified as galaxies/probable galaxies (mergedClass = +1/–3). These objects are marked with red circles in Figure 32. To ensure the purity of the sample, we removed these objects from the final list.

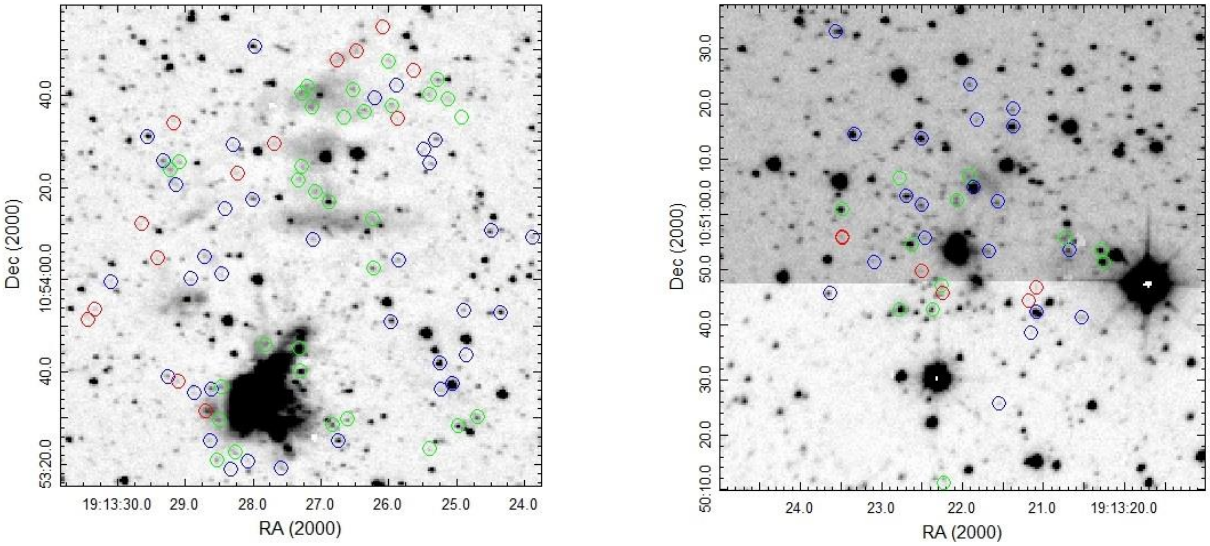

Figure 32. K image of G45.07+0.13 (top panel) and G45.12+0.13 (lower panel). The selected YSOs with mergedClass = -1/-2 (star/probable star marked by blue circles, mergedClass = +1/-3 (galaxy/probable galaxy) - by green circles [17]. Red circles show the identified non-stellar objects.

Overall, the final list comprised 518 YSOs (423 with constructed SEDs and 95 YSOs in two saturated regions). The coordinates, NIR and MIR photometric data, α_{IRAC}, and the evolutionary stage of the 518 YSOs are presented in Table 15, while Table 16 presents the FIR fluxes of the selected objects. In total, we identified 23 objects in FIR bands, including the object associated with IRAS19111+1048. Table 17 shows the weighted means and the standard deviation values of parameters for all models with χ^2 - χ^2_{best} < 3N obtained by the SED fitting tool. In Table 15, Table 16, Table 17, the parameters of the members of the region are listed in the following order: first, the IRAS19111+1048 source then objects within the IRAS 19111+1048 and 19110+1045 clusters (see Section 4.3.6), and, finally, those within a 6 arcmin radius of the whole region that are not included in the clusters. The numbering of objects in Table 17 was performed according to Table 15 and Table 16. Table 17 contains the parameters of the 423 objects for which the SED fitting tool achieved a value of χ^2<100.

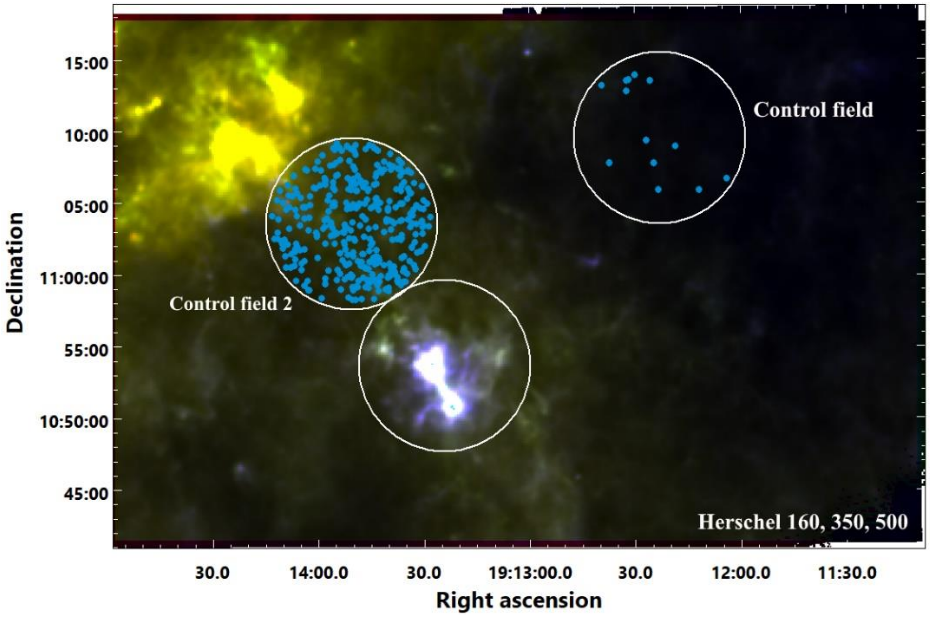

Figure 33. *Herschel* 160 (blue), 350 (green), 500 (red) μm colour-composite image of the considered region and two Control fields with the same 6 arcmin radius [17] around the centres with coordinates $\alpha_{(2000)}$=19:12:22.86, $\delta_{(2000)}$=11:09:30.7 (Control field 1), and $\alpha_{(2000)}$=19:13:52.96, $\delta_{(2000)}$=11:03:23.5 (Control field 2). YSOs selected by SED fitting tool (see Section 4.3.4) in both Control fields are indicated in filled blue circles.

Some conclusions can be drawn based on the data obtained by the SED fitting tool. The average interstellar extinction value is equal to A_v=13 mag, which corresponds to a lower interstellar extinction estimate than that obtained from the COBE/DIRBE and IRAS/ISSA maps [179]. The average mass of the YSOs is approximately 4.4 $M_\odot$, with a minimum estimated mass of 1.7 $M_\odot$ and a maximum of 22 $M_\odot$. Primarily, the lack of low-mass stellar objects can be explained by the large distance of the star-forming region.

Table 15. NIR and MIR photometric data of selected YSOs

ID	α(2000) (hh mm ss)	δ(2000) (dd mm ss)	J (mag)	H (mag)	K (mag)	[3.6] (mag)	[4.5] (mag)	W1 (mag)	W2 (mag)	W3 (mag)	W4 (mag)	α	Cl
(1)	(2)	(3)	(4)	(5)	(6)	(7)	(8)	(9)	(10)	(11)	(12)	(13)	(14)
IRAS19111+1048													
IR*	19 13 27.3	10 53 32.4	16.8	15.3	14.0	-	-	-	-	-	-	-	II
20	19 13 25.3	10 54 8.2	18.6	17.6	16.5	-	-	-	-	-	-	-	II
86	19 13 29.1	10 54 15.6	20.0	18.8	17.7	-	-	-	-	-	-	-	II
IRAS19110+1045													
134	19 13 23.4	10 50 9.8	17.4	16.0	15.1	14.2	13.7	-	-	-	-	-	II
140	19 13 23.7	10 51 32.8	-	-	16.0	13.5	12.4	12.0	10.2	6.1	1.8	-	I
Others													
158	19 13 3.4	10 52 49.6	18.8	15.8	14.4	13.6	13.4	-	-	-	-	-	II
239	19 13 12.1	10 51 29.2	19.6	16.3	14.8	14.1	13.8	-	-	-	-	-	II
280	19 13 16.6	10 50 56.3	19.5	18.3	17.4	-	-	11.1	10.8	6.4	2.8	-1.1	II
455	19 13 36.1	10 54 11.2	17.9	15.9	14.8	14.1	13.7	-	-	-	-		II
505	19 13 41.5	10 55 16.5	19.3	17.8	16.4	14.5	13.8	-	-	-	-		II

Notes. (1) - ID number in final list of YSOs, (2),(3) - position taken from the UKIDSS survey, (4)–(12) - apparent magnitudes, (12) - classification of YSOs according to c-c diagrams and α_{IRAC}. W1–W4 are four bands of WISE survey. (*)- IRAS19111+1048. The full table is available in VizieR On-line Data Catalog: J/other/PASA/39.24.

Table 16. FIR photometric data of selected YSOs

ID	α(2000) (hh mm ss)	δ(2000) (dd mm ss)	[70] μm (mJy)	[160] μm (mJy)	[250] μm (mJy)	[350] μm (mJy)	[500] μm (mJy)	Cl
(1)	(2)	(3)	(4)	(5)	(6)	(7)	(8)	(9)
				IRAS19111+1048				
IR*	19 13 27.34	10 53 32.45	-	1326590	-	-	-	II
20	19 13 25.30	10 54 8.29	14369	-	-	-	-	II
86	19 13 29.15	10 54 15.62	-	125230	78693	-	-	II
				IRAS19110+1045				
134	19 13 23.40	10 50 9.89	-	218656	-	-	-	II
140	19 13 23.75	10 51 32.81	2118	-	-	-	-	I
				Others				
158	19 13 3.41	10 52 49.65	-	658	-	-	-	II
239	19 13 12.17	10 51 29.28	-	-	-	-	15212	II
280	19 13 16.60	10 50 56.32	2351	-	-	-	-	II
455	19 13 36.15	10 54 11.28	-	12527	-	-	-	II
505	19 13 41.50	10 55 16.58	-	-	-	14589	-	II

Notes. (1) - ID number in final list of YSOs, (2),(3) - position taken from the UKIDSS survey and HiGAL 160 μm (4)–(8) - measured fluxes, (9) - classification of YSOs. (*)- IRAS19111+1048. The full table is available in VizieR On-line Data Catalog: J/other/PASA/39.24.

4.3.6. Distribution of YSOs

The top panel of Figure 34 shows the distribution of the selected YSOs in the field, with Class I and Class II objects shown by filled red and blue circles, respectively. Excluding the regions in the vicinity of the IRAS sources, all types of stellar objects are distributed relatively homogeneously in the molecular cloud. Additionally, in both UCHII regions, close to the IRAS sources, the selected YSOs form relatively dense concentrations or clusters. These concentrations were revealed above by the radial distribution of stellar densities (see Figure 30). The existence of the cluster around IRAS19111+1048 is more obvious now. We refined the radius of each cluster relative to its geometric centre based on the density distribution of the selected YSOs. The stellar density was determined for each ring of width 0.1′ by dividing the number of YSOs by the surface area. The radius of each cluster was considered the distance at which fluctuations in the rings' stellar density became random according to Poisson statistics. Table 18 presents the coordinates of the geometric centres of the clusters in the vicinity of IRAS sources and the whole region in Cols. 2 and 3, the coordinates of IRAS sources in Cols. 4 and 5, and the radii of the clusters in Col. 6. Cols. 7 and 8 present the stellar content and surface density of each cluster, as well as of the whole region, based on our selection. The surface density of stars in clusters is four times higher than that of the entire region. The radii of the clusters are in good agreement with the sizes of the UC HII regions as determined by the distributions of dust temperature and column density (see Section 4.3.2). Note that in previous studies, the young massive (OB) population embedded in the innermost regions of the clump has already been reported (e.g. [197]; [169]). The two insets in the lower panels of Figure 34 show the distribution of the members in the dense clusters. The yellow and purple circles correspond to older and younger populations, respectively. The size of each circle is related to its mass falling within certain mass intervals: 1–3 $M_{\odot}$ (smallest), 3–5 $M_{\odot}$, 5–7 $M_{\odot}$, and > 7 $M_{\odot}$ (largest). The colour and size of the members are taken based on their positions on the CMD (see Figure 35 left panel). The surface density distribution of the YSOs did not show any concentration around the BGPS 6737 (MSX G045.1663+00.0910) object.

[197] proposed that the initial trigger and power source of G45.12+0.13 is the brightest radio source S14, which was deduced to be of spectral type O6 from integrated radio emission. They also found two NIR objects, IR4 and IR5, within S14. According to our data, the nearest object to the S14 peak (~7.7′′) that can satisfy the conditions defined in [197] is a star with 9.4±4.3 $M_{\odot}$ mass, 23 000±11 000 K temperature, and (2.5±1.2)x10^6 years evolutionary age. This star is mentioned as IRAS19111+1048 in Table 15, Table 16, Table 17, and the NIR c-c diagram. It is also the closest object (~9′′) to the brightest source A16-24 obtained by the CORNISH interferometer at 4.8 GHz [169]. This stellar object has II evolutionary class. Besides IRAS19111+1048 source, two selected YSOs are also located within the radio contours of S14, i.e. stars ID 52 and 53 in Table 15, which are located at distances about 8.5 and 11′′ from the S14 peak, respectively. This group of objects can be assumed to be the power source of G45.12+0.13. [127] also suggested that S14 is a protocluster hosting several ZAMS stars.

Table 17. Parameters derived from [171] models SED fitting.

ID	A_v (mag)	Distance (kpc)	Age (Log)(yr)	Mass $M_\odot$	Temperature (K)	MdotE (Log)($M_\odot$yr^{-1})	MdotD (Log)($M_\odot$yr^{-1})	L_{Total} (Log)($L_\odot$)	CI
(1)	(2)	(3)	(4)	(5)	(6)	(7)	(8)	(9)	(10)
				IRAS19111+1048					
IR*	12.0	8.7	6.40	9.4	22928	-8.4	-7.8	3.8	II
20	10.9	7.6	5.01	8.5	10371	-3.3	-6.0	3.4	0/I
86	10.0	6.5	4.13	12.6	6333	-2.2	-4.9	3.8	0/I
				IRAS19110+1045					
134	12.0	7.2	6.37	4.4	12765	-9.2	-11.8	2.6	-
140	24.9	8.9	5.50	7.9	15175	-4.7	-6.3	3.4	0/I
				Others					
158	18.2	7.9	4.99	3.9	4515	-4.0	-6.7	2.0	0/I
239	16.0	7.1	3.90	15.3	6206	-2.2	-6.1	4.1	0/I
280	11.1	8.1	5.33	5.9	7930	-3.2	-6.6	2.8	0/I
455	13.8	7.8	5.75	4.7	6044	-4.8	-6.0	2.3	0/I
505	10.8	7.7	4.36	11.1	6515	-2.6	-4.8	3.6	0/I

Notes. (1) - ID number in final list of YSOs, (2)-(9) - the weighted means and the standard deviations of parameters obtained by SED fitting tool for all models with best χ^2- χ^2_{best} < 3N, (10) - Stage of YSOs. (*)-IRAS 19111+1048. The full table is available in VizieR On-line Data Catalog: J/other/PASA/39.24.

According to [197], IRAS19110+1045 is associated with the compact radio source S27, which has no NIR counterparts. Using the SED fitting tool, [160] obtained embedded pair of YSOs with the mass of 24 $M_\odot$ associated with IRAS19110+1045. Unfortunately, due to the saturation of the central parts of UCHII regions in the MIR range, we were unable to identify the YSOs associated with this source.

We examined the location of identified stellar objects in relation to radio sources [197]; [169]. Table 19 includes objects that are located no further than 5′′ from the peak of the radio sources. For the majority, we see that at least one stellar object can be associated with a radio source from [197].

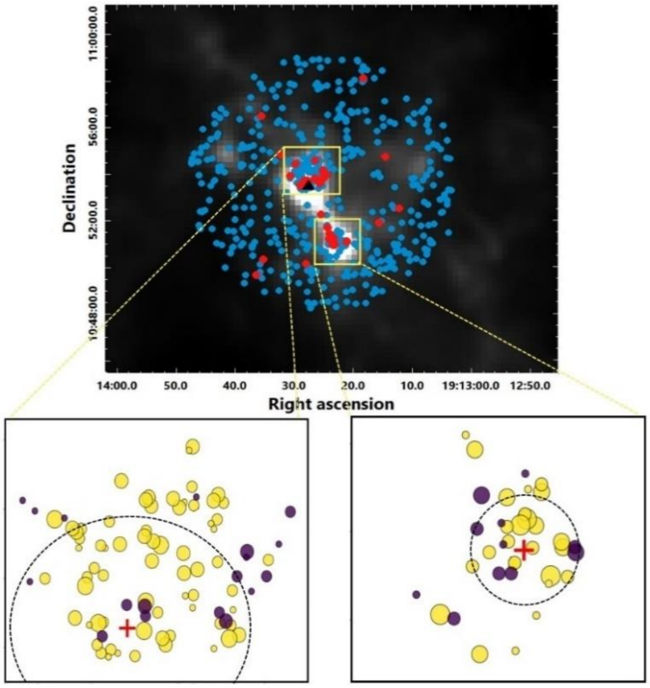

Figure 34. (*Top panel*): Distribution of YSOs in the region on *Herschel* 500 μm image [17]. Class I and Class II objects are indicated by filled red and blue circles, respectively. IRAS19111+1048 source is indicated by a black triangle. (*Bottom panels*): The two insets show the distribution of the clusters' members. Yellow and purple circles correspond to an older and younger population, respectively. The size of each circle is related to its mass falling within certain interval of masses: 1–3 $M_\odot$ (smallest), 3–5 $M_\odot$, 5–7 $M_\odot$ > 7 $M_\odot$ (largest). The colour and size of the members are taken based on their positions on the CMD (Figure 35 left panel). Red crosses show the coordinates of IRASs. Dashed circles shows the MIR-saturated regions around the IRAS sources.

Table 18. Properties of the region

IRAS	α(2000) (hh mm ss)	δ(2000) (dd mm ss)	α(2000) (hh mm ss)	δ(2000) (dd mm ss)	Radius (arcmin)	N	Density (arcmin^{-2})
(1)	(2)	(3)	(4)	(5)	(6)	(7)	(8)
19111+1048	19 13 27.8	+10 53 36.74	19 13 27.3	+10 54 07.42	1.2	87	19.2
19110+1045	19 13 22.0	+10 50 54.00	19 13 23.1	+10 50 51.88	0.8	37	18.4
Region	-	-	19 13 24.2	+10 53 38.00	6	518	4.6

Notes. (1)-names of (sub-)regions, (2),(3)- coordinates of the IRAS sources, (4),(5)- coordinates of the geometric centres, (6)-the radii of (sub-)regions, (7)- numbers of objects within the selected radii, (8)-surface stellar density in the (sub-)regions.

Table 19. Comparison of IR and radio data.

ID	GMRT	CORNISH	ID	GMRT	CORNISH
(1)	(2)	(3)	(1)	(2)	(3)
10	S3	-	63, 68	S18	-
11	S6	-	64	-	A16-C32
16	S5	-	65, 71	S16	-
26, 36	S10	-	66	-	A16-C33
37	S9	-	74	S19	-
43, 45	S12	-	87, 88	S24	-
50, 53	-	A16-C8	91	S25	-
56	-	A16-C25	98	S27	A12-C1
58	S15	-	120	-	A16-C5
59, 60	-	A16-C27	105	-	A12-C3

Notes. (1)—ID of objects from Table 15, (2)—sources obtained by radio continuum observations at 1 280, 610 MHz frequency bands [197], (3)—sources obtained by CORNISH interferometer at 4.8 GHz [169].

4.3.7. Colour-magnitude diagram

The distribution of the identified YSOs in the K versus J–K CMD is shown in the left panel of Figure 35. Circles indicate stars in the IRAS clusters, while red circles are stars with more than three photometric measurements. For these stars, the SED fitting tool obtained reliable parameters (i.e. χ^2 <100). Yellow circles represent objects in the saturated regions that have only three photometric measurements. Objects located outside of the two IRAS clusters (hereafter *non-cluster*) for which the SED fitting tool obtained reliable parameters are marked by blue crosses. The black dots are objects with no reliable parameters (χ^2>100). To correct the J and K magnitudes of the selected YSOs, we used a 7.8 kpc distance and the average interstellar extinction value (A_v = 13 mag). Using the excess vector, we also determined the photometric limit of the UKIDSS data represented by the dashed arrow in the diagram; this is parallel to the excess vector and passes through the ZAMS point with coordinates (0.34, 2.05). The Y-coordinate corresponds to the photometric limit of UKIDSS in K band (18.02 mag) corrected for distance and interstellar extinction. The photometric limit corresponds to the ZAMS stars with 1.4 $M_{\odot}$ mass; this value is in good agreement with the minimum mass (i.e. 1.7 $M_{\odot}$), obtained by the SED fitting tool. We observe that all detected objects are brighter in the K-band than the photometric limit of the UKIDSS survey. Undoubtedly, the large distance and interstellar extinction play a crucial role in this result.

Several conclusions can be drawn based on the location of stellar objects in the CMD. Objects without reliable parameters (black dots) occupy a separate region; in general, these are brighter in the K-band than objects with reliable parameters and most of them are likely foreground objects. The stars that belong to the star-forming region (circles and crosses) have considerable variation concerning their colour index, i.e. $(J-K)_{abs}$. The positions of objects in the two IRAS clusters and non-cluster regions are different. An overwhelming majority (more than 80%) of the non-cluster objects are located to the right of the 0.1 Myr isochrone. In contrast, about 75% of objects in the IRAS clusters are located to the left of the 0.1 Myr isochrone and concentrated around the ZAMS, some of which fall to the left of the ZAMS. For improved clarity, the histograms of $(J-K)_{abs}$ are shown in the top panels of Figure **35**. In general, the evolutionary age spread of the vast majority of stellar objects from both samples is small; furthermore, the members of the IRAS clusters are more developed than the non-cluster objects.

The middle panel of Figure **36** shows the distribution of evolutionary ages (by the SED fitting tool) for the non-cluster objects, which confirms the above interpretation. The age distribution of these objects has a well-defined peak at Log(Age)≈5.25. In contrast, the distribution of the evolutionary ages of the objects in the clusters has two peaks (Figure **36** top panel) centred at Log(Age)≈6.75 and Log(Age)≈5.25. Note that the age distribution of the objects in the clusters was constructed based on parameters from only 29 YSOs for which the SED fitting tool was applied. Most of the other 95 YSOs in the MIR-saturated regions are concentrated around the ZAMS and to the left of the 1 Myr isochrone. Therefore, we assume that these objects will have a real contribution to the first peak in the evolutionary age distribution. Accordingly, this distribution will have only one well-defined peak as per the histogram of $(J-K)_{abs}$ around Log(Age)≈6.75.

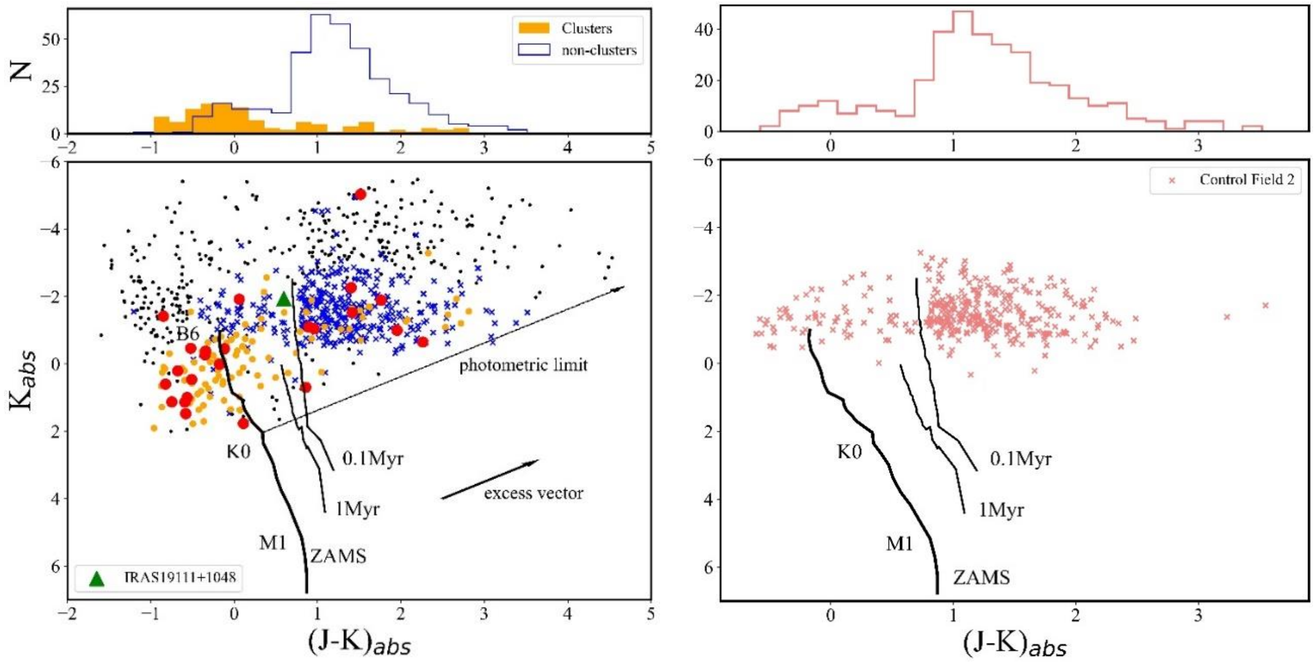

Figure 35. K versus (J–K) CMDs [17] for identified YSOs in the considered region (*bottom left panel*) and Control field 2 (*bottom right panel*). The J and K magnitudes of the YSOs are corrected for the interstellar extinctions determined according to average A_v = 13 mag value obtained by the SED fitting tool. (bottom left panel): Red circles are stellar objects within the IRAS clusters with constructed SED based on more than 3 photometric data points. Objects located in the saturated regions around two IRAS sources are yellow circles. Non-cluster objects are blue crosses and no-SED objects are black dots. IRAS19111+1048 source is indicated by a green triangle and labelled. The solid arrow indicates the average slope of NIR excesses caused by circumstellar discs [128]. The dashed arrow indicates the photometric limit of UKIDSS in K-band. (*bottom right panel*): Stellar objects located in Control field 2 are indicated by coral crosses. (*Top left and right panels*): Histograms of $(J–K)_{abs}$ values.

The cluster identification confirms the assumptions made in previous studies based mainly on radio observations of star clusters near the IRAS sources, which include high- and intermediate-mass ZAMS objects (e.g. [127]; [169]; [197], and ref. therein). The clusters' members exhibit low scatter relative to the isochrones. The clusters' origin can be assumed to relate to an external triggering shock. We examined the distribution of the cluster members relative to their masses and evolutionary ages (see the lower panels of Figure 34), which demonstrated that the objects are not segregated according to these parameters. The members of the IRAS19111+1048 cluster are asymmetrically arranged relative to the IRAS source, and, like the isotherms (see Figure 29), are elongated in a north-west direction. There are potentially two UCHIIs herein (i.e. G45.12+0.13 and G45.13+0.14) that are separated from each other in a northwest direction [54].

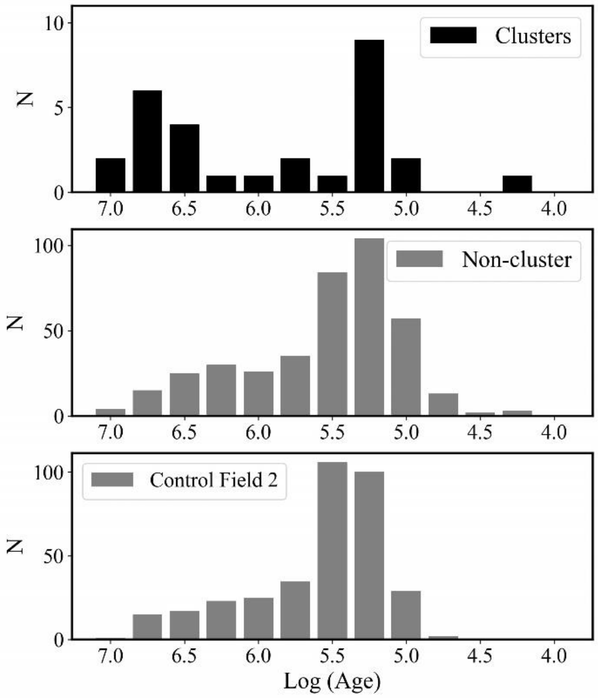

Figure 36. Histogram of evolutionary ages [17] for members of the IRAS clusters (*top panel*), the non-cluster objects (*middle panel*), and the objects in the Control field 2 (*bottom panel*). The bin size corresponds to Log(Age)=0.25.

The non-cluster objects of all evolutionary classes are uniformly distributed across the field (see Figure 34 top panel). As shown in previous studies, several massive stellar objects in or near the ZAMS are responsible for the ionisation of UCHII regions and can trigger a second star formation event along the ionising radiation ridge (e.g. [29]; [159]). Accordingly, the newly formed stars are unevenly distributed and localised in the radiation ridge. In our study, the non-cluster YSOs are found to be uniformly distributed in the molecular cloud. Therefore, the origin of the non-cluster objects cannot be explained by the activity of the embedded massive stars in the UCHII regions. We instead assume that these uniformly distributed objects are part of the young stellar population of the GRSMC 45.46+0.05 molecular cloud, which is an active star-forming region [184].

To confirm this assumption, we performed the same analysis in Control field 2, an area we selected that is located in the GRSMC 45.46+0.05 star-forming region and very close to the considered region. Figure 33 shows the position of Control field 2 with the same 6 arcmin radius. The analysis of the stellar population of Control field 2 includes the same steps described in Section 4.3.3. We selected 777 YSO candidates out of 30,254 objects identified in UKIDSS DR6. For the SED analysis of these YSO candidates, we used the same A_v and distance ranges of 10–100 mag and 6.5–9.5 kpc, respectively. We obtained relatively robust parameters for ~350 objects (χ^2 <100); therefore, the number of YSOs in Control field 2 is almost the same as the number of non-cluster objects in the considered region. The mass range of these objects also coincides (from 1.9 to 18 $M_{\odot}$). The evolutionary age distributions of the non-cluster stellar objects and Control field 2 objects show significant similarity (see bottom panel of Figure 36), with the Control field 2 object ages exhibiting one well-defined peak. The distribution of evolutionary ages and the peak value (Log(Age)≈5.35) coincide with those of the non-cluster objects. To further confirm the similarity between the non-cluster and Control field 2 stellar objects, we also used CMD. The distribution of the objects from Control field 2 in the K versus J–K CMD is shown in the right panel of Figure 35 (coral crosses). We used the same correction as previously for the J and K photometry, i.e. 7.8 kpc distance and A_v = 13 mag interstellar extinction. More than 80% of the objects are located to the right of the 0.1 Myr isochrone, like the non-cluster objects. Thus, the main parameters (evolutionary ages, masses, and surface stellar density) of the non-cluster and Control field 2 objects are almost the same. Accordingly, our assumption that the non-cluster YSOs are part of the young stellar population of the GRSMC 45.46+0.05 molecular cloud is plausible. To understand the tracers of their origins, the star formation history of the GRSMC 45.46+0.05 star-forming region as a whole must be investigated.

4.3.8. KLF and IMF

We evaluated the α slopes individually for the stellar populations of the IRAS clusters and the non-cluster objects. The KLF slopes were estimated by fitting the number of YSOs in 0.5 mag bins using a linear least-squares fitting routine. Figure 37 shows the observed overplotted KLFs of the IRAS clusters (dark grey) and the non-cluster objects (light grey). No sharp decline is recorded at the end of KLF as a whole, i.e. it occurs gradually, showing that the photometric completeness limit of the survey did not strongly affect the shape of the KLF. Note that the KLF of the IRAS clusters does not show an obvious maximum while the KLF of the non-cluster objects has a maximum at the same magnitude as the whole region. This is most likely due to the quantitative ratio between the objects from different samples. Its slope is also noticeably steeper than that of the IRAS clusters' KLF. Thus, the IRAS clusters appear to show unique characteristics relative to the whole region, once again confirming that they are at different stages of evolution. The calculated KLF α slopes for the IRAS clusters and non-cluster objects were 0.23±0.10 and 0.55±0.09, respectively.

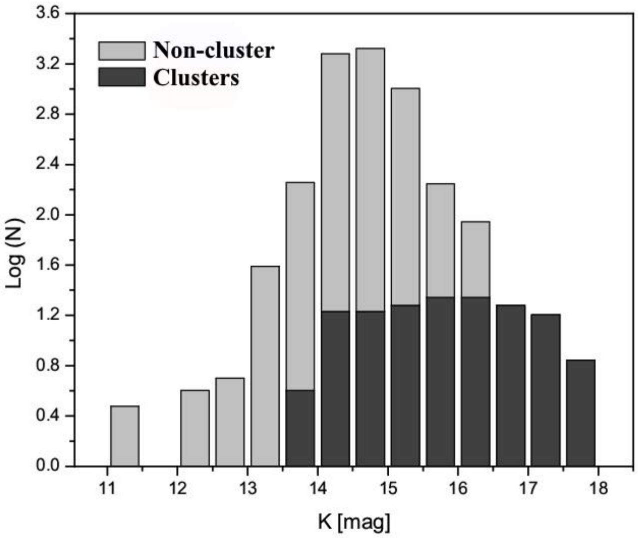

Figure 37. KLFs are derived for the IRAS clusters (dark grey) and non-cluster objects (light grey) as histograms of the number of stars in logarithm versus apparent K magnitude [17]. The bin size corresponds to 0.5 mag.

One of the most fundamental disciplines of astrophysical research is the origin of stars and stellar masses. The IMF, together with the star formation rate, dictates the evolution and fate of both galaxies and star clusters [106]. The study of the IMFs of star-forming regions is important—their mass functions (MFs) can be considered as IMFs because they are too young to lose a significant number of members through dynamical or stellar evolution effects. We assume that the MF and the mass-luminosity relation for a stellar cluster are described by power laws like the KLF, i.e. they are of the form $dN(logm) \propto m^{\gamma}$ and $L_K \propto m^{\beta}$, where γ and β are the slopes of MF and mass-luminosity relation, respectively. We obtained two completely different KLF results for the two IRAS clusters and the non-cluster objects. Here, we discuss the IMF of each case separately as the initial conditions may differ. The mass-luminosity relation with $\beta \sim 1$ is mostly used for stars at the lower mass end of the IMF, i.e. G–M stars for the 1 Myr cluster

[118]; [138]. If $\beta \sim 1$, values such as $\alpha = \gamma/(2.5\beta) = 0.68$ and 0.54 would be expected for power-law IMFs with slopes γ = 1.7 [141]; [178] and 1.35 [175], respectively. The latter value is in good agreement with our KLF fit result for the non-cluster stellar objects (0.55±0.09). If we assume $\beta \sim 2$, typically used for a larger and higher mass range (O–F stars) at 1 Myr [21], this results in α = 0.27 for a Salpeter-type IMF and α = 0.34 for a Miller-Scalo type IMF. The Salpeter-type IMF is closer to the KLF fit result for the two IRAS clusters (0.23±0.10). The results obtained via the IMFs are well-correlated with the masses obtained from the SED fitting tool (see Section 4.3.4). Notably, the 1 Myr age estimate for the non-cluster objects does not match with the results of the SED fitting tool and CMD (see Figure 36 and Figure 35)—in general, the non-cluster objects are noticeably younger. Such a discrepancy is because the mass-luminosity relation with $\beta \sim 1$ is used mostly for low-mass stars, while the SED fitting tool did not find any low-mass objects in the region and the CMD shows that the photometric limit of UKIDSS in the K-band influenced the detection of faint objects in the region. Thus, the resulting loss of low-mass YSOs in the region will strongly affect the results of the SFR and SFE calculation, so we did not define these parameters.

4.3.9. Conclusions

An infrared study of the star-forming region in a molecular cloud, which includes the UCHII regions G45.12+0.13/IRAS19111+1048 and G45.07+0.13/IRAS19110+1045, was undertaken with two major components: (i) determination of the ISM physical parameters (i.e. N(H_2) and T_d) and (ii) searching for and studying the young stellar population. To determine N(H_2) and T_d, we applied modified blackbody fitting on *Herschel* images obtained in four bands: 160, 250, 350, and 500 μm. The maps of these parameters allowed us to conclude:

- Within the G45.07+0.13 and G45.12+0.13 regions, N(H_2) varies from ~3.0x10^{23} to 5.5x10^{23} cm^{-2}.
- The T_d maximum in G45.12+0.13 is 35 K and in G45.07+0.13 it is 42 K.
- The dust temperature drops significantly from the centre to the periphery, reaching values of around 18–20 K. The T_d decline levels out at distances of ~2.6 and ~3.7 pc from IRAS 19110+1045 and 19111+1048, respectively. The masses of the gas-dust matter are ~1.7x10^5 $M_\odot$ and ~3.4x10^5 $M_\odot$ in the G45.07+0.13 and G45.12+0.13 regions, respectively.

- The N(H_2) map revealed a bridge between the two UCHII regions with relatively high density (4.3x10^{23} cm^{-2}) and low temperature (19 K), which is also clearly visible on *Herschel* images. This suggests that these two UCHII regions are physically connected.

The objectives of studying the stellar population were to identify the members of the clusters, associated with the UCHII regions, as well as to determine their main parameters (e.g. stellar masses, evolutionary ages, and age spread). The identification and classification of YSOs using NIR, MIR, and FIR photometric data were based on one of the main properties of young stars, namely, their infrared excess due to the presence of circumstellar discs and envelopes. The SED fitting tool [172] was used to determine their main parameters. Within a 6 arcmin radius around the UCHIIs, we obtained relatively robust parameters for 423 YSOs (16 Class I and 407 Class II objects) with χ^2 <100. We also identified 95 YSOs located in the two MIR-saturated regions based only on the J, H, and K photometric data. A detailed study of stellar objects in the considered star-forming region made it possible to obtain the following results:

- The stellar density radial distribution shows the existence of dense clusters in the vicinity of both IRAS sources. These clusters include 37 and 87 members in G45.07+0.13 and G45.12+0.13, respectively. Their surface stellar density exceeds the average over the star-forming region around fourfold. The radii are in good agreement with the sizes of the UCHII regions as determined by the distributions of dust temperature and column density. The remaining 394 non-cluster objects, irrespective of their evolutionary classes, are uniformly distributed in the molecular cloud.
- We were unable to identify stellar objects with masses less than 1.4 $M_{\odot}$. This can be explained by the large distance of the star-forming region.
- The study of the stellar parameters from different samples (i.e. clusters and non-cluster) showed differences between the two populations.
- On the CMD, around 75% of the YSOs in the IRAS clusters are located to the left of the 0.1 Myr isochrone and are concentrated around the ZAMS. The slope α of the KLF for these objects is 0.23±0.10, which agrees well with a Salpeter-type IMF (γ = 1.35) for a high mass range (O–F stars, β ~ 2) at 1 Myr.
- The detailed study of the clusters made it possible to identify the stellar object associated with IRAS19111+1048, and this can be the exciting star of G45.12+0.13. This is a star with 9.4±4.3 $M_{\odot}$ mass, 23 000±11 000 K temperature, and (2.5±1.2)x10^6 yr evolutionary age.

- The median value of the evolutionary ages obtained by the SED fitting tool for the non-cluster objects is Log(Age)≈5.25, more than 80% of which are located to the right of the 0.1 Myr isochrone. The slope α of the KLF for these objects is 0.55±0.09, which agrees better with a Salpeter-type IMF for low-mass objects (G–M stars, $\beta \sim 1$).

Based on the results, we concluded that dense clusters were formed in both UCHII regions, which include high- and intermediate-mass stellar objects. The evolutionary ages of these stars, in most cases, are several million years. Likely, low-mass stellar objects were not identified due to the large distance of the star-forming region. The small spread of evolutionary ages suggests that the clusters owe their origin to a triggering shock. Presumably, the low-density extended emission observed on the MIR images [54], which also stands out well on the dust temperature maps in both UCHII regions, may be due to the existence of the stellar clusters. The distribution of the non-cluster objects in the molecular cloud implies that their origin cannot be explained by the activity of the embedded massive star(s) in the UCHII regions. We assume that these uniformly distributed objects are part of the young stellar population of the GRSMC45.46+0.05 molecular cloud, which is an active star-forming region. To understand the tracers of their origins, it is necessary to investigate the star formation history of the GRSMC45.46+0.05 star-forming region as a whole. This extended star-forming region, spreading over an area of about 6 deg^2 in Aquila, is known to host numerous UCHII regions, maser emissions, and outflows from young and highly embedded OB stellar clusters (e.g. [184]; [169]). This work is also a part of the project to study the UCHII regions in GRSMC45.46+0.05, and, consequently, massive star formation and its influence on the surrounding ISM.

CHAPTER 5

5. CONCLUSIONS

Firstly, this thesis is focused on the identification of compact young stellar clusters on the bases of UKIDSS GPS and *Spitzer* data. According to NIR and MIR data, out of 20 IRAS sources, we were able to statistically identify compact groups of YSOs in the vicinity of 12 and 4 IRAS sources, respectively. This represents 80% of the overall number of regions that were studied and is substantially higher than the results based on data from the 2MASS survey, with lower sensitivity and resolution. The identified YSOs are not always located at the center of the discovered cluster (see Figure 4). This can be explained by the density gradient of the interstellar medium in the clusters, which significantly distorts the real picture. In 12 out of 19 identified regions (~63%), the IRAS sources are associated with a binary or even a group of YSOs. At least for these 20 regions, we may conclude that around middle- and high-mass YSO, in a certain stage of evolution, form a group of YSOs and with modified selection criteria (depth of images, longer wavelength range), the percentage of detected groups should increase. Undoubtedly, the search and detection of compact star-forming regions can be considered just an initial stage of research. There is a whole series of questions that will require a more detailed approach and more extensive databases: at what evolutionary stage does YSO form compact groups in its vicinity? Does the richness of a cluster depend on the mass and age of the central object, for example, in clusters concentrated around Herbig Ae/Be stars [193]? How do the properties of clusters depend on the parameters of the surrounding medium? Do the properties of the young stellar population reflect which process dominated the formation of the cluster, namely continuous self-condensating or external triggering? To address these questions, we selected three star-forming regions for the detailed study.

All regions were not chosen by chance. The main selection criteria are their considerable extent and multicomponent complex structure, which implies the presence of several local nests of star formation. The regions are little studied, but at the same time, there is sufficient observational data about them for our study. Besides, the preliminary studies shown that the star-forming regions differ in their stellar composition and structural properties [16]. As a result, we have chosen three star formation regions, namely IRAS 05137+3919, 05168+3634, and 19110+1045. And the second part of this thesis is focused on the detailed infrared study of the three star-forming regions with different masses, which includes two tasks: (i) determination of the ISM physical parameters (i.e. $N(H_2)$ and T_d) and (ii) searching for and studying the young stellar population.

To determine $N(H_2)$ and T_d, we applied modified blackbody fitting on *Herschel* images obtained in four bands: 160, 250, 350, and 500 μm. The maps of these parameters allowed us to conclude:

- The highest column density and dust temperature were obtained within the G45.07+0.13 (IRAS19110+1045) and G45.12+0.13 (IRAS19111+1048) UCHII regions: from ~3.0×10^{23} to 5.5×10^{23} cm^{-2} and ~40 K, respectively.
- The dust temperature in the IRAS05137+3919 and IRAS05168+3634 star-forming regions are almost the same: from 11 to 24 K, however, the column density is relatively lower in the IRAS05137+3919 region: from 0.3 to 1.0×10^{23} cm^{-2}, rather than in IRAS05168+3634 region: from 1.0 to 4.0×10^{23} cm^{-2}.

The identification and classification of YSOs using NIR, MIR, and FIR photometric data were based on one of the main properties of young stars, namely, their infrared excess due to the presence of circumstellar discs and envelopes. The SED fitting tool [172] was used to determine their main parameters. A detailed study of stellar objects in the considered star-forming region made it possible to obtain the following results:

- The stellar density radial distributions of the star-forming regions show the existence of dense clusters in the vicinity of the IRAS sources.
- We identified 84 YSOs in the vicinity of IRAS05137+3919 (6 arcmin radius) and the surface stellar density in the cluster exceeds density in the field twice. We identified a close pair of intermediate-mass YSOs with this IRAS object.
- We obtain the census of young stellar populations within a 24 arcmin radius region surrounding the molecular cloud where the IRAS05168+3634 and other four IRAS sources are located; this includes 1224 YSO candidates, 240 of which are concentrated around these five IRAS sources. The surface stellar density in the clusters exceeds density in the field more than three times. All five IRAS sources have NIR counterparts and one of them, namely IRAS05162+3639, is associated with a low-mass binary object, and the other four IRAS sources are associated with a single intermediate-mass YSO.

- The identified 518 YSOs exhibit dense clusters in the vicinity of IRAS 19110+1045 and 19111+1048 sources and the surface stellar density in the clusters exceeds density in the field at least four times. We were able to identify a massive stellar object associated only with the IRAS19111+1048 source.
- The number of identified YSOs is undoubtedly a lower limit of the total number in the star-forming regions. On one hand, this incompleteness is explained by the imperfection of the selection method and, on the other hand, by the large distance to the clusters which would undoubtedly primarily affects on detection of low-mass objects.
- There is an obvious direct relationship between surface stellar density and hydrogen column density. Moreover, in IRAS05168+3634 star-forming region, the subregions with the higher hydrogen column density have a larger percentage of YSOs with the Class I evolutionary stage.
- The Class I sources are often distributed within the detected clusters, while the Class II sources are more widely distributed. This fact can be explained, among other factors, that more "older" Class II YSOs had more time to move away from their birthplace.
- CMDs and SED fitting tool obtained massive young stellar objects only in the IRAS 19110+1045 and 19111+1048 where two UCHII regions are located.
- We did not obtain massive stars in the molecular cloud surrounding IRAS05168+3634 and the other four IRAS star-forming regions (IRAS 05184+3635, 05177+3636, 05156+3643, and 05162+3639), however higher masses have been obtained in those regions where the column density is higher, i.e. towards the IRAS05168+3634 source.
- The KLFs of the IRAS05137+3919 and IRAS05158+3634 star-forming regions show unusually low values for the α slope: from 0.12 to 0.18. According to these values, the age of these two star-forming regions can be estimated between 0.1 and 3 Myr. The evolutionary age distributions of these star-forming regions also show a large age spread. This suggests that the stellar populations in the IRAS05137+3919 and IRAS05158+3634 star-forming regions are formed as a result of independent condensations in their parent molecular clouds, and, therefore, the star formation process is sequential.
- The slope α of the KLF for the clusters in the IRAS 19110+1045 and 19111+1048 star-forming region is 0.23 ± 0.10, which agrees well with a Salpeter-type IMF (γ = 1.35) for a high mass range (O–F stars, $\beta\ \sim 2$) at 1 Myr. The evolutionary ages of these stars, in most cases, are several million

years. The small spread of evolutionary ages suggests that the clusters owe their origin to a triggering shock.

- Among considered star-forming regions, massive stars were detected only in the region where star formation was probably triggered, that are IRAS19110+1045 and 19111+1048.

ACKNOWLEDGEMENTS

After an overstretched period of time my PhD finally comes to an end. In this part of the thesis I will thank everyone who have supported me during my PhD.

I would like to express my sincere gratitude to my dear supervisor Dr. Elena Nikoghosyan for her useful advice and the continuous support of my PhD and before that also of my MSc. She encouraged me to grow as an independent scientist and her guidance helped me in all the time of my research. As a supervisor, she always supports me to take advantage all of the travelling opportunities. During this years we became friends with whom I can discuss various topics even not scientific.

I am thankful to Dr. Areg Mickaelian who always encouraged me to participate in different astronomical meetings, such as summer schools and conferences which contributed greatly to my scientific career. I would like to express my heartfelt thanks to Dr. Haik Harutyunian for welcoming me kindly at the Byurakan Astrophysical Observatory at the very beginning and for always supporting me.

I would like to thank my friends at Byurakan Astrophysical Observatory and not only for their sincere support with whom I had a lot of joyful time. I am grateful to my senior colleagues at Byurakan Astrophysical Observatory who are always ready to give important advice when I have questions related to my research.

I express my deepest thanks to my family for infinite support and advice to never stand still and always look forward! I am thankful to my new family, Derenik Andreasyan, who helped me up when I fell!

In conclusion, thank you to everyone who has been patiently waiting for **this day.**

6. REFERENCES

[1] Abrahamyan H. V., Mickaelian A. M., and Knazyan A. V., "*The IRAS PSC/FSC Combined Catalogue*" A&C, 2015, 10, pp. 99-106

[2] Agekian T., "*Theory of Probability for Astronomy and Physics*" Moscow: Nauka Publishing House, 1974

[3] Ali B. and Depoy D. L., "*A 2.2 Micron Imaging Survey of the Orion a Molecular Cloud*" AJ, 1995, 109, p. 709

[4] Allen L. E., Calvet N., D'Alessio P., et al., "*Infrared Array Camera (IRAC) Colors of Young Stellar Objects*" ApJS, 2004, 154, pp. 363-366

[5] Allen L. E., Myers P. C., Di Francesco J., et al., "*Hubble Space Telescope/NICMOS Imaging Survey of the Ophiuchus (Lynds 1688) Cluster*" ApJ, 2002, 566, pp. 993-1004

[6] Allen L., Megeath S. T., Gutermuth R., et al., "*The Structure and Evolution of Young Stellar Clusters*" University of Arizona Press, 2007, pp. 361-376

[7] Ambartsumian V. A., "*The evolution of stars and astrophysics*" Armenian Acad. Sci., Erevan, U.S.S.R., 1947

[8] Ambartsumian V. A., "*Stellar systems of positive total energy*" The Observatory, 1955, 75, pp. 72-78

[9] André P., "*The Initial Conditions for Protostellar Collapse: Observational Constraints*" EAS Publications Series, 2002, 3, pp.1-38

[10] André P. and Montmerle T., "*From T Tauri Stars to Protostars: Circumstellar Material and Young Stellar Objects in the rho Ophiuchi Cloud*" ApJ, 1994, 420, p. 837

[11] André P., Men'shchikov A., Bontemps S., et al., "*From filamentary clouds to prestellar cores to the stellar IMF: Initial highlights from the Herschel Gould Belt Survey*" A&A, 2010, 518, p. 7

[12] André P., Ward-Thompson D., and Barsony M., "*From Prestellar Cores to Protostars: the Initial Conditions of Star Formation*" The University of Arizona Press, 2000, p. 59

[13] Aniano G., Draine B. T., Gordon K. D., and Sandstrom K., "*Common-Resolution Convolution Kernels for Space- and Ground-Based Telescopes*" PASP, 2011, 123, p. 1218

[14] Argon A. L., Reid M. J., and Menten K. M., "*Interstellar Hydroxyl Masers in the Galaxy. I. The VLA Survey*" ApJS, 2000, 129, pp. 159-227

[15] Azatyan N. M. and Nikoghosyan E. H., "*Investigation of the stellar content in the IRAS 05168+3634 star-forming region*" ComBAO, 2018, 65, pp. 228-239

[16] Azatyan N. M., Nikoghosyan E. H., and Khachatryan K. G., "*Search for Compact Stellar Groups in the Vicinity of Iras Sources*" Astrophysics, 2016, 59, pp. 339-353

[17] Azatyan N., Nikoghosyan E., Harutyunian H., Baghdasaryan D., and Andreasyan D., "*Infrared study of the star-forming region associated with the UC HII regions G45.07+0.13 and G45.12+0.13*" PASA, 2022, 39, e024

[18] Azatyan N., Nikoghosyan E., Harutyunian H., Baghdasaryan D., and Andreasyan D., "*Stellar population in two star-forming regions*" ComBAO, 2020, 67, pp. 211-218

[19] Bachiller R., "*Bipolar Molecular Outflows from Young Stars and Protostars*" ARA&A, 1996, 34, pp. 111-154

[20] Bailer-Jones C.A.L., Rybizki J., Fouesneau M., Demleitner M., and Andrae R., "*Estimating Distances from Parallaxes. V. Geometric and Photogeometric Distances to 1.47 Billion Stars in Gaia Early Data Release 3*" AJ, 2021, 161, p. 24

[21] Balog Z., Kenyon S. J., Lada E. A., et al., "*A Near-Infrared (JHK) Survey of the Vicinity of the H II Region NGC 7538: Evidence for a Young Embedded Cluster*" AJ, 2004, 128, pp. 2942-2953

[22] Battersby C., Bally J., Ginsburg A., et al., "*Characterizing precursors to stellar clusters with Herschel*" A&A, 2011, 535, p. 17

[23] Baug T., Ojha D. K., Dewangan L. K., et al., "*Sh2-138: physical environment around a small cluster of massive stars*" MNRAS, 2015, 454, pp. 4335-4356

[24] Bernstein R. A., Freedman W. L., and Madore B. F., "*The First Detections of the Extragalactic Background Light at 3000, 5500, and 8000 Å. III. Cosmological Implications*" ApJ, 2002, 571, pp. 107-128

[25] Bessell M. S. and Brett J. M., "*JHKLM Photometry: Standard Systems, Passbands, and Intrinsic Colors*" PASP, 1988, 100, p. 1134

[26] Bica E., Dutra C. M., and Barbuy B., "*A Catalogue of infrared star clusters and stellar groups*" A&A, 2003, 397, pp. 177-180

[27] Bica E., Ortolani S., and Barbuy B., "*B and V photometry of the faint open cluster UKS 2 (BH 66)*" A&AS, 2000, 145, pp. 399-403

[28] Blitz L., "*Star Forming Giant Molecular Clouds*" NATO Advanced Study Institute (ASI) Series C, 1991, 342, p. 3

[29] Blum R. D. and McGregor P. J., "*The Ionizing Stars of the Galactic Ultra-Compact HII Region G45.45+0.06*" AJ, 2008, 135, pp. 1708-1717

[30] Bohlin R. C., Savage B. D., and Drake J. F., "*A survey of interstellar H I from Lalpha absorption measurements. II.*" ApJ, 1978, 224, pp. 132-142

[31] Bonnell I., Bate M., Clarke C., and Pringle J., "*Accretion and the stellar mass spectrum in small clusters*" MNRAS, 1997, 285, pp. 201-208

[32] Boss A.P. and Yorke H.W., "*Spectral Energy of First Protostellar Cores: Detecting "Class -I" Protostars with ISO and SIRTF*" ApJ, 1995, 439, p. L55

[33] Breen S. L., Contreras Y., Dawson J. R., et al., "*84-GHz methanol masers, their relationship to 36-GHz methanol masers, and their molecular environments*" MNRAS, 2019, 484, pp. 5072-5093

[34] Bressert E., Bastian N., Gutermuth R., et al., "*The spatial distribution of star formation in the solar neighbourhood: do all stars form in dense clusters?*" MNRAS, 2010, 409, pp. L54-L58

[35] Bronfman L., Nyman L.-A., and May J. "*A CS(2-1) survey of IRAS point sources with color characteristics of ultra-compact HII regions*" A&AS, 1996, 115, p. 81

[36] Campbell B., Persson S. E., and Matthews K., "*Identifications of New Young Stellar Objects Associated with IRAS Point Sources. III. The Northern Galactic Plane*" AJ, 1989, 98, p. 634

[37] Cardelli J. A., Clayton G. C., and Mathis J. S., "*The Relationship between Infrared, Optical, and Ultraviolet Extinction*" ApJ, 1989, 345, p. 245

[38] Carey S. J., Noriega-Crespo A., Mizuno D. R., et al., "*MIPSGAL: A Survey of the Inner Galactic Plane at 24 and 70 μm*" PASP, 2009, 121, p. 76

[39] Carpenter J. M., "*Color Transformations for the 2MASS Second Incremental Data Release*" AJ, 2001, 121, pp. 2851-2871

[40] Carpenter J. M., Meyer M. R., Dougados C., Strom S. E., and Hillenbrand L. A., "*Properties of the Monoceros R2 Stellar Cluster*" AJ, 1997, 114, pp. 198-221

[41] Carpenter J. M., Snell R. L., Schloerb F., and Skrutskie M. F., "*Embedded Star Clusters Associated with Luminous IRAS Point Sources*" ApJ, 1993, 407, p. 657

[42] Casoli F., Dupraz C., Gerin M., Combes F., and Boulanger F., "*13CO and 12CO observations of cold IRAS unidentified point sources inthe galaxy*" A&A, 1986, 169, pp. 281-297

[43] Caulet A., Gruendl R. A., and Chu Y. H., "*Young Stellar Objects in the Large Magellanic Cloud: N63 and N180 HII Regions*" ApJ, 2008, 678, pp. 200-218

[44] Cesaroni R., Massi F., Arcidiacono C., et al., "*Star and jet multiplicity in the high-mass star forming region IRAS 05137+3919*" A&A, 2015, 581, p. 46

[45] Chen H., Tafalla M., Greene T. P., Myers P. C., and Wilner D. J., "*IRAS 20050+2720: An Embedded Young Cluster Associated with a Multipolar Outflow*" ApJ, 1997, 475, pp. 163-172

[46] Churchwell E., "*Ultra-Compact HII Regions and Massive Star Formation*" ARA&A, 2002, 40, pp. 27-62

[47] Churchwell E., Babler B. L., Meade M. R., et al., "*The Spitzer/GLIMPSE Surveys: A New View of the Milky Way*" PASP, 2009, 121, p. 213

[48] Churchwell E., Sievers A., and Thum C., "*A millimeter survey of ultra-compact HII-regions and associated molecular clouds*" A&A, 2010, 513, pp. 13

[49] Churchwell E., Walmsley C. M., and Wood D. O. S., "*Hot, dense, molecular gas associated with ultracompact HII regions*" A&A, 1992, 253, pp. 541-556

[50] Compiègne M., Verstraete L., Jones A., et al., "*The global dust SED: tracing the nature and evolution of dust with DustEM*" A&A, 2011, 525, pp. 14

[51] Coupeaud A., Demyk K., Meny C., et al., "*Low-temperature FIR and submillimetre mass absorption coefficient of interstellar silicate dust analogues*" A&A, 2011, 535, pp. 15

[52] Cutri R. M., Skrutskie M. F., van Dyk S., et al., "*VizieR Online Data Catalog: 2MASS All-Sky Catalog of Point Sources (Cutri+ 2003)*" VizieR Online DataCatalog, 2003

[53] Dalessandro E., Miocchi P., Carraro G., J ǐlkov á L., and Moitinho A., "*Evidence of tidal distortions and mass-loss from the old open cluster NGC 6791*" MNRAS, 2015, 449, pp. 1811-1818

[54] de la Fuente E., et al., "*Ultracompact HII regions with extended emission: the complete view*" MNRAS, 2020a, 492, pp. 895-914

[55] de la Fuente E., et al., "*Ultracompact H II regions with extended emission: the case of G43.89-0.78 and its molecular environment*" MNRAS, 2020b, 497, pp. 4436-4447

[56] Desert F., Boulanger F., and Puget J. L., "*Interstellar Dust Models for Extinction and Emission*" A&A, 1990, 237, 215

[57] Di Francesco J., Johnstone D., Kirk H., MacKenzie T., and Ledwosinska E., "*The SCUBA Legacy Catalogues: Submillimeter-Continuum Objects Detected by SCUBA*" ApJS, 2008, 175, pp. 277-295

[58] Dobashi K., "*Atlas and Catalog of Dark Clouds Based on the 2 Micron All Sky Survey*" PASJ, 2011, 63, pp. S1-S362

[59] Dobashi K., Uehara H., Kandori R. et al., "*Atlas and Catalog of Dark Clouds Based on Digitized Sky Survey I*" PASJ, 2005, 57, pp. S1-S386

[60] Draine B. T., "*Interstellar Dust Grains*" ARA&A, 2003, 41, pp. 241-289

[61] Edris K. S., Fuller G. A., and Cohen R. J., "*A survey of OH masers towards high mass protostellar objects*" A&A, 2007, 465, pp. 865-877

[62] Egan M. P., Price S. D., Kraemer K. E., et al., "*VizieR Online Data Catalog: MSX6C Infrared Point Source Catalog. The Midcourse Space Experiment Point Source Catalog Version 2.3 (October 2003)*" VizieR Online Data Catalog, 2003

[63] Ehlerová S. and Palouš J., "*HI shells in the outer Milky Way*" A&A, 2005, 437, pp. 101-112

[64] Ellsworth-Bowers T. P., Rosolowsky E., Glenn J., et al., "*The Bolocam Galactic Plane Survey. XII. Distance Catalog Expansion Using Kinematic Isolation of Dense Molecular Cloud Structures with* ^{13}*CO(1-0)*" ApJ, 2015, 799, pp. 25

[65] Elmegreen B. G., Efremov Y., Pudritz R., and Zinnecker H., "*Observations and Theory of Star Cluster Formation*" University of Arizona Press, 2000, p. 179

[66] Elmegreen B. G. and Lada C. J. "*Sequential formation of subgroups in OB associations*" ApJ, 1977, 214, pp. 725-741

[67] Fall S. M., Krumholz M. R., and Matzner C. D., "*Stellar Feedback in Molecular Clouds and its Influence on the Mass Function of Young Star Clusters*" ApJ, 2010, 710, pp. L142-L146

[68] Faustini F., Molinari S., Testi L., and Brand J., "*Properties of stellar clusters around high-mass young stars*" A&A, 2009, 503, pp. 801-816

[69] Fazio G. G., Hora J. L., Allen L. E., et al., "*The Infrared Array Camera (IRAC) for the Spitzer Space Telescope*" ApJS, 2004, 154, pp. 10-17

[70] Ferrière K., "*The interstellar environment of our galaxy*" RvMP, 2001, 73, pp. 1031-1066

[71] Fish V. L., Reid M. J., Wilner D. J., and Churchwell E., "*HI Absorption toward Ultracompact HII Regions: Distances and Galactic Structure*" ApJ, 2003, 587, pp. 701-713

[72] Flaherty K. M., Pipher J. L., Megeath S. T., et al., "*Infrared Extinction toward Nearby Star-forming Regions*" ApJ, 2007, 663, pp. 1069-1082

[73] Fontani F., Cesaroni R., and Furuya R. S., "*Class I and Class II methanol masers in high-mass star-forming regions*" A&A, 2010, 517, pp. 24

[74] Gålfalk M. and Olofsson G., "*A detailed study of the L1641N star formation region*" A&A, 2008, 489, pp. 1409-1439

[75] Ginsburg A., Glenn J., Rosolowsky E., et al., "*The Bolocam Galactic Plane Survey. IX. Data Release 2 and Outer Galaxy Extension*" ApJS, 2013, 208, pp. 15

[76] Gomez M., Hartmann L., Kenyon S.J., and Hewett R., "*On the Spatial Distribution of pre-Main-Sequence Stars in Taurus*" AJ, 1993, 105, p. 1927

[77] Goodwin S. P. and Bastian N., "*Gas expulsion and the destruction of massive young clusters*" MNRAS, 2006, 373, pp. 752-758

[78] Grave J. M. C. and Kumar M. S. N., "*Spitzer-IRAC GLIMPSE of high mass protostellar objects. II. SED modelling of a bona fide sample*" A&A, 2009, 498, pp. 147-159

[79] Griffin M. J., Abergel A., Abreu, A., et al., "*The Herschel-SPIRE instrument and its in-flight performance*" A&A, 2010, 518, pp. 7

[80] Guan X., Wu Y., and Ju B., "*A mapping survey of massive CO cores*" MNRAS, 2008b, 391, pp. 869-880

[81] Gutermuth R. A., Megeath S. T., Myers P. C., et al., "*A Spitzer Survey of Young Stellar Clusters Within One Kiloparsec of the Sun: Cluster Core Extraction and Basic Structural Analysis*" ApJS, 2009, 184, pp. 18-83

[82] Gutermuth R. A., Myers P. C., Megeath S. T., et al., "*Spitzer Observations of NGC 1333: A Study of Structure and Evolution in a Nearby Embedded Cluster*" ApJ, 2008, 674, pp. 336-356

[83] Gutermuth R. A., Pipher J. L., Myers P. C., et al., "*A Fresh Look at Distributed vs Clustered Star Formation: Molecular Cloud Surveys with Spitzer*" American Astronomical Society Meeting Abstracts, 2006, 38, p. 87

[84] Han X. H., Zhou J. J., Wang J. Z., et al., "*Combination of CN(1-0), HCN(1-0), and HNC(1-0): A possible indicator for a high-mass star formation sequence in the Milky Way*" A&A, 2015, 576, pp. 47

[85] Harju J., Lehtinen K., Booth R. S., and Zinchenko I., "*A survey of SiO emission towards interstellar masers. I. SiO line characteristics*" A&AS, 1998, 132, pp. 211-231

[86] Hartmann L., "Accretion Processes in Star Formation: Second Edition" Cambridge University Press, 2009

[87] Hartmann L., Megeath S. T., Allen L., et al., "*IRAC Observations of Taurus Pre-Main-Sequence Stars*" ApJ, 2005, 629, pp. 881-896

[88] Henning T. and Stognienko R., "*Dust opacities for protoplanetary accretion disks: influence of dust aggregates*" A&A, 1996, 311, pp. 291-303

[89] Hernández J., Calvet N., Hartmann L., et al., "*Herbig Ae/Be Stars in nearby OB Associations*" AJ, 2005, 129, pp. 856-871

[90] Hernández-Hernández V., Kurtz S., Kalenskii S., et al., "*APEX Millimeter Observations of Methanol Emission Toward High-mass Star-forming Cores*" AJ, 2019, 158, pp. 12

[91] Hernández-Hernández V., Zapata L., Kurtz S., and Garay G., "*SMA Millimeter Observations of Hot Molecular Cores*" ApJ, 2014, 786, pp. 17

[92] Hildebrand R. H., "*The determination of cloud masses and dust characteristics from submillimetre thermal emission*" QJRAS, 1983, 24, pp. 267-282

[93] Hillenbrand L. A, Meyer M. R., Strom S. E., and Skrutskie M. F., "*Isolated Star-Forming Regions Containing Herbig AE/BE Stars. I. The Young Stellar Aggregate Associated With BD +40 degrees 4124*" AJ, 1995, 109, p. 280

[94] Hillenbrand L. A. and Hartmann, L. W., "*A Preliminary Study of the Orion Nebula Cluster Structure and Dynamics*" ApJ, 1998, 492, pp. 540-553

[95] Hillenbrand L. A., Strom S. E., Vrba F. J., and Keene J., "*Herbig Ae/Be Stars: Intermediate-Mass Stars Surrounded by Massive Circumstellar Accretion Disks*" ApJ, 1992, 397, p. 613

[96] Hillenbrand L.A., "*On the Stellar Population and Star-Forming History of the Orion Nebula Cluster*" AJ, 1997, 113, pp. 1733-1768

[97] Hofner P. and Churchwell E., "*A survey of water maser emission toward ultracompact HII regions*" A&AS, 1996, 120, pp. 283-299

[98] Hunter T. R., Phillips T. G., and Menten K. M., "*Active Star Formation toward the Ultracompact HII Regions G45.12+0.13 and G45.07+0.13*" ApJ, 1997, 478, pp. 283-294

[99] Johnson D.R.H. and Soderblom D.R., "*Calculating Galactic Space Velocities and Their Uncertainties, with an Application to the Ursa Major Group*" AJ, 1987, 93, p. 864

[100] Jose J., Pandey A. K., Ogura K., et al., "*Optical and near-infrared survey of the stellar contents associated with the star-forming complex Sh2-252*" MNRAS, 2012, 424, pp. 2486-2503

[101] Kenyon S. J., Gomez M., Marzke, R. O., and Hartmann L., "*New Pre-Main-Sequence Stars in the Taurus-Auriga Molecular Cloud*" AJ, 1994, 108, p. 251

[102] Keto E., "*The Formation of Massive Stars by Accretion through Trapped Hypercompact H II Regions*" ApJ, 2003, 599, pp. 1196-1206

[103] Khanzadyan T., Movsessian T. A., Davis C. J., Magakian T. Yu., and Nikogossian E. H., "*GM 2-4: a signpost for low- and intermediate-mass star formation*" MNRAS, 2011, 418, pp. 1994-2003

[104] Koenig X. P., Leisawitz D. T., Benford D. J., et al., "*Wide-field Infrared Survey Explorer Observations of the Evolution of Massive Star-forming Regions*" ApJ, 2012, 744, pp. 24

[105] Koposov S. E., Rix H.-W., and Hogg D. W., "*Constraining the Milky Way Potential with a Six-Dimensional Phase-Space Map of the GD-1 Stellar Stream*" ApJ, 2010, 712, pp. 260-273

[106] Kroupa P., "*The Initial Mass Function of Stars: Evidence for Uniformity in Variable Systems*" Science, 2002, 295, pp. 82-91

[107] Kroupa P., "*Star Cluster Formation and Some Implications for Gaia*" Proc. Stellar Clusters & Associations, 2011, pp.17-27

[108] Kroupa P. and Boily C. M., "*On the mass function of star clusters*" MNRAS, 2002, 336, pp. 1188-1194

[109] Krumholz M. R., Bate M. R., Arce H. G., et al., "*Star Cluster Formation and Feedback*" University of Arizona Press, 2014, pp 243–266

[110] Kumar M. S. N., Keto E, and Clerkin E., "*The youngest stellar clusters. Clusters associated with massive protostellar candidates*" A&A, 2006, 449, pp. 1033-1041

[111] Königl A. and Pudritz R.E., "*Disk Winds and the Accretion-Outflow Connection*" University of Arizona Press, 2000, p. 759

[112] Lada C. J. and Lada E. A., "*Embedded Clusters in Molecular Clouds*" ARA&A, 2003, 41, pp. 57-115

[113] Lada C. J., "*Star formation: from OB associations to protostars*" IAU Symposium, 1987, 115, p. 1

[114] Lada C. J., Alves J. F., and Lombardi M., "*Near-Infrared Extinction and Molecular Cloud Structure*" University of Arizona Press, 2007, pp. 3-15

[115] Lada C. J., Alves J., and Lada, E. A., "*Near-Infrared Imaging of Embedded Clusters: NGC 1333*" AJ, 1996, 111, p. 1964

[116] Lada C. J., Margulis M., and Dearborn D., "*The formation and early dynamical evolution of bound stellar systems*" ApJ, 1984, 285, pp. 141-152

[117] Lada C. J., Muench A. A., Luhman K. L., et al., "*Spitzer Observations of IC 348: The Disk Population at 2-3 Million Years*" AJ, 2006, 131, pp. 1574-1607

[118] Lada C. J., Young E. T., and Greene T. P., "*Infrared Images of the Young Cluster NGC 2264*" ApJ, 1993, 408, p. 471

[119] Lada C.J. and Wilking B.A., "*The nature of the embedded population in the rho Ophiuchi dark cloud : mid-infrared observations*" ApJ, 1984, 287, pp. 610-621

[120] Lada E. A. and Lada C. J., "*Near-Infrared Images of IC 348 and the Luminosity Functions of Young Embedded Star Clusters*" AJ, 1995, 109, p. 1682

[121] Lada E. A., Depoy D. L., Evans II., N. J., and Gatley I., "*A 2.2 Micron Survey in the L1630 Molecular Cloud*" ApJ, 1991, 371, p. 171

[122] Lada C. J. and Adams F. C., "*Interpreting Infrared Color-Color Diagrams: Circumstellar Disks around Low- and Intermediate-Mass Young Stellar Objects*" ApJ, 1992, 393, p. 278

[123] Larson R.B., "*Numerical calculations of the dynamics of collapsing proto-star*" MNRAS, 1969, 145, p. 271

[124] Launhardt R., Stutz A. M., Schmiedeke A., et al., "*The Earliest Phases of Star Formation (EPoS): a Herschel key project. The thermal structure of low-mass molecular cloud cores*" A&A, 2013, 551, pp. 35

[125] Lee H.-T. and Chen W.P., "*Triggered Star Formation by Massive Stars*" ApJ, 2007, 657, pp. 884-896

[126] Lépine S. and Shara M. M., "*A Catalog of Northern Stars with Annual Proper Motions Larger than 0.15" (LSPM-NORTH Catalog)*" AJ, 2005, 129, pp. 1483-1522

[127] Liu M., Tan J. C., De Buizer J. M., et al., "*The SOFIA Massive (SOMA) Star Formation Survey. II. High Luminosity Protostars*" ApJ, 2019, 874, pp. 26

[128] López-Chico T. and Salas L., "*Mass determination for T Tauri stars from JHK Photometry*" RMxAA, 2007, 43, pp. 155-171

[129] Lucas P. W., Hoare M. G., Longmore A., et al., "*The UKIDSS Galactic Plane Survey*" MNRAS, 2008, 391, pp. 136-163

[130] Lucas P.W. and Roche P.F., "*Butterfly star in Taurus: structures of young stellar objects*" MNRAS, 1997, 286, pp. 895-919

[131] Maddox N., Jarvis M. J., Banerji M., et al., "*Far-infrared emission in luminous quasars accompanied by nuclear outflows*" MNRAS, 2017, 470, pp. 2314-2319

[132] Massi F., Lorenzetti D., Giannini T., and Vitali F., "*Star formation in the Vela molecular clouds. IV. Young embedded star clusters towards D-cloud class I sources*" A&A, 2000, 353, pp. 598-616

[133] Mateen M., Hofner P., and Araya E., "*A Survey of the SO* $J_K=1_0-0_1$ *Transition toward Massive Star-forming Regions*" ApJS, 2006, 167, pp. 239-255

[134] McCaughrean M.J. and Stauffer J.R., *"High Resolution Near-Infrared Imaging of the Trapezium: A Stellar Census*" AJ, 1994, 108, p. 1382

[135] McKee C. F. and Ostriker E. C., "*Theory of Star Formation*" ARA&A, 2007, 45, pp. 565-687

[136] Megeath S. T. and Wilson T. L., "*The NGC 281 west cluster. I. Star formation in photoevaporating clumps*" AJ, 1997, 114, pp. 1106-1120

[137] Megeath S. T., Allen L. E., Gutermuth R. A., et al., "*Initial Results from the Spitzer Young Stellar Cluster Survey*" ApJS, 2004, 154, pp. 367-373

[138] Megeath S. T., Herter T., Beichman C., et al., "*A dense stellar cluster surrounding W3 IRS 5*" A&A, 1996, 307, pp. 775-790

[139] Merello M.; Molinari S.; Rygl K. L. J.; et al., "*Thermal balance and comparison of gas and dust properties of dense clumps in the Hi-GAL survey*" MNRAS, 2019, 483, pp. 5355-5379

[140] Meyer M. R., Calvet N., and Hillenbrand L. A., "*Intrinsic Near-Infrared Excesses of T Tauri Stars: Understanding the Classical T Tauri Star Locus*" AJ, 1997, 114, pp. 288-300

[141] Miller G. E. and Scalo J. M., "*The Initial Mass Function and Stellar Birthrate in the Solar Neighborhood*" ApJS, 1979, 41, p. 513

[142] Molinari S., Brand J., Cesaroni R., and Palla F., "*A search for precursors of ultracompact HII regions in a sample of luminous IRAS sources. I. Association with ammonia cores*" A&A, 1996, 308, pp. 573-587

[143] Molinari S., Brand J., Cesaroni R., Palla F., and Palumbo G. G. C., "*A search for precursors of ultracompact H II regions in a sample of luminous IRAS sources. II. VLA observations*" A&A, 1998, 336, pp. 339-351

[144] Molinari S., Schisano E., Elia D., et al., "*Hi-GAL, the Herschel infrared Galactic Plane Survey: photometric maps and compact source catalogues. First data release for the inner Milky Way: +68° ≥ l ≥ -70°*" A&A, 2016, 591, pp. 33

[145] Molinary S., Pezzuto S., Cesaroni R., et al., "*The evolution of the spectral energy distribution in massive young stellar objects*" A&A, 2008, 481, pp. 345-365

[146] Molinary S., Testi L., Rodriguez L. F., and Zhang Q., "*The Formation of Massive Stars. I. High-Resolution Millimeter and Radio Studies of High-Mass Protostellar Candidates*" ApJ, 2002, 570, pp. 758-778

[147] Morales E. F. E., Wyrowski F., Schuller F., and Menten K. M., "*Stellar clusters in the inner Galaxy and their correlation with cold dust emission*" A&A, 2013, 560, pp. 38

[148] Morton D. C. and Adams T. F., "*Effective Temperatures and Bolometric Corrections of Early-Type Stars*" ApJ, 1968, 151, p. 611

[149] Muzerolle J., Megeath S. T., Gutermuth R. A., et al., "*The 24 Micron View of Embedded Star Formation in NGC 7129*" ApJS, 2004, 154, pp. 379-384

[150] Neugebauer G., Habing H. J., van Duinen R., et al., "*The Infrared Astronomical Satellite (IRAS) mission*" ApJ, 1984, 278, pp. L1-L6

[151] Nikoghosyan E. and Azatyan N., "*Young Stellar Cluster in the Vicinity of the IRAS 05137+3919 Source*" Astrophysics, 2014, 57, pp. 330-343

[152] Nikoghosyan E. H., "*PMS objects in the star formation region Cep OB3. II. Young stellar objects in the Hα nebula Cep B*" Astrophysics, 2013, 56, pp. 165-172

[153] Nikoghosyan E. H., Azatyan N. M., Andreasyan D. H., and Baghdasaryan D. S., "*The structure of the IRAS05168+3634 star-forming region*" ApSS, 2021, 366, id.114

[154] Nikoghosyan E. H., Azatyan N. M., and Khachatryan K. G., "*New eruptive variable in the massive star-forming region associated with IRAS 18507+0121*" A&A, 2017, 603, pp. 8

[155] Nikoghosyan E., Azatyan N., Harutyunian H., Baghdasaryan D., and Andreasyan D., "*Properties of ISM in two star-forming regions*" ComBAO, 2020, 67, pp. 187-192

[156] Azatyan N. M., "*Investigation of the stellar content in the IRAS 05168+3634 star-forming region*" A&A, 2019, 22, pp. 22

[157] Ojha D. K., Tamura M., Nakajima Y., et al., "*A Near-Infrared Study of the NGC 7538 Star-forming Region*" ApJ, 2004, 616, pp. 1042-1057

[158] Ott S., "*The Herschel Data Processing System — HIPE and Pipelines — Up and Running Since the Start of the Mission*" Astronomical Society of the Pacific Conference Series, 2010, 434, p. 139

[159] Paron S., Cichowolski S., and Ortega M. E., "*The environs of the ultracompact HII region G45.45+0.06*" A&A, 2009, 506, pp. 789-796

[160] Persi P. and Tapia M., "*Infrared imaging of high-mass young stellar objects: evidence of multiple shocks and of a new protostar/star eclipsing system*" MNRAS, 2019, 485, pp. 784-795

[161] Phelps R. L. and Lada E. A., "*Spatial Distribution of Embedded Clusters in the Rosette Molecular Cloud: Implications for Cluster Formation*" ApJ, 1997, 477, pp. 176-182

[162] Pilbratt G. L., Riedinger J. R., Passvogel T., et al., "*Herschel Space Observatory. An ESA facility for far-infrared and submillimetre astronomy*" A&A, 2010, 518, pp. 6

[163] Poglitsch A., Waelkens C., Geis N., et al., "*The Photodetector Array Camera and Spectrometer (PACS) on the Herschel Space Observatory*" A&A, 2010, 518, pp. 12

[164] Preibisch T., "*The reliability of age measurements for Young Stellar Objects from Hertzsprung-Russell or color-magnitude diagrams*" RAA, 2012, 12, pp. 1-25

[165] Price S. D., Egan M. P., Carey S. J., Mizuno D. R., and Kuchar T. A., "*Midcourse Space Experiment Survey of the Galactic Plane*" AJ, 2001, 121, pp. 2819-2842

[166] Qiu K., Zhang Q., Megeath S. T., et al., "*Spitzer IRAC and MIPS Imaging of Clusters and Outflows in Nine High-Mass Star Forming Regions*" ApJ, 2008, 685, pp. 1005-1025

[167] Reach W. T., Heiles C., and Bernard J.-P., "*Variations between Dust and Gas in the Diffuse Interstellar Medium*" ApJ, 2015, 811, pp. 14

[168] Rieke G. H. and Lebofsky M. J., "*The interstellar extinction law from 1 to 13 microns*" ApJ, 1985, 288, pp. 618-621

[169] Rivera-Ingraham A., Ade, P. A. R., Bock, J. J., et al., "*The BLAST View of the Star-forming Region in Aquila (ell = 45°, b = 0°)*" ApJ, 2010, 723, pp. 915-934

[170] Robitaille T. P., Meade M. R., Babler B. L., et al., "*Intrinsically Red Sources Observed by Spitzer in the Galactic Midplane*" AJ, 2008, 136, pp. 2413-2440

[171] Robitaille T. P., Whitney B. A., Indebetouw R., and Wood K., "*Interpreting Spectral Energy Distributions from Young Stellar Objects. II. Fitting Observed SEDs Using a Large Grid of Precomputed Models*" ApJS, 2007, 169, pp. 328-352

[172] Robitaille T. P., Whitney B.A., Indebetouw R., Wood K., and Denzmore P., "*Interpreting Spectral Energy Distributions from Young Stellar Objects. I. A Grid of 200,000 YSO Model SEDs*" ApJS, 2006, 167, pp. 256-285

[173] Ruiz-Velasco A. E., Felli D., Migenes V., and Wiggins B. K., "VLBA Surveys of OH Masers in Star-forming Regions. I. Satellite Lines" ApJ, 2016, 822, pp. 8

[174] Sakai N., Honma M., Nakanishi H., et al., "*Outer Rotation Curve of the Galaxy with VERA I: Trigonometric Parallax of IRAS 05168+3634*" PASJ, 2012, 64, p. 1

[175] Salpeter E. E., "*The Luminosity Function and Stellar Evolution*" ApJ, 1955, 121, p. 161

[176] Sánchez-Portal M., Marston A., Altieri B., et al.. "*The pointing system of the Herschel space observatory. Description, Calibration, Performance and improvements*" Experimental Astronomy, 2014, 37, pp. 453-479

[177] Saraceno P., André Ph., Ceccarelli C., Griffin M., and Molinari S., "*An evolutionary diagram for young stellar objects*" A&A, 1996, 309, pp. 827-839

[178] Scalo J. M., "*The Stellar Initial Mass Function*" Fundamentals of Cosmic Physics, 1986, 11, pp. 1-278

[179] Schlegel D. J., Finkbeiner D. P., and Davis M., "*Maps of Dust Infrared Emission for Use in Estimation of Reddening and Cosmic Microwave Background Radiation Foregrounds*" ApJ, 1998, 500, pp. 525-553

[180] Shepherd D. S., Nürnberger D. E., and Bronfman L., "*Discovery of a Massive Protostar near IRAS 18507+0121*" ApJ, 2004, 602, pp. 850-859

[181] Shetty R., Kauffmann J., Schnee S., and Goodman A. A., "*The Effect of Noise on the Dust Temperature-Spectral Index Correlation*" ApJ, 2009a, 696, pp. 676-680

[182] Shu F.H., Adams F.C., and Lizano S., "*Star formation in molecular clouds: observation and theory*" ARA&A, 1987, 25, pp. 23-81

[183] Siess L., Dufour E., and Forestini M., "*An internet server for pre-main sequence tracks of low- and intermediate-mass stars*" A&A, 2000, 358, pp. 593-599

[184] Simon R., Jackson J. M., Clemens D. P., Bania T. M., and Heyer M. H., "*The Structure of Four Molecular Cloud Complexes in the BU-FCRAO Milky Way Galactic Ring Survey*" ApJ, 2001, 551, pp. 747-763

[185] Soderblom D. R., "*The Ages of Stars*" ARA&A, 2010, 48, pp. 581-629

[186] Solin O., Ukkonen E., and Haikala L., "*Mining the UKIDSS Galactic Plane Survey: star formation and embedded clusters*" A&A, 2012, 542, pp. 23

[187] Stahler S. W. and Palla F., "*The Formation of Stars*" 2004, pp. 865

[188] Stern D., Eisenhardt P., Gorjian V., et al., "*Mid-Infrared Selection of Active Galaxies*" ApJ, 2005, 631, pp. 163-168

[189] Strom S.E., "*The early evolution of stars*" Astronomical Society of the Pacific, 1995, 73 pp. 205-214

[190] Sunada K., Nakazato T., Ikeda N., et al., "*Water Maser and Ammonia Survey toward IRAS Sources in the Galaxy I. H_2O Maser Data*" PASJ, 2007, 59, pp. 1185-1219

[191] Szymczak M., Hrynek G., and Kus A. J., "*A survey of the 6.7 GHz methanol maser emission from IRAS sources. I. Data*" A&AS, 2000, 143, pp. 269-301

[192] Terebey S., Van Buren D., Hancock T., et al., "*Dynamical Structure in HST/NICMOS Images of Nearby Protostars*" Astronomical Society of the Pacific, 2001, 243, p. 243

[193] Testi L., Palla F., and Natta A., "*The onset of cluster formation around Herbig Ae/Be stars*" A&A, 1999, 342, pp. 515-523

[194] Testi L., Palla F., Prusti T., Natta A, Maitaglaiti S., "*A search for clustering around Herbig Ae/Be stars*" A&A, 1997, 320, pp.159-166

[195] Turner D. G. and Forbes D., "*Berkeley 87, a heavily-obscured young cluster associated with the ON2star-formation complex and containing the WO star Stephenson 3*" PASP, 1982, 94, pp. 789-801

[196] Varricatt W. P., Davis C. J., Ramsay S., and Todd S. P., "*A near-IR imaging survey of intermediate- and high-mass young stellar outflow candidates*" MNRAS, 2010, 404, pp. 661-720

[197] Vig S., Ghosh S. K., Kulkarni V. K., Ojha D. K., and Verma R. P., "*Infrared and Radio Study of Star-forming Regions Associated with IRAS 19111+1048 and IRAS 19110+1045*" ApJ, 2006, 637, pp. 400-414

[198] Wang K., Wu Y. F., Ran L., Yu W. T., and Miller M., "*The relation between ^{13}CO $J = 2$-1 line width in molecular clouds and bolometric luminosity of associated IRAS sources*" A&A, 2009, 507, pp. 369-376

[199] Wood D. O. S. and Churchwell E., "*The Morphologies and Physical Properties of Ultracompact H II Regions*" ApJS, 1989, 69, p. 831

[200] Wouterloot J. G. A., and Brand J., "*IRAS sources beyond the solar circle. I. CO observations*" A&AS, 1989, 80, pp. 149-187

[201] Wright E. L., Eisenhardt P. R. M., Mainzer A. K., et al., "*The Wide-field Infrared Survey Explorer (WISE): Mission Description and Initial On-orbit Performance*" AJ, 2010, 140, pp. 1868-1881

[202] Wu Y. W., Reid M. J., Sakai N., et al., "*Trigonometric Parallaxes of Star-forming Regions beyond the Tangent Point of the Sagittarius Spiral Arm*" ApJ, 2019, 874, pp. 13

[203] Zhang Q., Hunter T. R., Brand J., et al., "*Search for CO Outflows toward a Sample of 69 High-Mass Protostellar Candidates. II. Outflow Properties*" ApJ, 2005, 625, pp. 864-882

[204] Zinnecker H. and Yorke H. W., "*Toward Understanding Massive Star Formation*" ARA&A, 2007, 45, pp. 481-563

[205] Zinnecker H., McCaughrean M. J., and Wilking B. A, "*The Initial Stellar Population*" University of Arizona Press, 1993, p. 429